Characterization of Photonic Crystal Fibers and Metamaterials: Theory and Experiments

**A thesis submitted to the
Faculty of Technology, University of Delhi
for the award of the degree of**

DOCTOR OF PHILOSOPHY
IN
APPLIED PHYSICS

By

Kamal Kishor

Under the Supervision of :

PROF. R. K. SINHA

Department of Applied Physics,
Delhi College of Engineering,
(Now, Delhi Technological University)
Faculty of Technology
University of Delhi
Delhi-110 042, India

<u>CERTIFICATE</u>

This is to certify that the thesis entitled "**CHARACTERIZATION OF PHOTONIC CRYSTAL FIBERS AND METAMATERIALS: THEORY AND EXPERIMENTS**", being submitted by Mr. Kamal Kishor, for the award of degree of Doctor of Philosophy to the Faculty of Technology, University of Delhi, India, is a record of bonafide research work carried out by him under my supervision. He has fulfilled the requirements which have reached the requisite standard for the submission of this thesis. The work reported in this thesis has not been submitted to any other University or Institution for the award of any degree or diploma.

(Prof. R.K Sinha)

Supervisor

Department of Applied Physics,

Delhi College of Engineering

(Now Delhi Technological University)

Faculty of technology, University of Delhi

Bawana Road, Delhi-110042, India

CERTIFICATE

This is to certify that the thesis entitled "**CHARACTERIZATION OF PHOTONIC CRYSTAL FIBERS AND METAMATERIALS: THEORY AND EXPERIMENTS**", being submitted for the award of degree of Doctor of Philosophy to the Faculty of Technology, University of Delhi, India, is based on the research work carried out by me under the supervision of Prof. R. K. Sinha, Department of Applied Physics, Delhi College Of Engineering (Now Delhi Technological University), Faculty of Technology, University of Delhi. The results embodied in this thesis have not been submitted to any other University or Institution for the award of any degree or diploma.

Place: Delhi   **(Kamal Kishor)**

Date: **Candidate**

(Prof. R.K Sinha)

Supervisor

Department of Applied Physics

Delhi College of Engineering,

(Now Delhi Technological University)

Faculty of Technology, University of Delhi

Bawana Road, Delhi-110042, India

(Prof. Sudhish Pachauri)

Head, Applied Sciences and Humanities

& Dean, **Faculty of Technology,**

University Of Delhi

Delhi-110042, India

DEPARTMENT OF APPLIED SCIENCES AND HUMANITIES

FACULTY OF TECHNOLOGY

UNIVERSITY OF DELHI

DELHI-110042, INDIA

Date:

CERTIFICATE OF ORIGINALITY

The research work embodied in this thesis entitled **"Characterization of Photonic Crystal Fibers and Metamaterials: Theory and Experiments"** has been carried out by me at the Department of Applied Sciences and Humanities, Faculty of Technology, University of Delhi, India. The manuscript has been subjected to plagiarism check by CheckForPlagiarism.net software. I declare that the work and language included in this thesis are free from any kind of plagiarism.

Kamal Kishor

Acknowledgement

It is indeed a great pleasure to express my sincere appreciation and deepest gratitude to my supervisor Prof. R. K. Sinha for his unwavering guidance, motivation, support and encouragement throughout my PhD which made me proficient to face and win over the challenges. I am equally thankful him for his generosity in time, the valuable discussion in sharing this knowledge and experience throughout my research work.

I would like to thank TIFAC-CORE, Delhi Technological University for financial and infrastructure support. I would like to thank Photon Design, UK to provide me Omnisim FDTD simulation tool to carry out my research work.

Many people and organization have helped me in different ways and different places throughout my Ph.D. career. I would like to thank all faculties and staffs of DTU for their love and support. I would like to thank Basudev Lahiri, James Watt Nano Fabrication Centre, and University of Glasgow for providing me the experimental support. I will always carry fond memories of my colleagues and friends for their valuable friendship, support and our profound discussions.

I would like to thank Dr. Anshu D. Varshney (JIIT Noida), Dr. Ajeet Kumar (DTU), Dr. Yogita Kalra (DTU), Dr. Shailendra K Varshney (IIT Kharagpur) for all the fruitful exchanges and technical discussions on research issues.

I express my deepest regard and gratitude to my parents, wife and family members, who forebear pain and discomfort in bringing me up to this stage. I would appreciate their unconditional love, support and encouragement throughout my studies. Finally, I must thank my little daughter for giving her endless love and innocent cute smile which wash out all stress and give me a new strength to carry out this research work towards a completion.

Kamal Kishor   Place:

(Candidate)   Date:

Characterization of Photonic Crystal Fiber and Metamaterial: Theory and Experiment

Abstract submitted to the
Faculty of Technology, University of Delhi
for the award of the degree of

DOCTOR OF PHILOSOPHY
IN
APPLIED PHYSICS

By

Kamal Kishor

Under the Supervision of :

PROF. R. K. SINHA

Department of Applied Physics,
Delhi College of Engineering,
(Now, Delhi Technological University)
Faculty of Technology
University of Delhi
Delhi-110 042, India

Characterization of Photonic Crystal Fiber and Metamaterial: Theory and Experiment

Recent developments in optical technologies are being shifted towards nano-scale devices of sub-wavelength dimensions. In these emerging technologies photons are being manipulated and controlled using devices having unit cells with a dimension in wavelength range or even with a dimension smaller than wavelength. Photonic crystal and Metamaterials are the prime focus area of research in photonics in the past few years with the number of publications and patents increasing exponentially. Photonic crystals are patterned materials with a well defined periodicity in dielectric constant. Photonic Crystal Fibers (PCFs) are one of the most important applications of photonic crystal materials. PCF is an optical fibers made up of single material with an arrangement of periodic air holes across the cross-section running down its entire length. PCF has the ability to confine light with the confinement characteristics, not possible in conventional optical fiber due to its high degree of design flexibility.

Metamaterials are the specially designed structures having negative permittivity and permeability simultaneously at the same operating frequency for which the electromagnetic wave shows anomalous behaviour, i.e. phase and group velocity would be in opposite direction. Metamaterials provide precise control over the flow of electromagnetic waves.
 It is now the critical phase of their development as they move fast from the realm of fundamental studies to the manufacturing of photonic devices and commercial deployment in optical communication network. For the extraction of optimum performance of any designed structure it is the important to characterize it in terms of its waveguiding, geometrical and transmission parameters.

In this thesis first the characterization of Endlessly Single Mode (ESM) PCF from its Far Field intensity measurements has been explored. The characterization results are verified and supported with experimental as well as simulation results. From the experimental measurements of the far field intensity pattern, we obtained the transmission characteristics

of ESM PCF in terms of V-number, effective refractive index of the cladding, radius of the core, numerical aperture, etc. The experimental values of the waveguiding and geometrical parameters are found to be in agreement with the simulation results obtained using Improved Effective Index Method (IEIM) and Scanning Electron Microscope (SEM) data. Further, characterization of a specially designed Polarization Maintaining (PM) PCF has explored using Far Field intensity distribution pattern. It is observed that the waveguiding and geometrical parameters obtained from the far field measurement of PM PCF match with the manufacturer/simulation/SEM data within the experimental limits. Thus, this characterization method provides a useful tool for online characterization of PM PCF.

Next, a V-shaped SRR metamaterial has been fabricated and characterized. The fabricated structure has shown a unique property of angular-gap-dependent tuneable negative refractive index (NRI) characteristics. The unique property of this structure is that by varying the angular gap between its arms, the capacitance (C) for the structure can be changed, and hence there can be a great control over the NRI. It is experimentally and computationally investigated the interdependence of the capacitance (C) and inductance (L) of the structure, and it is observed that by changing the angular gap of V-shaped SRRs, it is possible to control/tune their NRI at the corresponding resonance wavelength.

After the tunable metamaterial structure next is to design of a split ring resonance (SRR) based planar metamaterial to achieve the negative refraction in optical communication window. A "I" shaped split ring resonator (SRR) metamaterial designed has been explored. This metamaterial design is showing negative refraction in the optical communication window around wavelength of 1.5 μm. Further the structure is characterized using finite differential time domain (FDTD) method in terms of its propagation characteristics. All the key electromagnetic parameters i.e. such as permittivity (ε), permeability (μ), refractive index (n) etc have been obtained from the simulation data obtained for propagation characteristics for the structure. The electromagnetic parameters (such as permittivity (ε) and permeability (μ)) as well as the refractive index for the reported structure are negative in broad optical communication window of 1.4μm to 1.6μm.

CONTENTS

Reprints of research papers

List of Tables

List of Figures

List of abbreviations

PCF   Photonic Crystal Fiber

PM PCF   Polarization maintaining Photonic Crystal Fiber

ESM PCF   Endlessly Single Mode Photonic Crystal Fiber

LMA   Large Mode Area

SEM   Scanning Electron Microscope

PMF   Polarization Maintaining Fibers

PMD   Polarization Mode Dispersion

SAP   Stress Applying Parts

EBL   Electron Beam Lithography

FTIR   Fourier transform Infra-Red

SRR   Split Ring Resonator

TE   Transverse Electric

TM   Transverse Magnetic

NA   Numerical Aperture

MFD   Mode Field Area

IEIM   Improved Effective Index Method

FEM   Finite Element Method

FDTD   Finite Difference Time Domain

NRI   Negative Refractive Index

RCW   Rectangular Core Waveguide

Chapter 1

CHAPTER 1

Introduction

1.1 Introduction

Today, due to rapidly changing nano-fabrication limit and sub-wavelength imaging technology, everyday various new design and structure is developed in the world of photonic devices. For the assessment of optimum performance for any newly designed structure and device it is the important to characterize it in terms of its waveguiding, geometrical and transmission parameters with accuracy. In view of increasing demand of characterization of new photonics devices, the present thesis mainly focused on "characterization of Photonic Crystal Fibers and Metamaterials: Theory and Experiments".

Optical fibers have evolved into many forms since the introduction of conventional step index fibers in the 1970s [1-2]. Optical fibers have a very wide range of applications, e.g. waveguide, medical endoscopy, optical communication, fiber amplifier (generate and amplify laser light), temperature and stress sensor [3-5]. The wide application of optical fiber leads to design of application specific fiber. In the recent past many new types of application specific optical fiber [6-9] is designed which also created a demand to develop the characterization techniques for these newly designed fibers.

1.2 Photonic Crystal Fibers (PCF)

Photonic Crystal Fibers (PCF) is a new variant of the micro structured optical fibers. PCFs are single material optical fiber with a cladding having microstructure air hole running down its entire length [10-20]. All remarkable properties of PCFs come from the wavelength dependence of cladding refractive index [21]. PCFs have versatile applications in optical communications ranging from nonlinear optical signal processing to high power fiber amplifiers [22-30].

1.2.1 Endlessly Single Mode (ESM) PCF

The most important properties of PCFs for telecommunication is that it can be, under certain circumstances become endlessly single mode operation over a wide range of wavelength. V-parameter must be less than 2.405 for the optical fiber to be single mode [13, 15-17]. Thus single-mode fibers for one operating wavelength are in fact act as multi-mode for the signal of other sufficiently short wavelength. The wide single-mode operating range of the photonic crystal fiber is explained by considering the effective refractive index of the cladding. The field in case of shorter wavelengths is more concentrated in the silica (core) regions and less penetrates to the holey (cladding) region. This results in raising the effective cladding index. On the other hand, the field in case of higher wavelengths have more penetration to the holey (cladding) region. This results in lowering the effective cladding index of the same PCFs. In this way, different operating wavelengths experience different effective index for the same PCF. So the change in refractive index contrast for the same fiber with the change in operating wavelength helps to keep V-parameter almost constant for a PCF over a wide range of wavelengths. Figure 1.1 showing the Scanning Electron Microscope (SEM) images of the cross section of a ESM-PCF.
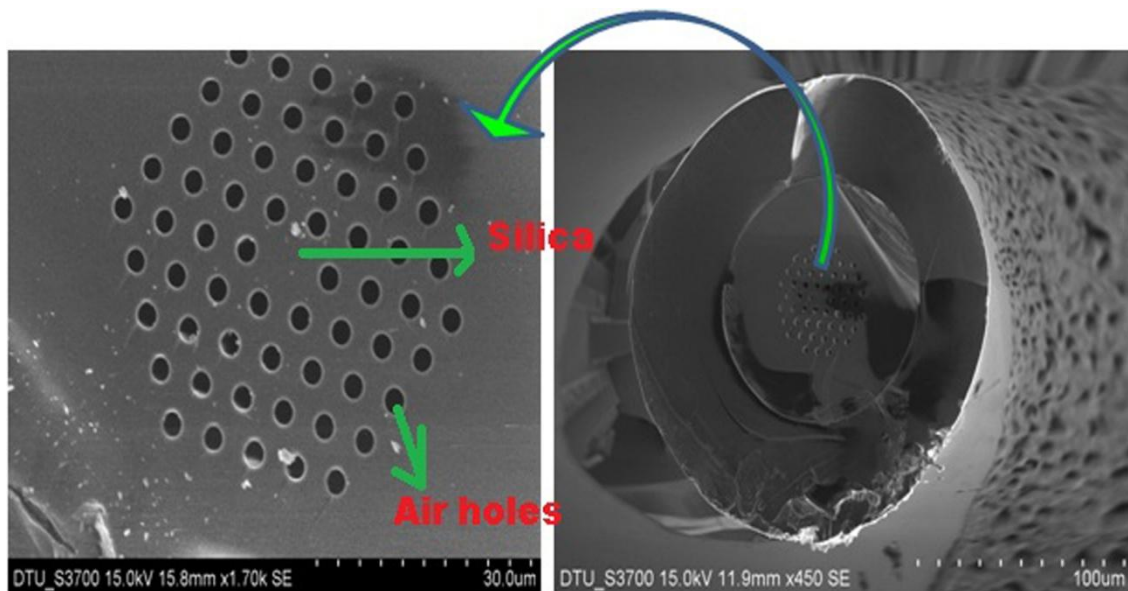
Figure 1.1: Scanning Electron Microscope images of the cross section of a PCF

1.2.2 Polarization maintaining PCF

In high bit rate optical fiber communication systems Polarization Maintaining Fibers (PMFs) are required to eliminate the polarization mode dispersion (PMD). It is important to create birefringence within a PMF to transmit the stable state of polarization. The circular symmetry in an optical fiber is broken using birefringence breaks, either by forming a non-circular fiber core (shape induced birefringence), or by inducing constant stresses within the fiber (stress induced birefringence) with stress applying parts (SAP) [10, 15, 31]. PMF has two principal transmission axes within the core of the fiber, called as the fast and slow axes of the fiber as per the effective refractive index experienced by the propagating modes. PMFs have been extensively applied in coherent optical communication systems and in polarization sensitive experiments.

The development of photonic crystal fiber, given a way to design highly birefringent fiber as birefringence can be easily tailored and enhanced in polarization maintaining (PM) PCF. Using two different air hole diameters along two orthogonal axes near the core region of the PCF, an extraordinary PM PCF has been fabricated. The transmission characteristics of this PM PCF exhibit very high birefringence in the order of 10^{-3}; due to high cladding effective index contrast between two orthogonal polarization modes [32-34]. Figure 1.2 showing the Scanning Electron Microscope (SEM) images of the cross section of this special PM-PCF
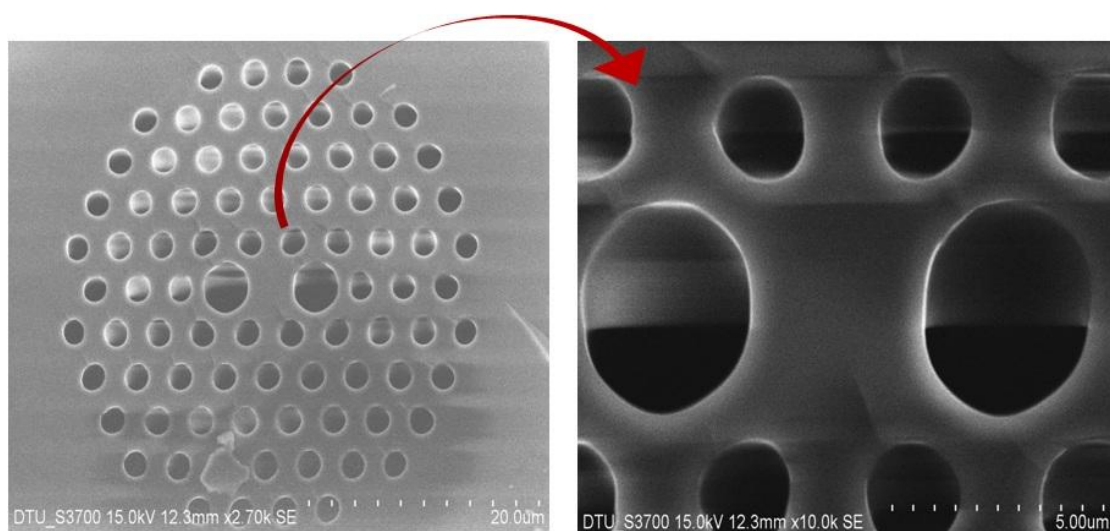
Figure 1.2: Scanning Electron Microscope images of the cross section of PM-PCF

1.3 Metamaterials

The name Metamaterials is coined from Greek meaning "materials beyond the conventional materials found in nature". The refractive index n of any material is determined by equation $n = \pm\sqrt{(\varepsilon_r \mu_r)}$. All naturally found optical materials have positive electric permittivity ε and magnetic permeability μ and by convention the positive value of n is taken in account. In nature, there are some materials e.g. silver and gold have negative electric permittivity at shorter wavelengths but positive magnetic permeability at that wavelength, and making them often opaque to the electromagnetic radiation for that wavelength. In case of artificially designed metamaterial, both electric permittivity and magnetic permeability is negative, which results n real and under this situation negative square root for n is taken into account (negative refractive index) [35-37]. Figure 1.3 shows the classification of materials and their electromagnetic parameters.

Due to the amazing electromagnetic properties of negative refractive index Metamaterials emerged as an important technological and scientific advancement for every aspect of life e.g. lens, antenna, telecommunication, radars, imaging and many more [38-51]. The Electromagnetic wave shows anomalous behaviour (flow of energy in a direction opposite to that of wave propagation) i.e. phase and group velocity are in opposite direction [35].

After the rapidly-developing Nano-fabrication and sub-wavelength techniques, different types of metamaterial structures (such as square, Ω- shaped, circular, U-shaped, S-shaped, asymmetric-rings and asymmetric-rings) is designed for different applications purpose [52-58].
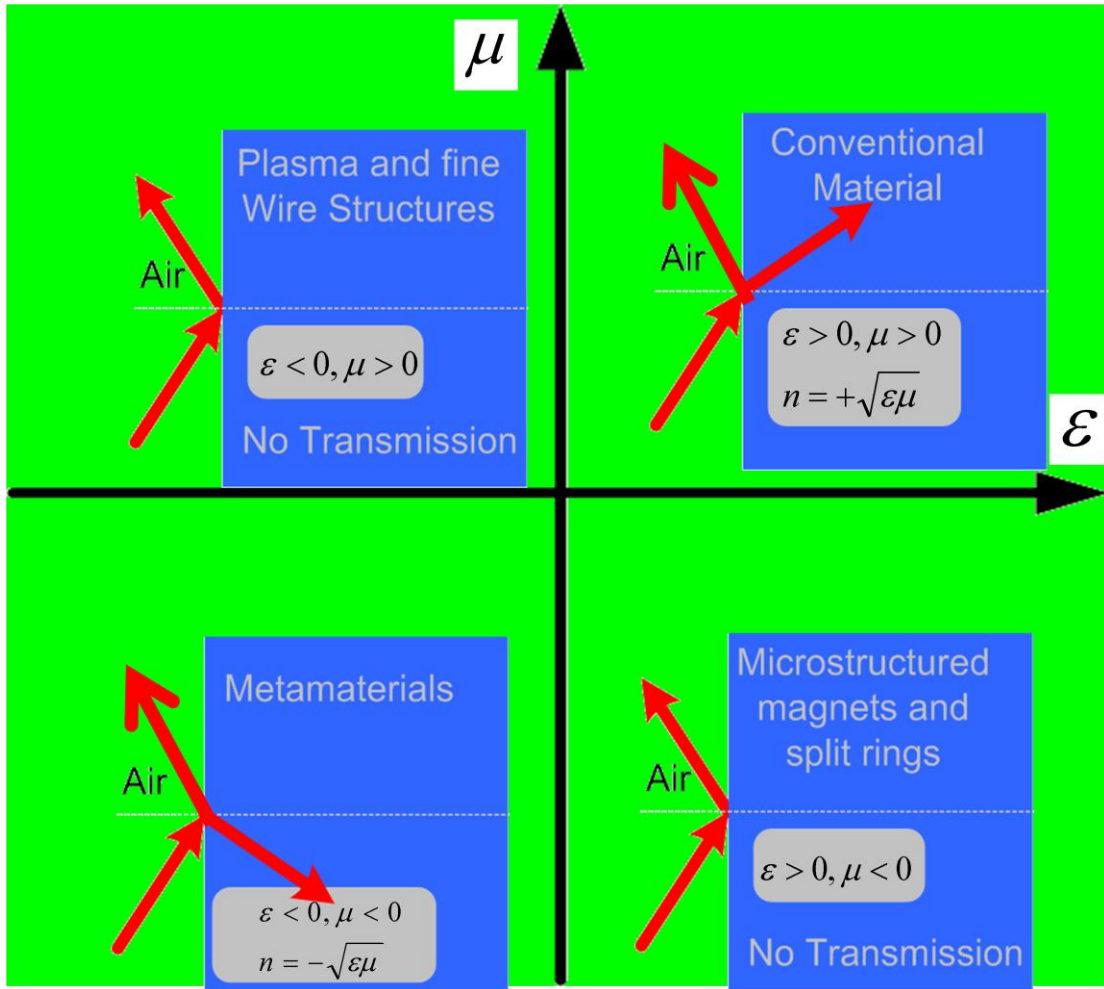
Figure 1.3: Classification of materials

1.4 Instruments and Experimental set-up used

1.4.1 Experimental set-up for the characterization of PCFs

The experimental setup for the characterization of PCFs consists of a He-Ne laser with wavelength 633 nm, microscopic lens, fiber chuck and holders, Polarizer sheet (to find the polarization axes of laser), Silicon photo-detector (818-SL/Newport) with digital display and 10 m long PCF samples. Both the ends of the sample PCF are properly stripped and cleaved to minimize the reflection losses. Fiber output end is mounted on a calibrated circular mount fitted with a photo detector such that the fiber end is at the centre of the circle and when we rotate the circular mount photo detector records the far field at the circumference of the circle. Figure 1.4 shows the schematic

diagram of experimental setup to record the far field intensity pattern of PCF for its characterization.
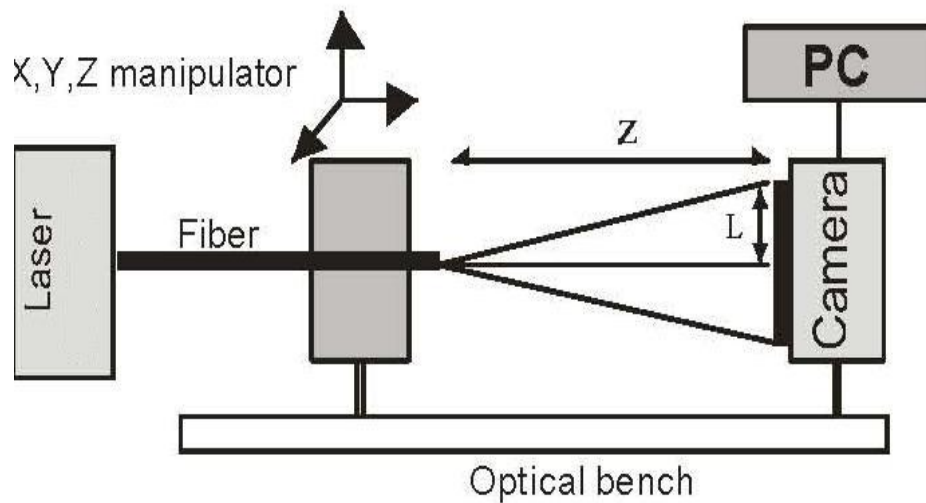
Figure 1.4: Schematic diagram of experimental setup for the characterization of PCFs

For the measurement of the physical parameters like core diameter, hole radius and pitch etc. of the PCFs, Hitachi S-3700N Scanning Electron Microscope (SEM) is used, shown in figure 1.5

Figure 1.5: Hitachi S-3700N Scanning Electron Microscope (SEM)

1.4.2 Experimental set-up for the characterization of Metamaterials

The fabrication of metamaterial done in this thesis work has are three steps. The fabrication starts from a flat cleaved and chemically cleaned wafer. After that to form a unique film on the substrate a resist is spun on the n-doped silicon substrate.

In next step, using Electron Beam Lithography (EBL) the patterning process had been done to define the desired structures on the resist. EBL has been chosen as the common photo lithography has many limitations to provide the desired resolution in such a required nanoscale level fabrication and EBL also does not require any additional masks. Figure 1.6 shows Vistec VB6 UHR EWF electron beam lithography facility present at James Watt Nanofabrication Centre, University of Glasgow, used in the thesis work.

Figure 1.6: Vistec VB6 UHR EWF Electron Beam Lithography

Two main limitations for EBL system, namely scattering and proximity effect is avoided to the best extent possible. Scattering effect which leads to a much larger exposure area than defined exposure area is controlled by applying a higher acceleration voltage.

The proximity effect results in reducing its contrast i.e. each unit of metamaterial are not completely isolated as electrons of the exposure of an adjacent region spill over

into the next exposure feature. Proximity effect is controlled by calculating the exposure function on the resist.

In the third step, to transfer the patterns from the resist to the substrate the metal lift off techniques is used. A thin layer of titanium is used due to its good sticking property as gold layer does not stick properly on silicon substrate.

After the fabrication process of different samples, their reflectance measurements were done using a Nicolet continuum Fourier transform infrared (FTIR) spectroscope fitted with a case grain objective of 10× magnifications and an NA of 0.25. The measurements were taken for both orthogonal linear polarizations of the incident light (TE and TM polarization) and were then normalized with respect to the reflectivity of a bare silicon substrate. All measurements were taken at normal incidence. Figure 1.7 shows Nicolet continuum Fourier Transform Infrared (FTIR) spectroscope, used in the thesis work.

Figure 1.7: Nicolet continuum Fourier Transform Infrared (FTIR) spectroscope

1.5   Analytical and Numerical Methods

In this thesis work mainly following analytical and numerical methods are used to characterize the PCFs and Metamaterials.

1.5.1   <u>Far-Field method</u>

Far-Field measurement is also referred as the Fraunhofer region intensity measurement. It is the region where the angular field distribution is essentially independent of distance from the source. The far-field radiation pattern $\Psi(r, \theta, \Phi)$ is the inverse Fourier transform of the aperture or near fields. For a single mode fiber the fundamental mode field can be accurately expressed by Gaussian function. The Gaussian far-field intensity distribution of fibers has cylindrical symmetry and depends only on the angle θ. The normalized (w.r.t. $\theta=0$) far-field intensity distribution I (θ) [5, 59, 60] for the fundamental mode of fiber with normalized radiation angle (α) is given as

$$I(\theta) = |\psi|^2$$

$$|\psi|^2 = \left[\frac{U^2 W^2}{\left(U^2 - \alpha^2\right)\left(W^2 + \alpha^2\right)}\left\{J_0(\alpha) - \alpha J_1(\alpha)\frac{J_0(U)}{U J_1(U)}\right\}\right]^2 \qquad \text{for} \quad U \neq \alpha$$

$$|\psi|^2 = \left[\frac{U^2 W^2}{\left(2V^2\right)\left(U J_1(U)\right)}\left\{J_0^2(\alpha) + J_1^2(\alpha)\right\}\right]^2 \qquad \text{for} \quad U = \alpha$$

Where, $V^2 = U^2 + W^2$; $\alpha = ka\sin\theta$; $k = \frac{2\pi}{\lambda_o}$; λ_o is the free-space wavelength and 'a' is the radius of the core. Figure 1.7 shows the far field intensity distribution pattern for a fiber with respect to α.
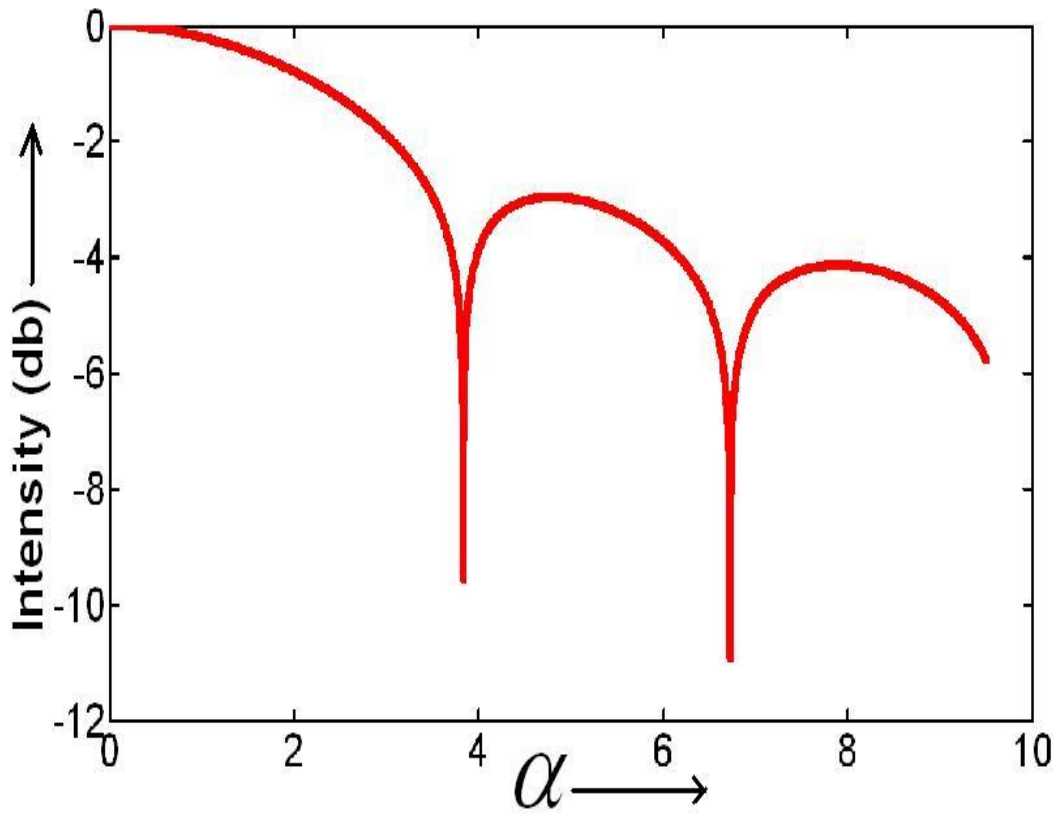
Figure 1.8: Far- Field intensity pattern

It is noted that it is practically very difficult to measure the first minimum intensity position accurately in far field intensity pattern. So, θ_{10} (angles at which the intensity drops to 10% of its maximum value) is taken as first minimum position [5, 59].

1.5.2 Improved Effective index Method

The Improved Effective index Method (IEIM) was developed by Park and Lee [61]. In IEIM the core radius (r_c) is not fixed but depend on pitch (Λ) and air hole diameter (d) of the PCF [62-64]. IEIM improves the result accuracy of the earlier used effective index method. In IEIM the core radius is optimized using empirical formula given as follows

$$\frac{r_c}{\Lambda} = c_1 / \{1 + \exp[(\frac{d}{\Lambda} - c_3)/c_2]\}$$

Where $c_1 = 0.686064$; $c_2 = 0.265366$ and $c_3 = 1.291080$;

The tolerance of this formula is 1e-6.

12

1.5.3 Finite element method

Finite Element Method (FEM) is a better choice for the analysis of a structure which has complicated boundary like PCFs where the boundary lacks smoothness and the desired precision varies over the entire domain [65-66]. The FEM is a numerical technique for calculating approximate solutions of boundary value problems for partial differential equations. FEM divides the whole problem domain into subdivision of different shape and sizes as per requirement e.g. triangles and quadrilaterals [67-68]. This different-sized elements approach makes FEM best mathematical tool for PCFs and to calculate expected mode field response. Also in FEM, variational method is used to solve the problem which helps in minimizing an associated error function.

1.5.4 Finite-Difference Time-Domain

Finite Difference Time Domain (FDTD) is a versatile time-domain based numerical technique used for computing electrodynamics problems which require solutions over a wide frequency range with a single simulation [69-71]. In FDTD technique far-field radiation over a wide range of frequencies can be computed in a single simulation when a broadband pulse is used as the source. This is main reason to use FDTD tool is used in this thesis to determine the resonant frequencies for the fabricated structure. The FDTD method is a grid-based differential method and it discretize the time-dependent Maxwell's equations using central-difference approximations for the space and time partial derivatives [72-73]. In Maxwell's equations the time derivative of E-field depends on the change in the H-field across space. So in FDTD method the E and H fields are calculated everywhere in the computational domain with the time [74-75]. So, the results are updated by Iterating the either E-field or H-field with time. It helps to understand that how the E and H field are interacting with the structure over time.

The radiated far-field is calculated using near to far-field transformation as the FDTD method calculate electromagnetic fields within a compact spatial region.

13

1.6 Overview of the thesis

In this thesis work, the characterization of different types of Photonic Crystal Fibers and specially designed polarization maintain PCF has been done theoretically as well as experimentally. The geometrical and wave guiding parameters of the PCFs has been calculated using far field intensity. Further, in this thesis the Design, fabrication and characterization of metamaterial in terms of electromagnetic parameters (electric permittivity 'ε', magnetic permeability 'μ', refractive index 'n' etc.) has been done. Structure for exhibiting tunable negative refractive index has been fabricated, analyzed and characterized. This thesis also includes the Design and characterization of SRR Structure for Negative refraction in optical communication window around 1.55 μm.

The thesis is organized as follows:

Chapter 1 includes the importance of Photonic Crystal Fiber and Metamaterials and the urgent need to develop the technique for the Characterization of Photonic Crystal Fiber and Metamaterial. Detailed literature review on the advances in area of Photonic Crystal Fiber and Metamaterial. This chapter also includes the analytical techniques, numerical methods and the experimental instruments/set-up used for the Characterization of Photonic Crystal Fibers and Metamaterials.

Chapter 2 includes the characterization of different types of Endlessly Single Mode Photonic Crystal Fibers (ESM PCFs) in terms of all the key parameters i.e. V-Number, effective refractive index of the cladding, radius of the core and numerical aperture using experimentally measured far-field intensity pattern. It has been shown that the transmission characteristics of ESM-PCFs obtained experimentally match with the simulation result calculated and also with the core diameter of PCF obtained from scanning electron microscope (SEM) within the experimental limit.

Chapter 3 includes the characterization of specially designed polarization maintaining photonic crystal fiber (PM PCF) in terms of all the key parameters i.e. mode field diameters (MFD), V-values along major and minor axes, mode field area, birefringence, core radius, effective refractive index of cladding and numerical apertures along major and minor axes of PM PCFs using experimentally measured far-field intensity pattern. It is shown that the experimentally obtained geometrical and wave guiding parameters of the PM PCF match with the manufacturer/simulation/scanning electron microscope (SEM) data within the experimental limits.

Chapter 4 describes design, fabrication and characterization of a V-shaped split ring resonator (SRR) metamaterial and has shown that it is possible to tune a negative refractive index by changing the angular gap of V-shaped SRR. The unique property of this structure is that by varying the angular gap between its arms, one can change the capacitance (C) for the structure, and hence can tune and control the Negative Refractive Index (NRI). The experimental and computational investigation of the interdependence of the capacitance (C) and inductance (L) of the structure has been done, and it is observed that by changing the angular gap of V-shaped SRRs, it is possible to control/tune their NRI at the corresponding resonance wavelength. Exploiting this important result for the extraordinary electromagnetic properties of the reported structure, the reported structure will put a significant mark in the design and development of Metamaterials based optical switch, tuneable devices, and sensors etc.

Chapter 5 focuses, a design of a split ring resonance (SRR) based planar metamaterial to achieve the negative refraction in optical communication window. The propagation characteristics in terms of reflection and transmission spectrum of the reported structure are obtained using finite differential time domain (FDTD) method. All the key electromagnetic parameters i.e. such as permittivity (ε), permeability (μ), refractive index (n) etc have been obtained from the simulation using propagation characteristics for the reported structure. It is observed and reported that the electromagnetic parameters (such as permittivity (ε) and permeability (μ)) as well as the refractive index for the reported structure is negative in broad optical

communication windows of 1.4μm to 1.6μm. The reported structure provides a way to build the device such as sensors, cloaking device etc. in the range of optical frequency using the property of negative refraction within very small characteristic size. This achievement opens the way to advance metamaterial technology in optical frequency range for the design of nano-scale optical devices.

Chapter 6 includes chapter wise brief summary of the research work carried out in the thesis and future scope of the research work carried out in the thesis.

Chapter 2

CHAPTER 2

Characterization of Endlessly Single Mode Photonic Crystal Fibers[1]

2.1 INTRODUCTION

In chapter one, urgent need of characterization of photonic devices is detailed. In the present chapter, characterization of Endlessly Single Mode (ESM) Photonic Crystal Fibers (PCFs) is demonstrated. First theory for the characterization of ESM-PCF from far field intensity measurements is developed. After that experimental measurement of the far field intensity pattern is taken. The transmission characteristics of ESM PCF in terms of *V*-number, effective refractive index of the cladding, radius of the core, numerical aperture etc is measured from the far field intensity pattern. The experimental values of the waveguiding and geometrical parameters are found to be in agreement with the simulation results obtained using Improved Effective index Method (IEIM) and Scanning Electron Microscope (SEM) data. This characterization technique developed in this chapter is well supported with experimental as well as simulation results.

2.2 Characterization of ESM PCFs from Far-Field: Theory

The geometrical and wave guiding parameters of ESM PCFs is obtained from the far field intensity pattern measurements. Far-Field is the region where the angular field distribution is essentially independent of distance from the source.

For ESM-PCFs the fundamental mode field can be accurately expressed by Gaussian function. The far-field intensity distribution of ESM-PCFs has symmetry and depends only on the angle θ. The normalized (w.r.t. θ=0) far-field intensity distribution I (θ) [5, 60, 76] for the fundamental mode of ESM-PCFs with normalized radiation angle (α) is given as follow

---

[1] Part of the results reported in this chapter has been published in the paper- "Experimental Verification of Improved Effective Index Method for Endlessly Single Mode Photonic Crystal Fiber", Optics and Laser in Engineering (Elsevier, Science Direct), vol. 50, pp. 182-186, 2012.

$$I(\theta) = |\psi|^2 = \left[\frac{U^2W^2}{\left(U^2 - \alpha^2\right)\left(W^2 + \alpha^2\right)}\left\{J_0(\alpha) - \alpha J_1(\alpha)\frac{J_0(U)}{UJ_1(U)}\right\}\right]^2 \qquad \text{for} \qquad U \neq \alpha$$

$$I(\theta) = |\psi|^2 = \left[\frac{U^2W^2}{\left(2V^2\right)\left(UJ_1(U)\right)}\left\{J_0^2(\alpha) + J_1^2(\alpha)\right\}\right]^2 \qquad \text{for} \qquad U = \alpha$$

Where, $V^2 = U^2 + W^2$; $\alpha = ka\sin\theta$; $k = \frac{2\pi}{\lambda_o}$; λ_o is the free-space operating wavelength and 'a' is the optimized core radius of ESM-PCFs. With the help of above equations a universal curve (figure 2.1) for ESM-PCF is plotted, which is used for the characterization of fiber from the far-field pattern measurement. Figure 2.1 shows the variation in the ratio α_{10}/α_{50} and α_{50} with V parameter for ESM-PCFs.
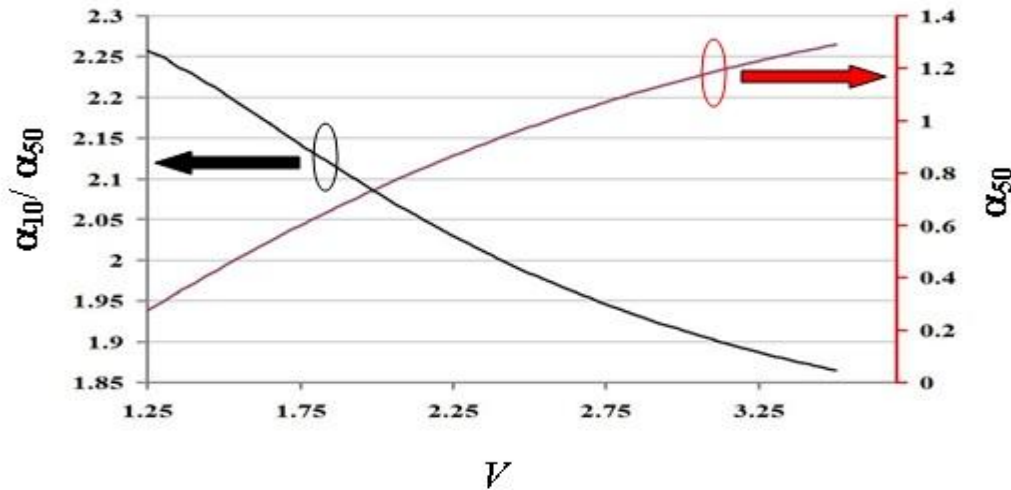
Figure 2.1: Variation of the ratio α_{10}/α_{50} (black) and α_{50} (red) with *V* parameter

It is noted that α_{10} and α_{50} are the values of $\alpha = ka\sin\theta$ at corresponding angles at which the intensity dropped to 10% and 50% of its maximum value (at $\theta=0$) in the far field intensity pattern. The first minimum intensity position is measured at θ_{10} because it is practically very difficult to measure the first minimum intensity position accurately in far field intensity pattern [5, 59].

2.3 Characterization of ESM-PCFs from far-field: Experiment

The experimental setup for the characterization of ESM-PCFs require a He-Ne laser with wavelength 633nm, Polarizer sheet (to find the polarization axes of laser),

sample fibers, fiber chuck and holders, microscopic lens, Silicon photo-detector (818-SL/Newport) with digital display. In this thesis work three samples of ESM-PCFs (ESM-12-01, LMA-10, and LMA-15) obtained from Crystal Fiber, Denmark is used for experiment. Figure 2.2 shows the SEM images of the ESM-PCFs taken for characterization verification.
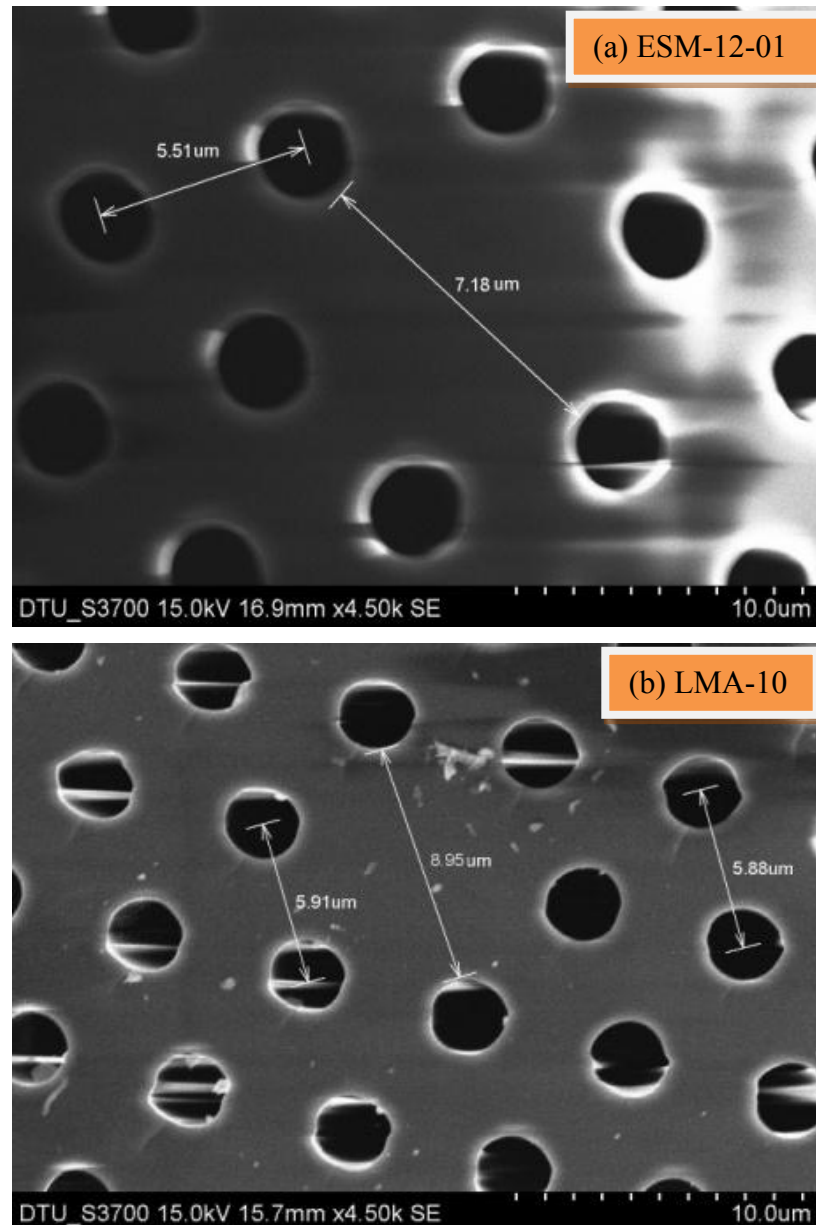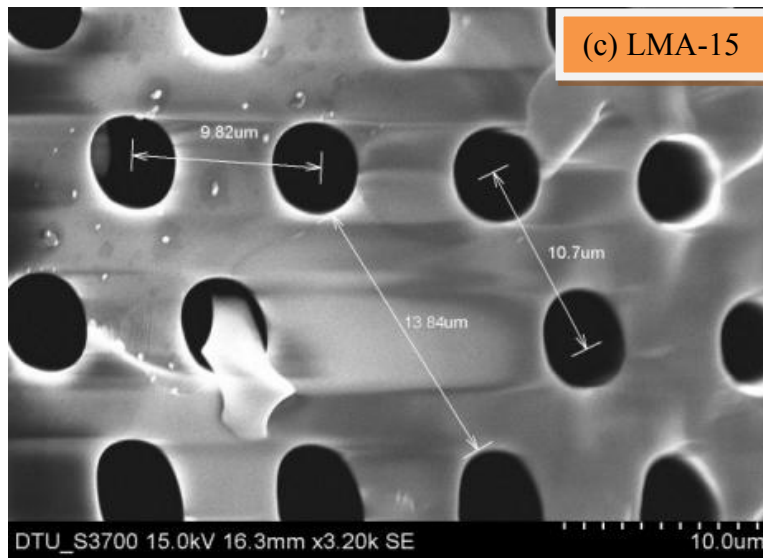
Figure 2.2: Scanning Electron Microscope images of the cross section of PCFs used;

(a) ESM-12-01; (b) LMA-10; (c) LMA-15

To minimize the reflection losses at ends of ESM PCFs, ends are properly and carefully stripped and cleaved. Silicon photo-detector (818-SL/Newport) is mounted on a calibrated circular mount at the circumference of the circular mount. Fiber output end is also fitted on the calibrated circular mount such that the fiber end is at the center of the circle. The least count of the calibrated circular mount was 0.1 degree (6'). So, when circular mount is rotated angularly, photo-detector records the far field intensity pattern. The sketch diagram for experimental set to record the far field intensity pattern of ESM PCFs is shown below in figure 2.3 while figure 2.4 shows the real time experimental set up.
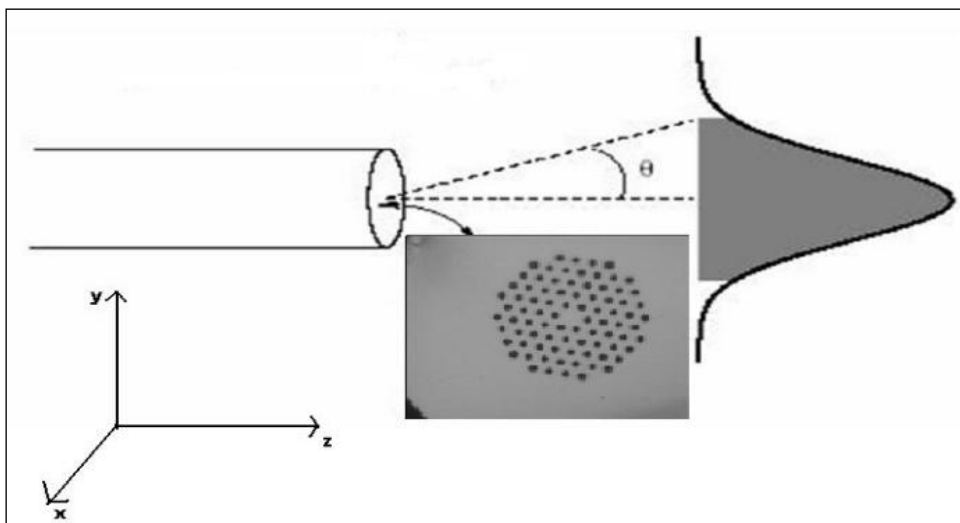
Figure 2.3: Sketch of Experimental arrangement for far field measurement
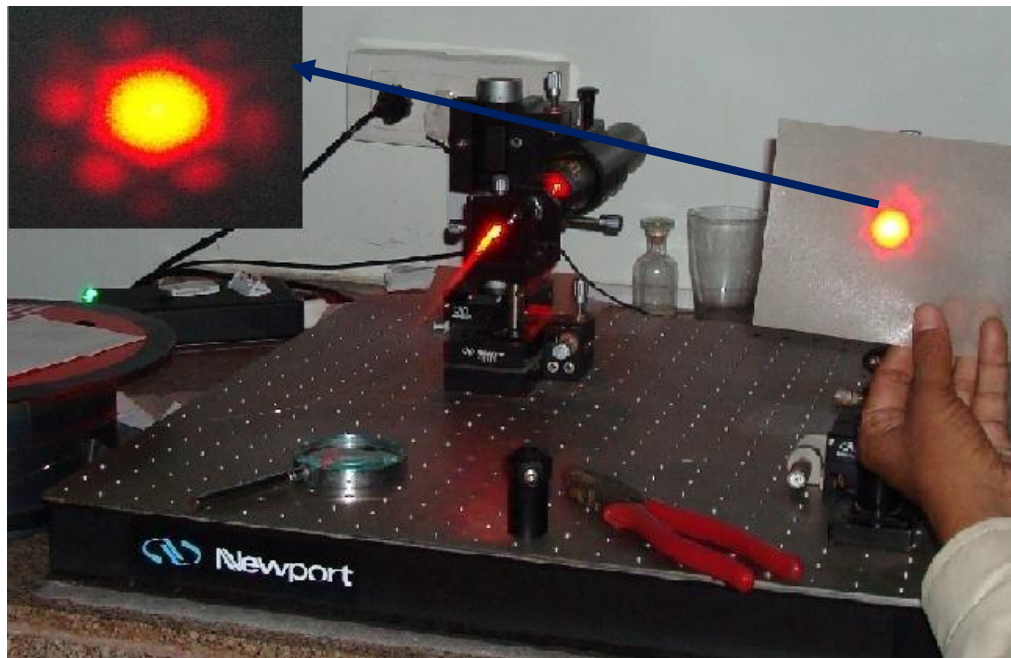
Figure 2.4: Real Time experimental arrangement; Far-Field pattern (inset)

The far-field radiation patterns of fundamental mode for all the PCFs are recorded at output end of the fibers. Figure 2.5 shows the curve of measured far field radiation pattern of the three PCFs used.
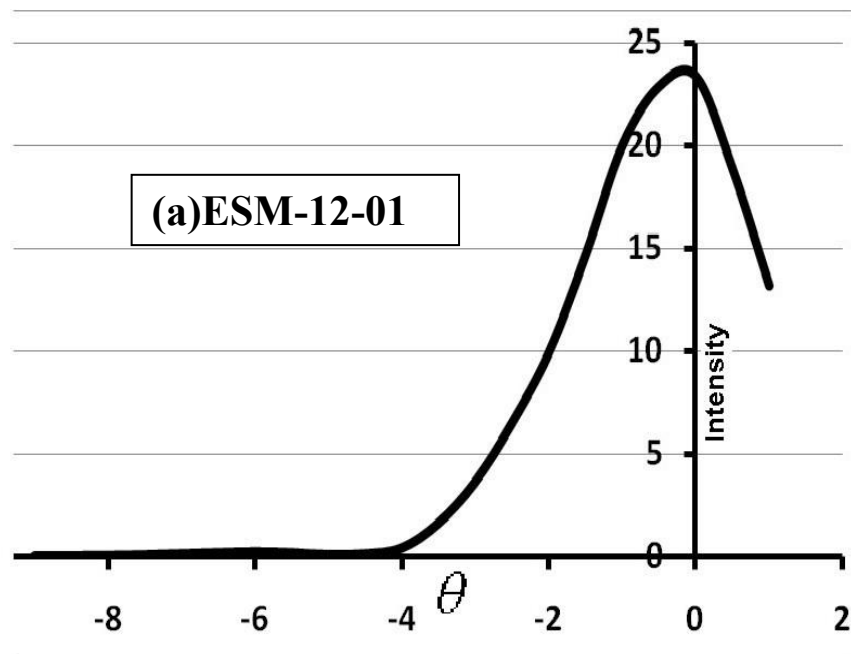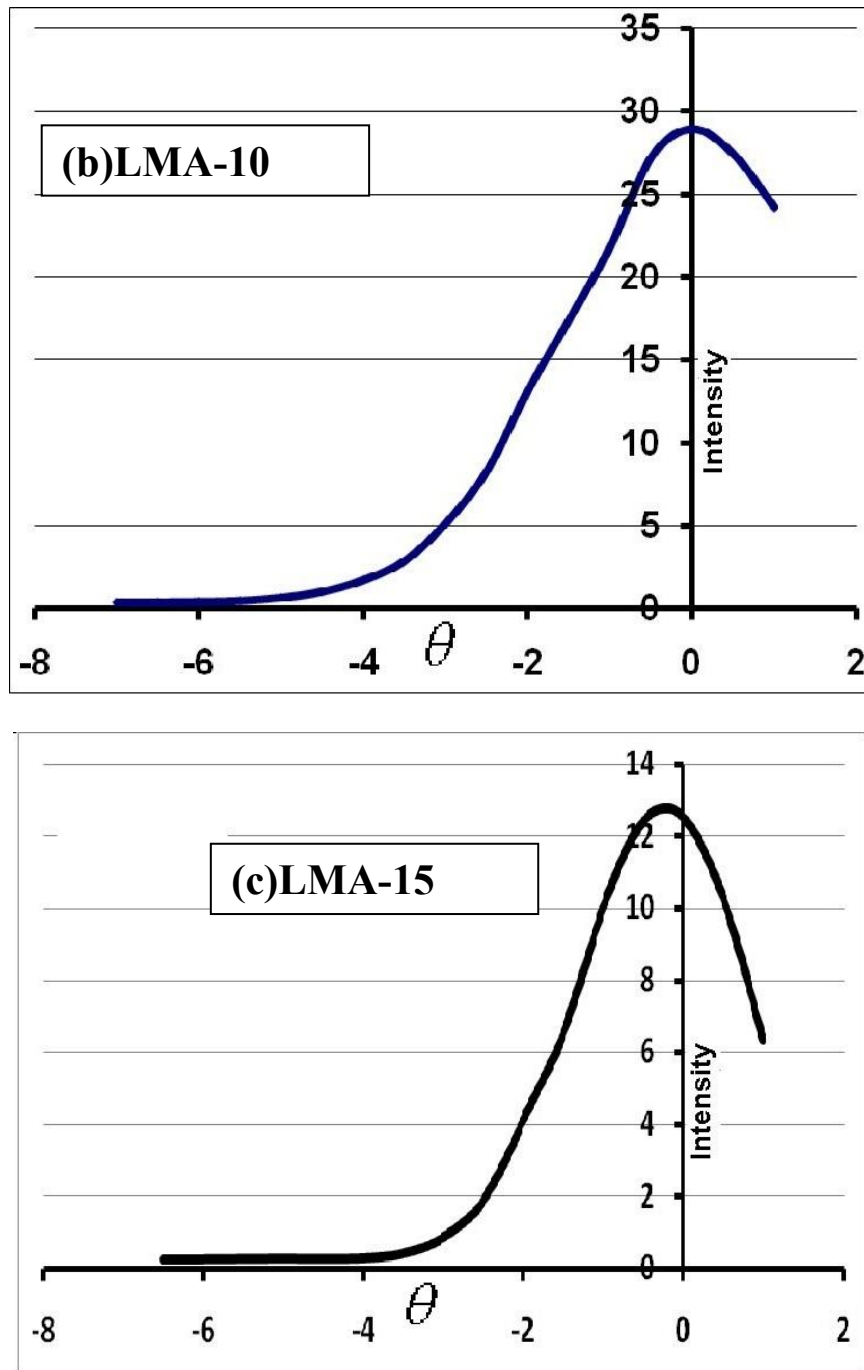
Figure 2.5: Measured far field intensity distribution of PCFs;
(a) ESM-12-01; (b) LMA-10; (c) LMA-15

From the measured far field intensity pattern shown in above figure, the corresponding angles θ_{10} and θ_{50} at which the intensity drops to 10% and 50% of its maximum value (at $\theta=0^{\circ}$) is obtained for the corresponding three ESM-PCFs. Thereby ratio $sin\theta_{10}/sin\theta_{50}$ is calculated. Using the universal graph (Figure 2.1), the V value

24

is obtained corresponding to experimental values of $sin\theta_{10}/sin\theta_{50}$ for each fiber. For the respective V parameter the corresponding $\alpha_{50}(= k_o a sin\theta_{50})$ is calculated from the right hand ordinate of the universal graph (Figure 2.1). Since θ_{50} was already known, the core radius is calculated with the value of α_{50}, at the known operating wavelength (633nm). Since V parameter and core dimension is obtained, the corresponding numerical aperture $(\sqrt{n_1{}^2 - n_2{}^2})$ is calculated for each ESM PCF. Further, using refractive-index of core$(n_1 = 1.457)$ at 633nm [77] obtained from Sellemier formula, effective refractive index of cladding $(n_2 = n_{clad})$ is calculated using the value of numerical aperture.

2.4   Characterization Results and Discussion

The core radius is obtained by universal graph (Figure 2.1) and these values are verified with the SEM measurement and are found to be in agreement with each other for the three different sample of ESM PCF.

The V-parameters for each fiber is obtained from the universal graph (Figure 2.1), using the experimental value of corresponding $sin\theta_{10}/sin\theta_{50}$ and is verified with the values calculated from IEIM.

The numerical aperture $(\sqrt{n_1{}^2 - n_2{}^2})$ is calculated using the above obtained values of V-parameters for respective fibers and corresponding core radius and are verified with the calculated by IEIM and.

The calculated effective refractive index of cladding for each ESM PCF and the numerical aperture and are verified with the results obtained from IEIM.

The Experimental characterization results obtained for the geometrical and waveguiding parameters of ESM PCFs are found to be in good agreement with the results obtained using improved effective index method (IEIM) and scanning electron microscope (SEM) data. The experimental and simulation results obtained for characterization of ESM-PCFs have been compared and tabulated in table 2.1. The small variation the experimental results and the simulation results are due to experimental error in the measurement of angles θ_{10} and θ_{50}.

Table 2.1: Geometrical and waveguiding parameters of each PCFs obtained from IEIM, SEM and Experimental results obtained from far field measurements.

	IEIM(a)/ Measured from SEM (b)		Experimental Results
V-parameter	**ESM-12-01**	**2.8268 (a)**	**2.725 ± 0.06**
	LMA-10	**2.9540 (a)**	**2.701 ± 0.05**
	LMA-15	**2.9703 (a)**	**2.775 ± 0.05**
Core Diameter (micrometer)	**ESM-12-01**	**7.18 (b)**	**7.01 ± 0.05**
	LMA-10	**8.95 (b)**	**8.62 ± 0.04**
	LMA-15	**13.84 (b)**	**13.59 ± 0.04**
Numerical Aperture	**ESM-12-01**	**0.055972 (a)**	**0.038829 ± 0.001100**
	LMA-10	**0.074013 (a)**	**0.063246 ± 0.001400**
	LMA-15	**0.048275 (a)**	**0.041360 ± 0.000800**
Effective Refractive index of cladding (n_{clad})	**ESM-12-01**	**1.4560 (a)**	**1.45648 ± 0.04100**
	LMA-10	**1.4552 (a)**	**1.45562 ± 0.03200**
	LMA-15	**1.4562 (a)**	**1.45641 ± 0.02800**

2.5 Conclusion

It is observed that the transmission characteristics i.e. core diameter, *V*-parameter, Effective refractive index of cladding and numerical aperture obtained from far field measurement match with the SEM data and simulation results using IEIM within the experimental limits. Thus, characterization of ESM-PCFs from its far field radiation pattern measurement provides a useful tool for online characterization of ESM PCFs. It is expected that this method will serve as standard technique to characterize ESM PCFs and will also be useful to design and develop application specific ESM PCFs in optical communication systems.

Chapter 5

CHAPTER 3

Characterization of specially designed Polarization Maintaining Photonic Crystal Fiber[2]

3.1 INTRODUCTION

In chapter two, characterization of ESM PCFs from its far field radiation pattern is expounded. After the successful development of characterization technique for ESM-PCFs from its far field radiation pattern measurement now its turn to develop the characterization technique for application specific PCFs. In the present chapter, the theory and experimental characterization technique for a specially designed Polarization Maintaining (PM) PCF from its far filed intensity measurements is developed and described. Transmission characteristics of the sample PM PCF depends on the geometrical (core radius of major and minor axes of PM PCFs, air hole diameters, etc.) and waveguiding (e.g., Mode Field Diameter (MFD), cladding effective refractive index, V-values along major and minor axes and birefringence etc.) parameters of PM PCF. Therefore the knowledge of these waveguiding and geometrical parameters are required to assess the performance and transmission characteristics of PM PCFs. In the present chapter, first the theory for the characterization of sample PM PCF from far field intensity measurements is developed and discussed. After that from the experimental measurements of the far-field intensity pattern, all the transmission characteristics parameters of PM-PCF in terms of Mode Field Diameter (MFD), cladding effective refractive index and V-values along major and minor axis, Mode Field Area, Birefringence, Core radius & Numerical Apertures of major and minor axis of PM PCFs are calculated. The experimental measured values of geometrical and waveguiding parameters are found to be in agreement with the simulation, Scanning Electron Microscope (SEM) and manufacturer data for this PM-PCF.

---

[2] Part of the results reported in this chapter has been published in the paper- "Characterization of specially designed Polarization Maintaining Photonic Crystal Fiber from far field radiation patterns", Optics Communications (Elsevier, Science Direct), vol. 283, pp. 5007-5011, 2010.

3.2 Characterization of PM PCFs from Far-Field: Theory

In this chapter the far field intensity measurements is used for the estimation of waveguiding and geometrical parameters of PM-PCF. Recently a special PM PCF have been fabricated using two different air hole diameters along two orthogonal axes near the core region, which provides an effective index difference between two orthogonal polarization modes and their transmission characteristics exhibiting high birefringence in the order of 10^{-3} [78-81]. Figure 3.1 shows the SEM image of the sample PM-PCF.
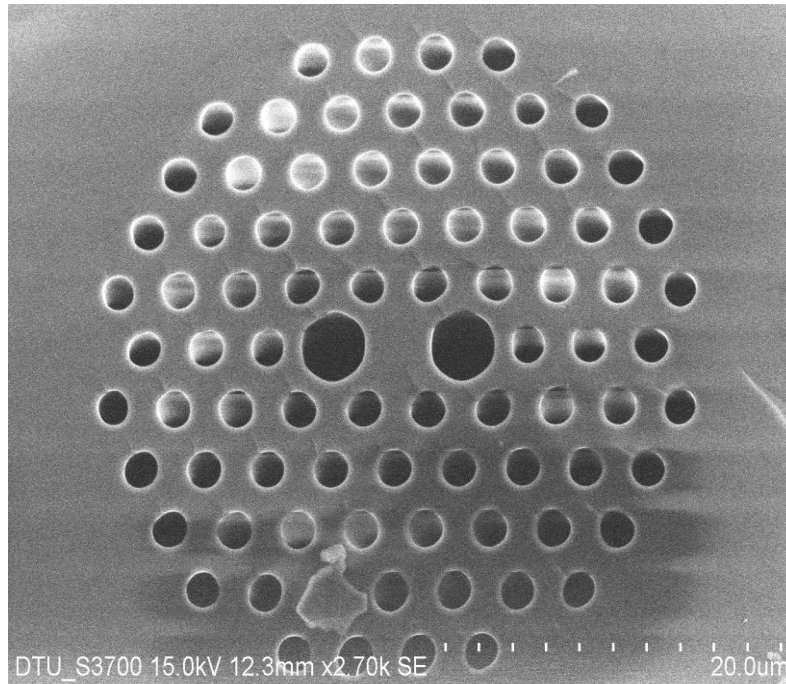
Figure 3.1: SEM image of the sample PM-PCF

The cross sectional views of the spot size of the sample PM-PCF is found to be elliptical in its near and far field regime and hence it is considered as an elliptical core fiber. Figure 3.2 shows the Far field pattern of PM-PCF.
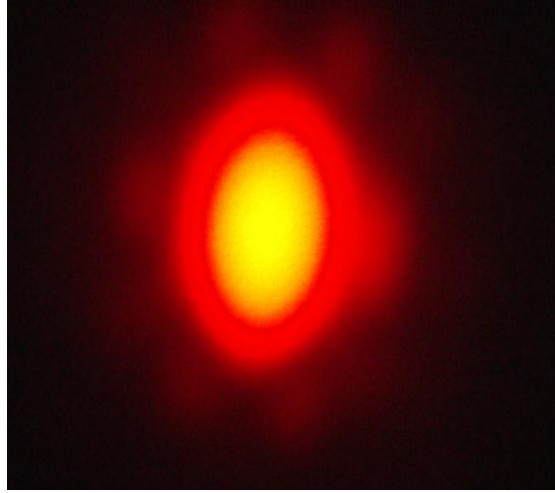
Figure 3.2: Far field pattern of PM-PCF

The elliptical cross section of PM PCF is accurately approximated to an equivalent Rectangular Core Waveguide (RCW) having the same aspect ratio, core areas and core-cladding refractive index difference [82-83]. Figure 3.3 depicts the approximation of transverse cross section of elliptical core with its equivalent pseudo same rectangular core waveguide having same refractive index profile.
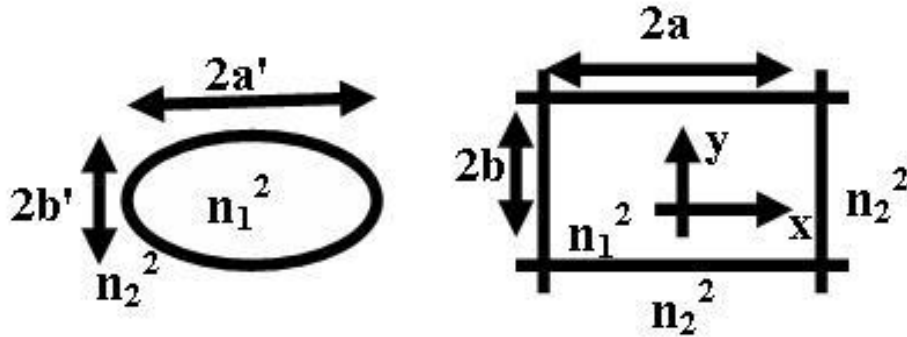
Figure 3.3: Transverse cross section of elliptical core with its equivalent pseudo rectangular core waveguide

The above approximation helped in deriving the far field intensity expression for the PM PCF from rectangular waveguide far field distribution.

Refractive Index Profile of elliptical core can be given by following equations [82]

$$n^2(x,y) = n_1^2, \quad \text{for } \left(\frac{x^2}{a^2} + \frac{y^2}{b^2}\right) < 1.0$$

$$n^2(x,y) = n_2^2, \quad \text{for } \left(\frac{x^2}{a^2} + \frac{y^2}{b^2}\right) > 1.0$$

Further, approximated pseudo rectangular core waveguide have following refractive index distribution:

$$n^2(x, y) = n'^2(x) + n''^2(y) - n_1^2$$

Where,

$n'(x) = n_1$ for $|x| < a$ and, $n''(y) = n_1$ for $|y| < b$

      $= n_2$ for $|x| > a$ $= n_2$ for $|y| > b$

Where, $a/a' = b/b' = \sqrt{\pi/2}$, as Area of ellipse ($\pi a'b'$) =Area of rectangle (4ab). For a symmetric slab waveguide (i.e. X –polarized and Y-Polarized cross section) the normalized (with respect to θ=0) far-field intensity distribution for the fundamental TE mode is given by following equations [84]

$$I(\theta) = |\psi|^2 = \left[\frac{U^2W^2}{\left(U^2 \text{-} \alpha^2\right)\left(W^2 \text{+} \alpha^2\right)} \left\{ \cos(\alpha)\text{-}\alpha\sin(\alpha)\frac{\cos U}{U\sin U} \right\} \right]^2 \quad \text{for} \quad U \neq \alpha$$

$$I(\theta) = |\psi|^2 = \left[\frac{U^2W^2}{\left(2V^2\right)\left(U\sin(U)\right)} \left\{ \cos^2(\alpha)+\sin^2(\alpha)+\frac{\sin 2\alpha}{2\alpha} \right\} \right]^2 \quad \text{for} \quad U = \alpha$$

Where, $V^2 = U^2 + W^2$; $\alpha = ka\sin\theta$; $k = \frac{2\pi}{\lambda_o}$; λ_o is the free-space operating wavelength and 'a' is the half-thickness of the core along the respective axes. The TE mode of the far field intensity is being used as the transcendental equation, as unlike TM modes, propagation does not depend on refractive indices directly for TE mode [5, 84]. The universal curve for far field radiation pattern of the slab waveguides is plotted using the above equations and the plotted universal curve is used for characterization of PM PCF. Figure 3.4 shows the variation in the ratio α_{10}/α_{50} and α_{50} with V parameter for slab waveguides.
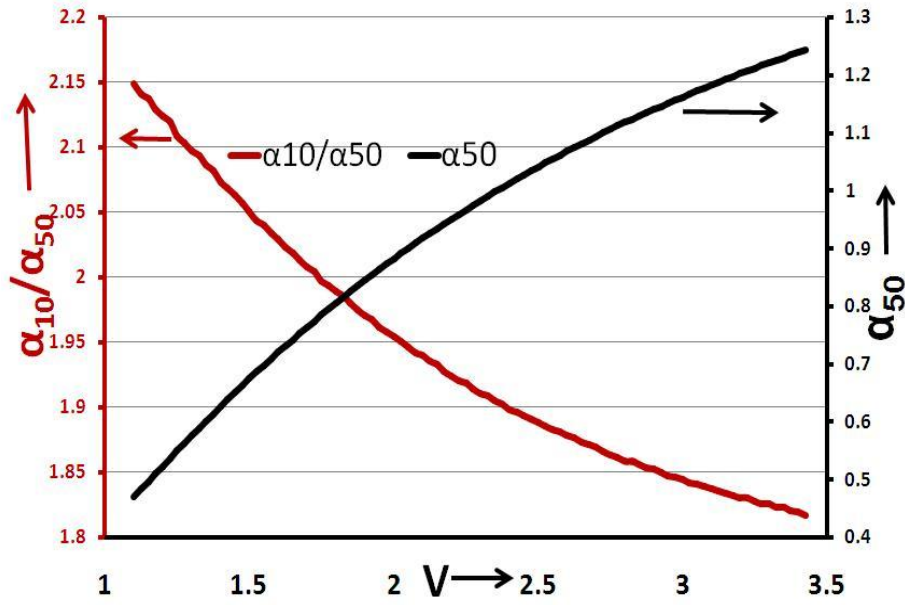
Figure 3.4: Variation in the ratio α_{10}/α_{50} and α_{50} with *V* parameter.

It is noted that α_{10} and α_{50} are the values of $\alpha = \text{ka}\sin\theta$ at corresponding angles at which the intensity dropped to 10% and 50% of its maximum value (at $\theta=0$) in the far field intensity pattern. The first minimum intensity position is measured at θ_{10} because it is practically very difficult to measure the first minimum intensity position accurately in far field intensity pattern [5].

3.3   Characterization of PM-PCFs from far-field: Experiment

The experimental setup for the characterization of PM-PCFs require a He-Ne laser with wavelength 633nm, Polarizer sheet (to find the polarization axes of laser as well as polarization of the output light from PM-PCF), sample PM PCF, fiber chuck and holders, microscopic lens, Silicon photo-detector (818-SL/Newport) with digital display.

To minimize the reflection losses at ends of PM PCF, ends are properly and carefully stripped and cleaved. The polarization axis of laser and fiber input-out ends has been found using the polarizer sheet. Silicon photo-detector (818-SL/Newport) is mounted on a calibrated circular mount at the circumference of the circular mount. Fiber output end is also fitted on the calibrated circular mount such that the fiber end is at the center of the circle. The least count of the calibrated circular mount was 0.1 degree

(6'). The Schematic diagram for experimental set to record the far field intensity pattern of PM PCF is shown in Figure 3.5 while the real time set up of the experiment is shown in Figure 3.6.
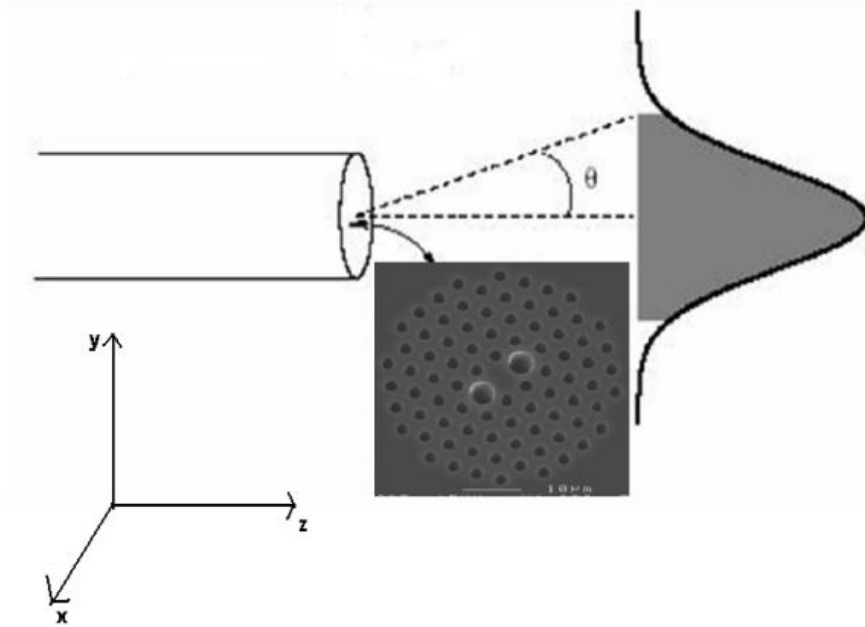
Figure3.5: Line sketch of far- field intensity pattern
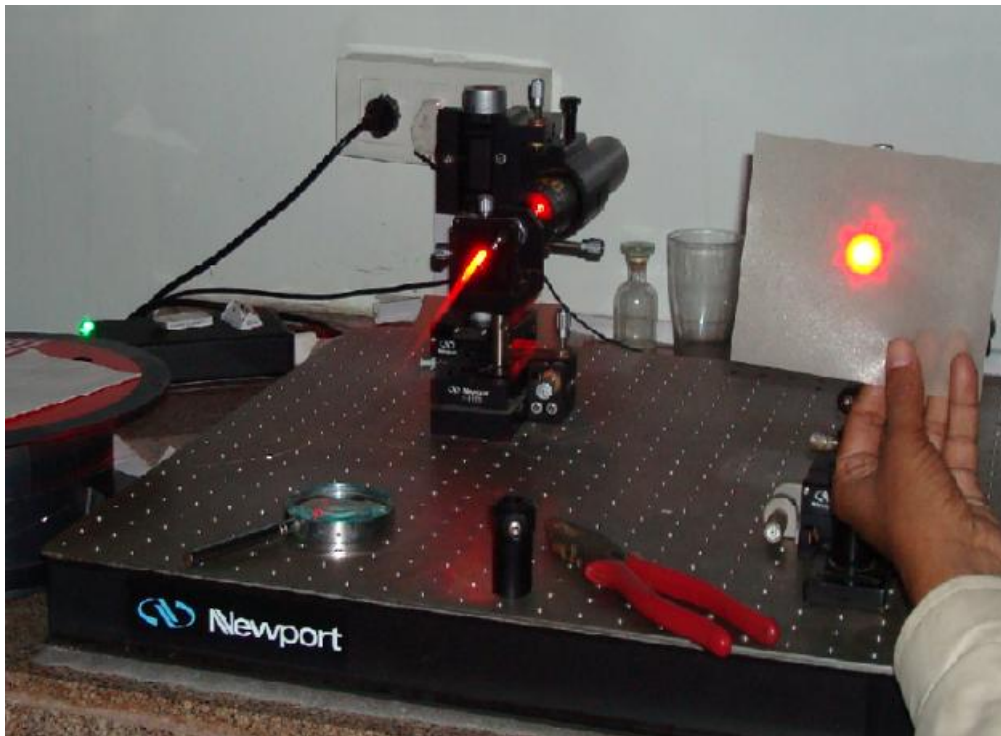
Figure 3.6: Real-time Experimental arrangement for far field measurement

The TE mode has been excited in the fiber and its far-field intensity pattern at output end is recorded with the help of photo detector by rotating the circular mount.

Figure 3.7: Measured far field intensity distribution along major axis.

Figure 3.8: Measured far field intensity distribution along minor axis

35

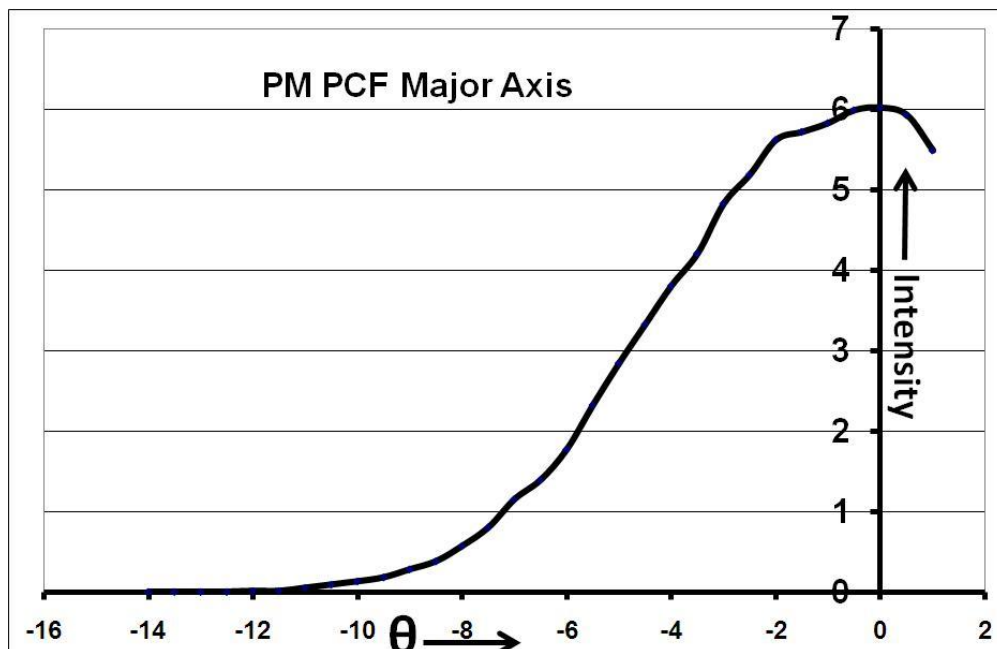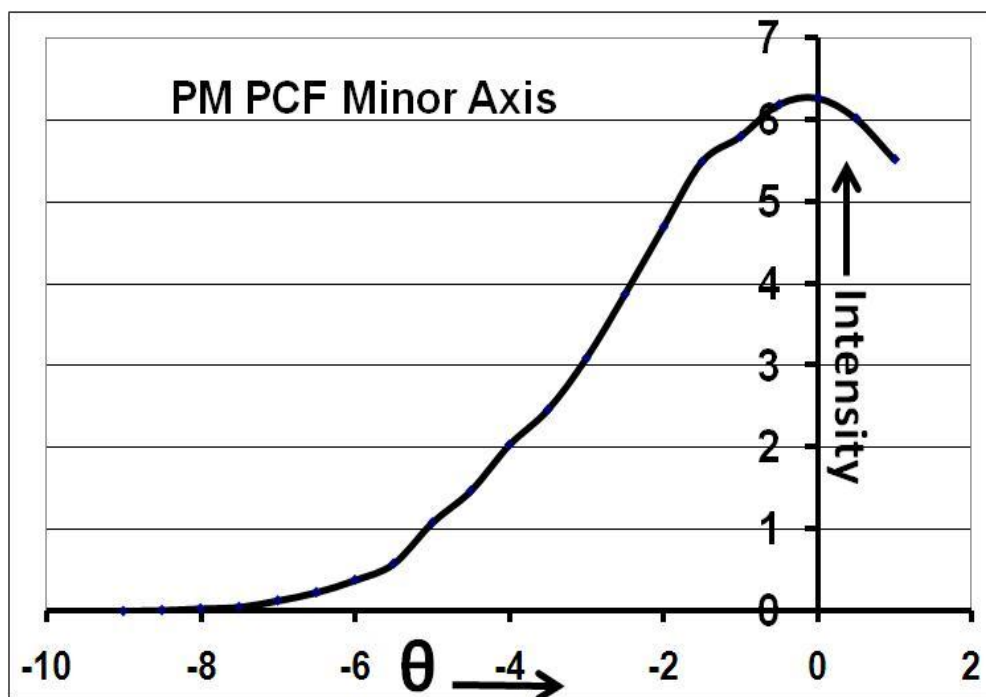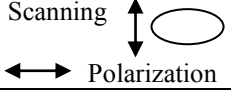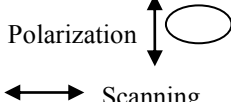The above measured far-field intensity variation shown in figure 3.7 and 3.8 corresponds to the far-field radiation pattern of fundamental TE mode of the PM-PCF along major and minor axis respectively. From the above plotted curves the θ_{10} and θ_{50}; the angles at which the intensity has dropped to 10% and 50% of its maximum value (at $\theta=0$) is obtained along the corresponding axes. Using these results the ratio $\sin\theta_{10}/\sin\theta_{50}$ is calculated along both the axes and are shown in table 3.1

Table 3.1: Scanning data along the major & minor axis of the far-field

Figure (Far- field)	θ_{10}	θ_{50}	$\alpha_{10}/\alpha_{50} = \sin\theta_{10}/\sin\theta_{50}$	$\alpha_{50} = k_0 a \sin\theta_{50}$
Scanning ↕ ⬯ ⟷ Polarization	5.5°	3°	1.8313	1.198
Polarization ↕ ⬯ ⟷ Scanning	8°	4.25°	1.87796	1.068

Corresponding to experimental values of $\sin\theta_{10}/\sin\theta_{50}$ along both axes the V values are obtained from the universal graph for the slab waveguide. For the respective V numbers the corresponding $\alpha_{50}(=k_0 a\sin\theta_{50})$ is calculated from the right hand ordinate of the universal graph. The core radius along the respective axes is calculated from the value of α_{50}, as θ_{50} and the operating wavelength was already known. Thus, by measuring far field intensity angles at which the intensity has dropped to 10% and 50% of its maximum value, the core-radius for the pseudo rectangular waveguide are calculated. From this data, the core dimension of the elliptical core of this PM PCF has been calculated using aspect ratio for pseudo rectangular waveguide and elliptical PM-PCF i.e. , $a/a' = b/b' = \sqrt{\pi/2}$.

Since V parameter and core dimension is obtained, the corresponding numerical aperture ($\sqrt{n_1{}^2 - n_2{}^2}$) is calculated along both the axes. Further, using refractive-index of core($n_1 = 1.457$) at 633nm obtained from Sellemier formula, effective refractive index of cladding ($n_2 = n_{clad}$) is calculated using the value of numerical aperture.

Once the effective refractive index of cladding ($n_2 = n_{clad}$) is calculated, the effective refractive index of the guided mode(n_g) along the two orthogonal axes of PM-PCF is calculated with the simulation using the R-Soft. After the knowledge of

effective refractive index of the guided mode along two mutually orthogonal axes, the Birefringence ($n_{gx} - n_{gy}$) induced in the sample PM-PCF is obtained.

Further, the experimental value of θ_e (the angle where the far-field intensity falls to $1/e^2$ of the maximum intensity) is obtained from the measured far-field intensity curve. The MFD of propagating light wave is obtained with the help of the formula of $MFD = 2 \lambda_o/\pi\sin\theta_e$ for both the axes [85].

From the calculated values of MFD of PM-PCF along two orthogonal axes, the mode-field area ($= \pi xy/4$) is calculated; where x, y are the MFD of PM-PCF along the two orthogonal axes.

3.4   Characterization Results and Discussion

It is mentioned that the major axis in the near field becomes minor axis in far field and the minor axis in near field becomes major axis in far field, which is expected also from diffraction phenomena. The experimental result of MFD along both the axes is found to be in close agreement with the manufacturer data within the experimental limits.

From the experimentally obtained value of MFD for both axes, Mode Field Area is obtained and is also found to be in close agreement with the manufactures data.

Core radius along two axis i.e. semi major and semi minor axes is obtained using universal graph and these values are verified with Scanning Electron Microscope (SEM) measurement.

The V-parameters of the PM-PCF along both axes is obtained from universal graph, using the experimental value of $\sin\theta_{10}/\sin\theta_{50}$ and is verified with the simulation result of R-Soft Band solver.

The numerical aperture ($\sqrt{n_1{}^2 - n_2{}^2}$) along the two axes is calculated using the above obtained value of V-parameters & the core radius and are verified with the simulation result of R-Soft Band solver.

The effective refractive-index of cladding for given PM PCF along the two axes is calculated using core refractive-index (n_1) = 1.45 and the numerical aperture and are verified with the simulation result obtained from R-Soft Band solver.

The experimental effective refractive index of the guided modes (n_g) along the two orthogonal axes is obtained with the R-Soft using the experimentally obtained effective refractive index of cladding. These values are verified with simulation result of R-Soft Band solver.

The Birefringence ($n_{gx} - n_{gy}$) induced in the given PM-PCF is obtained from effective refractive index of the guided mode along two mutually orthogonal axes and is verified with the simulation result of R-Soft Band solver, where it is shown that the birefringence is in the order of 10^{-3}.

Experimental results for the determination of waveguiding and geometrical parameters for given PM PCF are found to be matching with manufacturer /simulation results by Plane wave expansion method using the R-Soft Band solver as well as from the SEM measurements, which have been compared and tabulated in table 2. "Axis-1" is the axis along big air holes act as minor axis in near field and major axis in far-field and hence yields lower effective refractive index in cladding along big air holes, similarly "Axis-2" is the axis along regular air holes act as major axis in near field and minor axis in far field and yields larger value of effective refractive index in the cladding. As a result modal birefringence is introduced.

Table 3.2: Comparison between Manufacturer/Simulation/SEM data and Experimental Results

	Manufacturer's-(k)/ Simulation data(l)/ Measured from SEM (m)		Experimental Results
MFD (μm)	Axis-1(x)	3.1 (k)	3.08
	Axis-2(y)	3.6 (k)	3.79
Mode Field Area(μm^2)	πxy/4	8.7606 (k)	9.163462
Core Radius (μm)	Axis-1	b'=1.445 (m)	b=1.28754, b'=1.45284
	Axis-2	a'=2.285 (m)	a=2.0454, a'=2.3080
Effective Refractive index of cladding (n_{clad})	Axis-1	1.43298 (l)	1.43860
	Axis-2	1.44086 (l)	1.44335
Effective Refractive index of guided mode (n_g)	Axis-1	1.445459 (l)	1.445212
	Axis-2	1.447837 (l)	1.447869
Birefringence	0.002378 (l)		0.002657
V-parameter	Axis-1	2.8295 (l)	2.650
	Axis-2	3.2985 (l)	3.175
Numerical Aperture	Axis-1	0.22151 (l)	0.18146
	Axis-2	0.16254 (l)	0.13871

3.5 Conclusion

Far-Field method is applied to characterize PM PCF. Assuming the elliptical core of PM PCF as an equivalent rectangular waveguide, first the parameters for the equivalent rectangular/slab waveguides are found. Then with the suitable approximation we calculated and characterized the PM PCF. The Experimental result so obtained matches with the manufacturer/ Simulation/SEM data within the experimental limits. Thus, this method provides us a useful tool for online

characterization of PM PCF. It is expected that this method will serve as standard technique to characterize PM PCF and will also be useful to design and develop application specific PM PCF both in optical communication and in sensor systems.

Chapter 4

CHAPTER 4

Design, fabrication and characterization of tunable negative refractive index metamaterial[3]

4.1 INTRODUCTION

In last two chapters, characterization technique for the different application specific photonic crystal fiber is presented. In the present chapter, Design, fabrication and characterization of a new tunable photonic device called Metamaterial is discussed. Due to their highly uncommon electromagnetic properties and application such as negative refraction, flat lens, Cloaking, reverse Doppler Effect etc; Metamaterials are in the prime focus for past few years with the number of publications and patents, increasing exponentially.

All known naturally found transparent materials have positive electric permittivity (ε_r) and magnetic permeability (μ_r) and by convention the positive value of refractive index (n) is taken in account [35-37]. In case of artificially designed metamaterial, both electric permittivity and magnetic permeability is negative, which results n real and under this situation negative square root for n is taken into account (negative refractive index). The main challenge in the design of metamaterials is to design a structure which shows electric permittivity and magnetic permeability simultaneously negative for the desired frequency range within its characteristic size [35-37, 42]. It becomes possible to design metamaterials due to the dispersive nature of materials i.e. electric permittivity and magnetic permeability is function of the radiation frequency.

Due to the rapidly-developing sub-wavelength techniques and Nano-fabrication facility, different types of metamaterials structures (such as square, Ω- shaped, circular, U-shaped, S-shaped, asymmetric-rings and asymmetric-rings) is designed for different applications purpose [52-58]. Almost in all cases, metamaterials are fabricated as periodic arrays of metallic structures whose dimensions are smaller than the wavelength of radiation. The overall electromagnetic response of the entire

---

[3] Part of the results reported in this chapter has been published in the paper-"Tunable negative refractive index metamaterial from "V" shaped SRR structure: Fabrication and Characterization", Journal of the Optical Society of America B (OSA) Vol. 31 No. 7, pp 1410-1414, 2014.
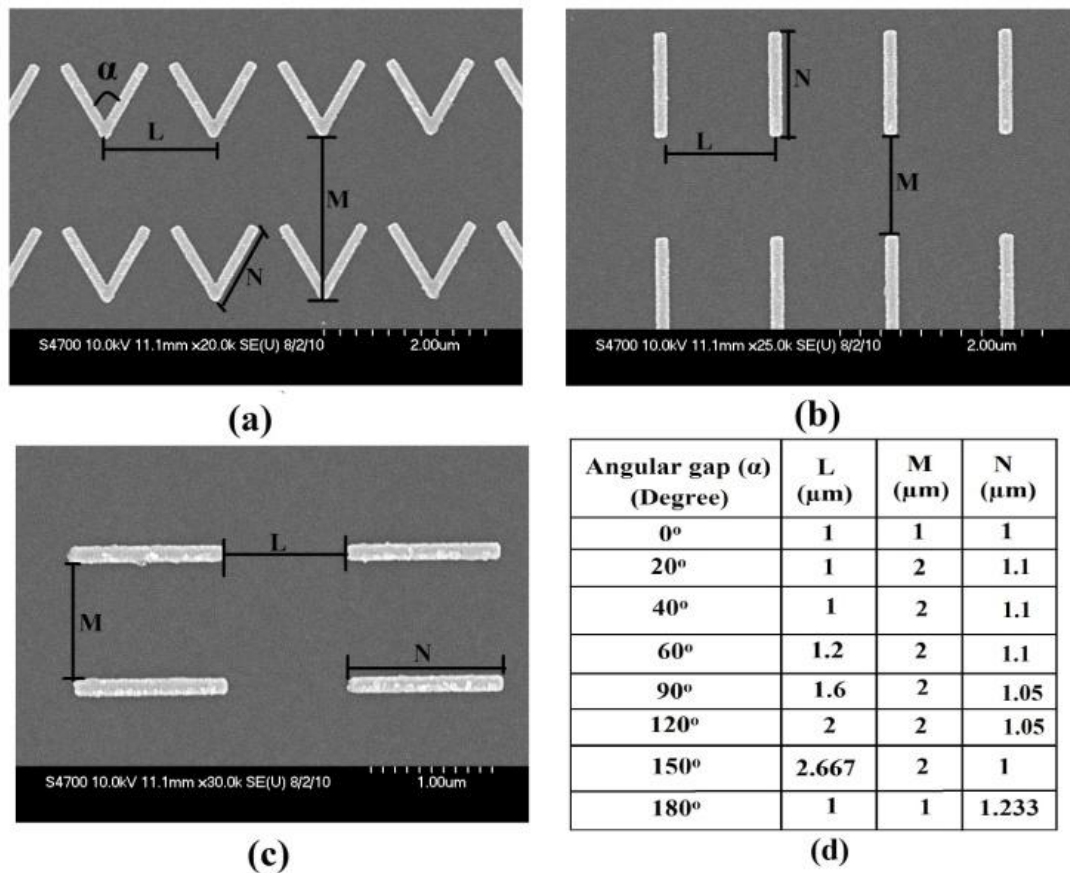
material is determined by the collective oscillations of conducting electrons in these metallic structures (known as localized surface Plasmon) [86-90, 92-93]. To achieve a customized electromagnetic response, the dimensions and geometries of these metamaterial unit cells is to be adjusted. The "C" shaped Split Ring Resonator (SRR) is the most common element used in forming the basic microstructure of metamaterials resonating in the infrared regime [86-90]. In case of normal incidence with TE polarization mode, when incident electric field across its gap, the electric field couples with the capacitance of the SRR and generates a circulating current across it. A magnetic field is induces at the bottom of the SRR by this circulating current. This induced magnetic field interacts with the external field to generate the magnetic resonance identified as an LC resonance by Linden et al [91]. The LC resonance ($\omega_{lc} = 1/\sqrt{LC}$) of the SRR is inversely proportional to the size (dimension) of SRRs. In case of TM polarization mode, when the electric field is perpendicular across the SRR gap, no LC resonance only with the plasmon resonance being present as there is no circulating current could be produced.

In this chapter, Fabrication and characterizations of a "V" shaped SRR metamaterial is described and also shown the angular gap dependent tunable negative refractive index (NRI) characteristics. The unique property of this structure is that by varying the angular gap between its arms, the capacitance (C) for the structure can be changed and hence the negative refractive index can be tuned and controlled as per requirement. The interdependence of the capacitance (C) and inductance (L) of the structure is experimentally and computationally investigated and it is observed that by changing the angular gap of V shaped SRRs it is possible to control/tune their negative refractive index at the corresponding resonance wavelength. Exploiting this important result for the extraordinary electromagnetic properties of the reported structure, this structure can be used for tuneable metamaterial devices e.g. the design of receiver and transmitter antenna for the desired frequency/application range.

44

4.2   Design and Fabrication

On the n-doped silicon substrate having an area of ~300 x 300 μm, two dimensional array of ~50 nm thick gold based V shaped SRRs were fabricated using a combination of Electron Beam Lithography (EBL) technique and metal lift-off. The width of the arms for "V" shaped structure was kept at ~0.1μm and the arm length at ~1μm. Eight different sample of reported structure with angular gap of 0°, 20°, 40°, 60°, 90°, 120°, 150° and 180° is fabricated and studied.

Figure 4.1 shows the geometry and dimensions of the reported structure. Fig. 1(a) shows the geometry of the structure for angular gap of α° (α may be 20°, 40°, 60°, 90°, 120°, 150°); fig. 1(b) is for angular gap of 0° which look like single arm or longitudinally parallel rods; similarly fig.1(c) shows the structure for angular gap of 180° where both arm open in opposite direction and look like horizontally parallel rods. Fig.1 (d) charts the dimension of all the samples for different angular gap.

(a)

(b)

(c)

Angular gap (α) (Degree)	L (μm)	M (μm)	N (μm)
0º	1	1	1
20º	1	2	1.1
40º	1	2	1.1
60º	1.2	2	1.1
90º	1.6	2	1.05
120º	2	2	1.05
150º	2.667	2	1
180º	1	1	1.233

(d)
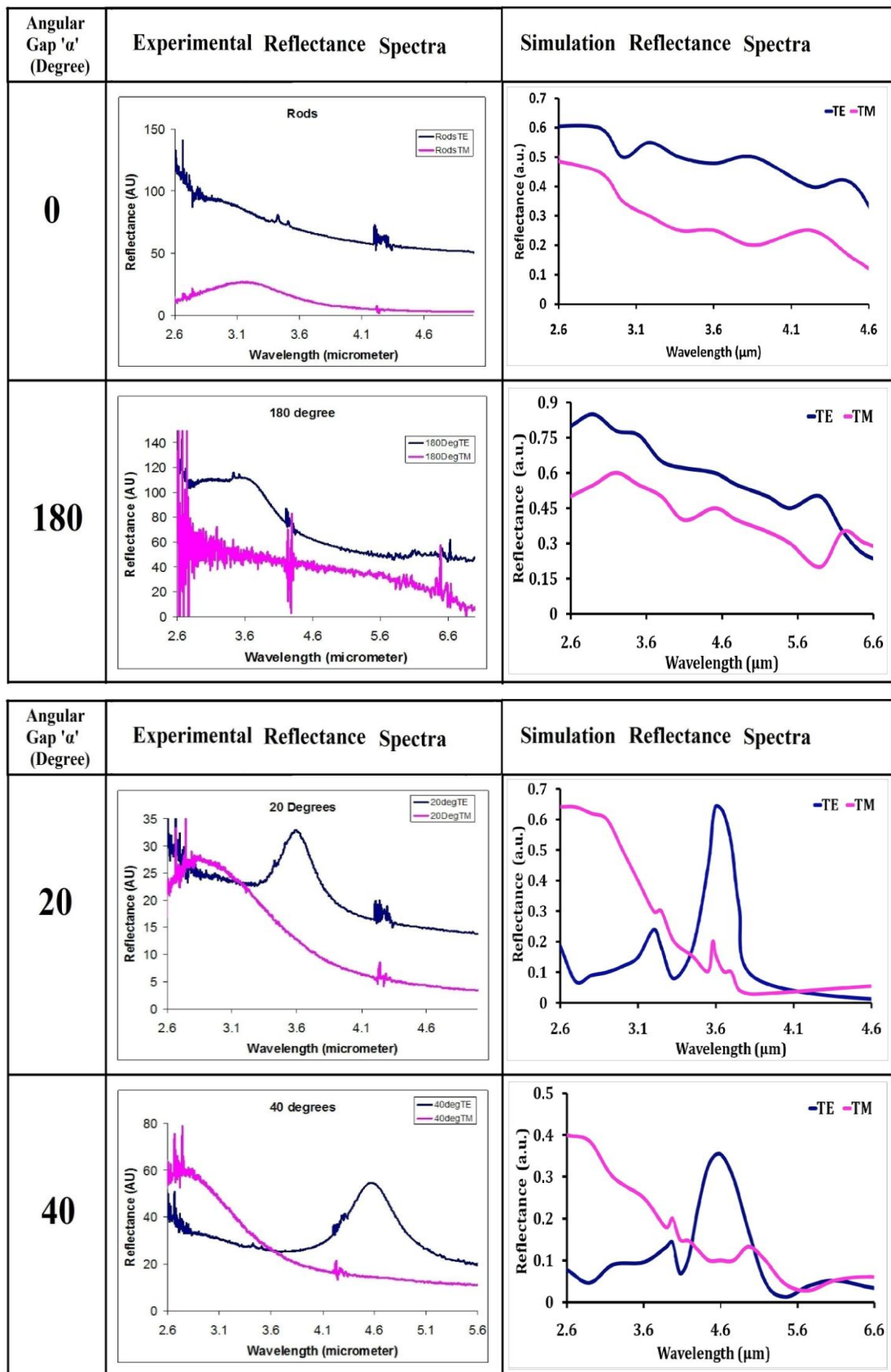
Figure 4.1: Geometry and Dimensions of the reported structure

4.3   Characterization Process

The reflectance measurements of all the fabricated structure were done using a Nicolet Continuum Fourier transform infrared (FTIR) spectroscope fitted with a case grain objective of 10 × magnifications and an NA of 0.25. A Zinc Selenide polarizer was used to polarize the incident light. The measurements were taken for both orthogonal linear polarizations of the incident light (TE and TM polarization) - and were then normalized with respect to the reflectivity of a bare silicon substrate. All measurements were taken at normal incidence.

Modelling and simulation for fabricated "V" shape metamaterial is performed using finite-differential-time-domain (FDTD) method of Omnisim simulation package from Photon Design, UK. The Drude model is used to describe the complex dielectric constant of the gold layer. The reflection and transmission spectra for the modelled structures are simulated as a function of wavelength.

The reflectance resonance response of TE and TM modes measured from Nicolet Continuum Fourier transform infrared (FTIR) spectroscope as well as obtained by Finite Difference Time Domain (FDTD) simulations of the structure are shown in Figure 4.2 (Blue curve is for TE mode, Pink curve is TM mode).

Angular Gap 'α' (Degree)	Experimental Reflectance Spectra	Simulation Reflectance Spectra
0		
180		

Angular Gap 'α' (Degree)	Experimental Reflectance Spectra	Simulation Reflectance Spectra
20		
40		

Angular Gap 'α' (Degree)	Experimental Reflectance Spectra	Simulation Reflectance Spectra
60		
90		

| Angular Gap 'α' (Degree)	Experimental Reflectance Spectra	Simulation Reflectance Spectra
120		
150		

Figure 4.2: Reflection spectra of both TE and TM polarization for all samples SRR structures

48

It is observed that the 0 degree and 180 degree angular gap samples (having minimum and maximum gaps) produced no significant resonance response as expected as they simply represent metallic rods instead of SRRs and. But for the structures with the angular gap (α) of 20°, 40°, 60°, 90°, 120° and 150°, the LC and Plasmon resonance response is significant and observable for the TE polarization mode with the electric field parallel across the SRR gap.

Figure 4.3 shows the significant shift in resonance (LC) peak with respect to angular gap for TE polarization (both experimental as well as simulated).

The most significant observation is that position of LC resonance peak the samples varying from 3.6 μm to 5.6 μm wavelength ranges by varying the angular gap from 20° to 150° respectively. These experimental observations were confirmed with the simulation results obtained from Omnisim FDTD simulation package within experimental limits.
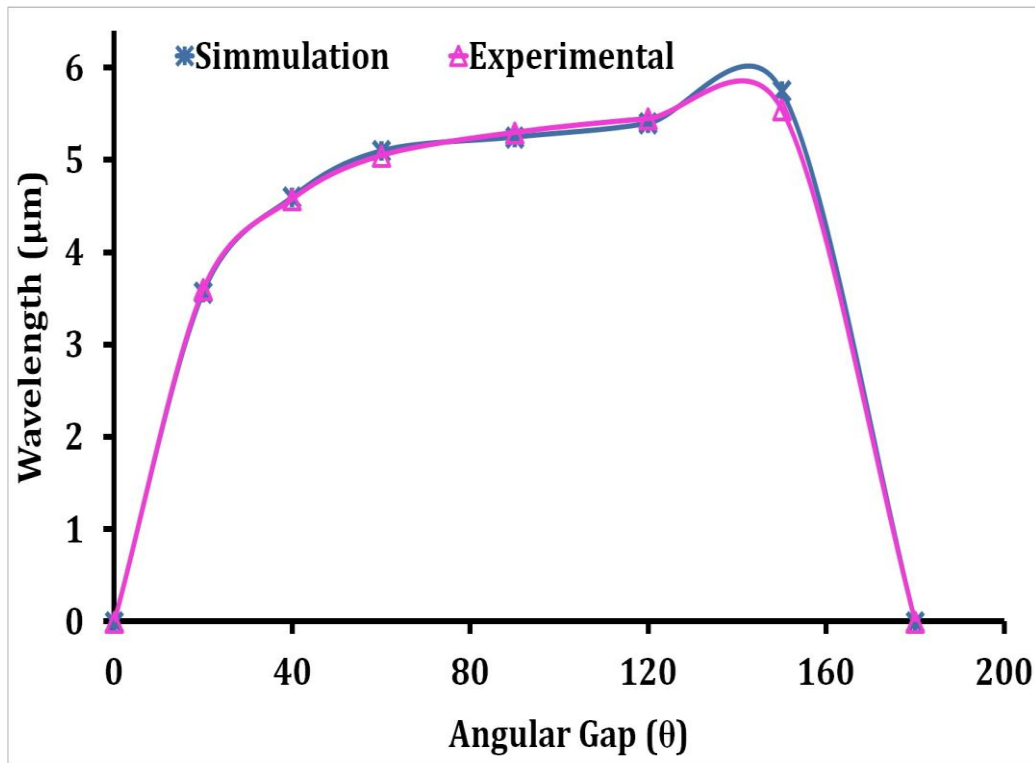
Figure 4.3: Position of LC peak with respect to angular gap.

4.4 Determination and analysis of Electromagnetic parameters

To the exploit of the amazing electromagnetic properties of metamaterial, it is require to characterize the metamaterial structure in terms of its electromagnetic parameters

such as real and imaginary value of electrical permittivity, magnetic permeability, refractive index and impedance etc. In the recent past several methods are used for the characterization of metamaterials and evaluating its electromagnetic parameters [94-102]. In this chapter, Yosuke et al. method [102] is used to compute the electromagnetic parameters by using the reflection and transmission coefficients obtained by simulation results and the following equations are used,

$$z^2 = \frac{T^2 - (1+R)^2}{T^2 - (1-R)^2} \quad \text{...................... (1)}$$

$$n = \frac{c}{i\omega d} \ln\left[\frac{(1+z)R}{(1-z)R} + \frac{1}{T}\right] \quad \text{.................... (2)}$$

$$T = Te^{(i\omega d/c)} \quad \text{.................... (3)}$$

$$R = -R \quad \text{.................... (4)}$$

$$\varepsilon = \frac{n}{z} \quad \text{.................... (5)}$$

$$\mu = nz \quad \text{.................... (6)}$$

Where T = Transmission coefficient, R = Reflection coefficient, d = effective thickness of the gold layer, c = velocity of light in vacuum, $\omega = 2\pi/\lambda$, z= impedance, n=refractive index, ε=electric permittivity, μ= magnetic permeability.

Using the above equations and the reflection and transmission spectrum, the variation in electromagnetic parameters w.r.t. wavelength for each structure is plotted in figure 4.4. It is easily observed in the electromagnetic parameters plots that electric permittivity and magnetic permeability for the structure is negative at the resonance wavelength, so the refractive index is also negative at the resonance wavelength. The entire curve plotted for the eight different samples are given below (Blue curve is for real part, Pink curve is for imaginary part).

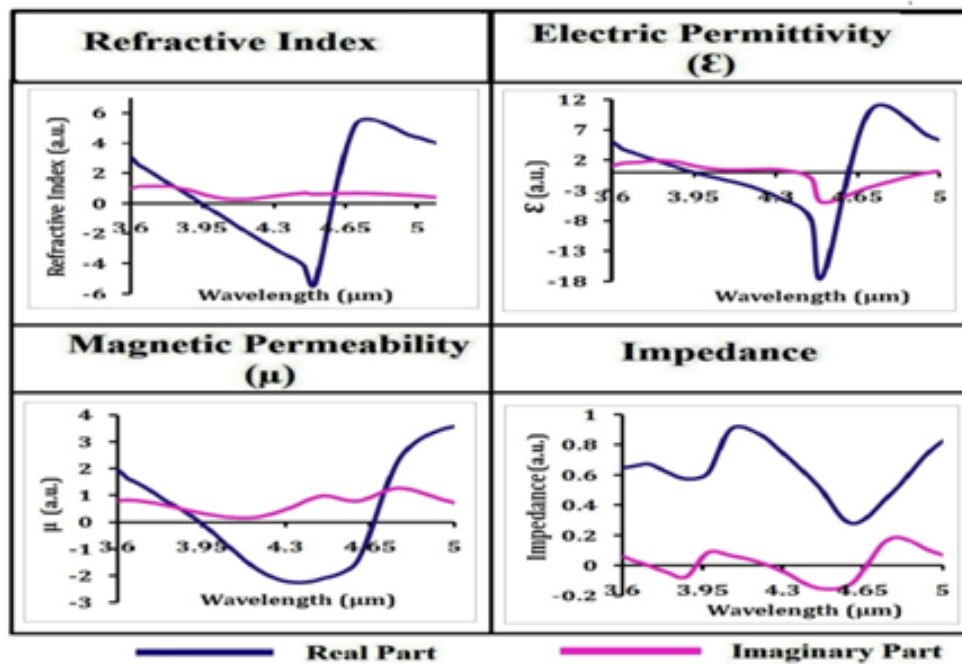Electromagnetic parameters for 0°
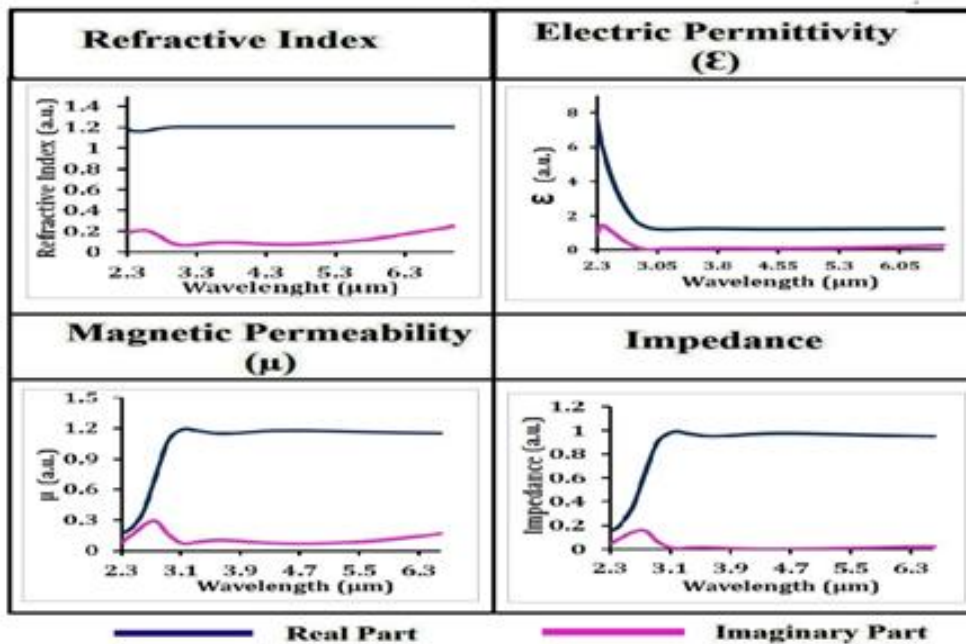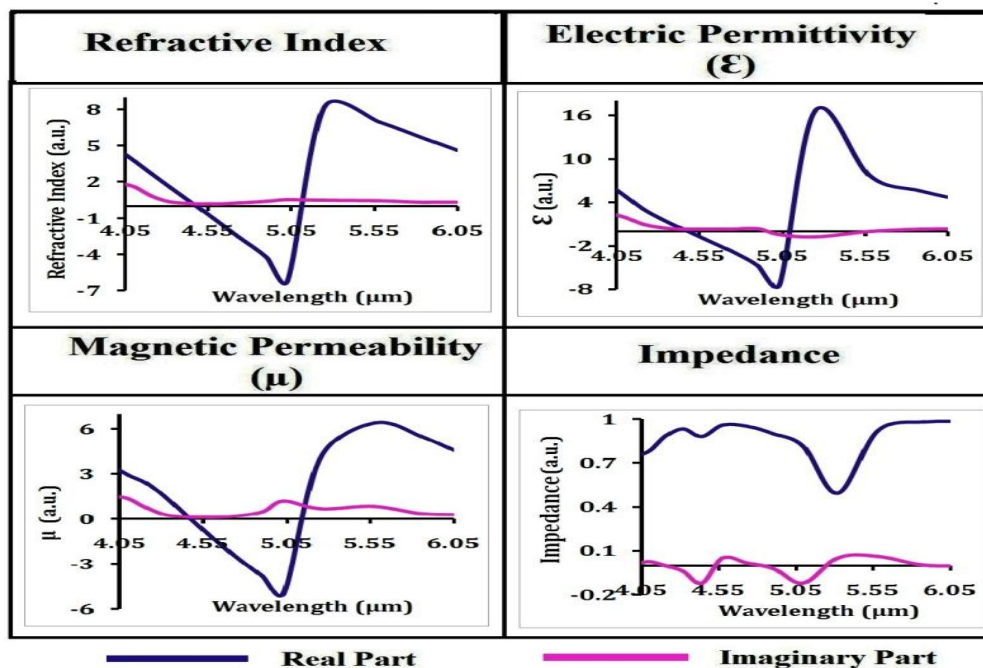

Electromagnetic parameters for 20°
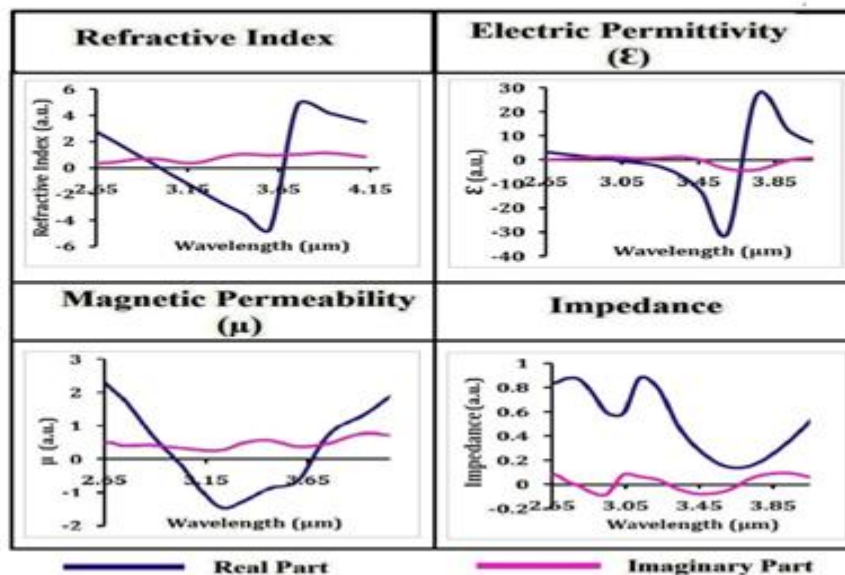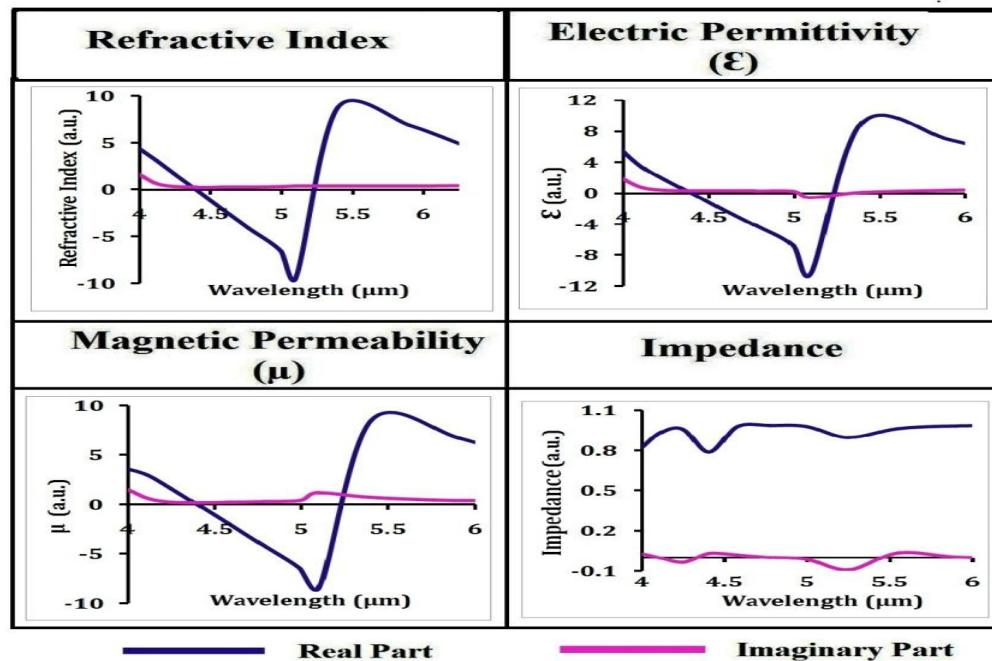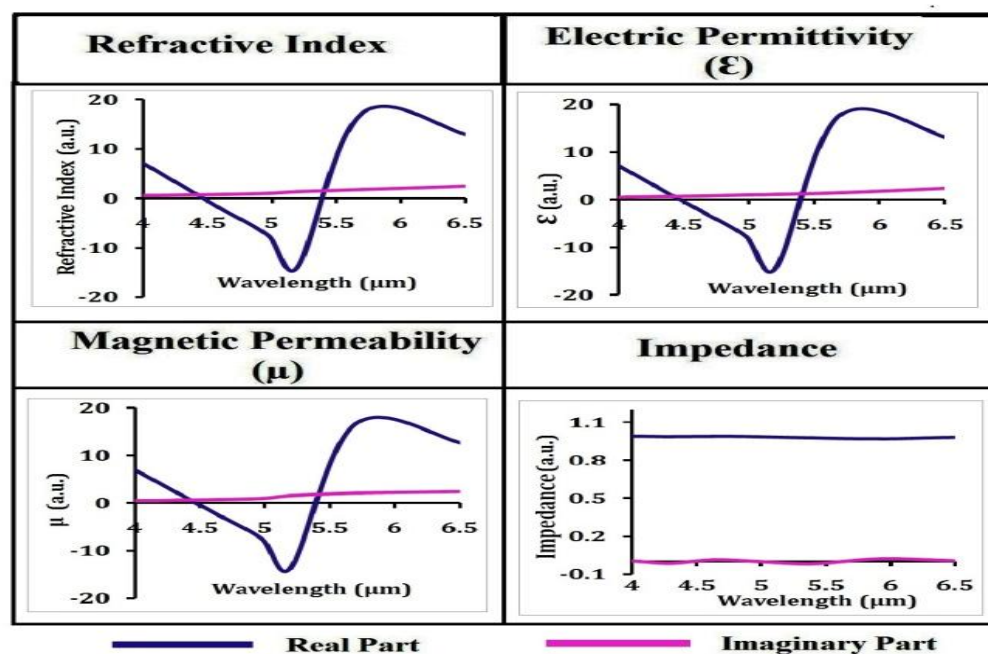
Electromagnetic parameters for 40°
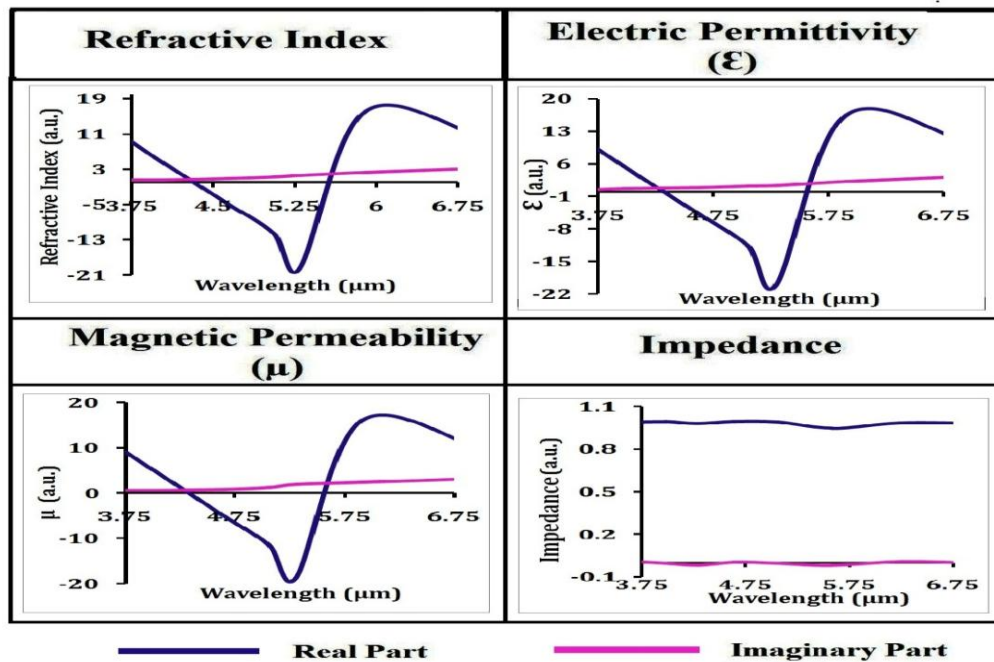

Electromagnetic parameters for 60

Electromagnetic parameters for 90

Electromagnetic parameters for 120

Electromagnetic parameters for 150

Electromagnetic parameters for 180
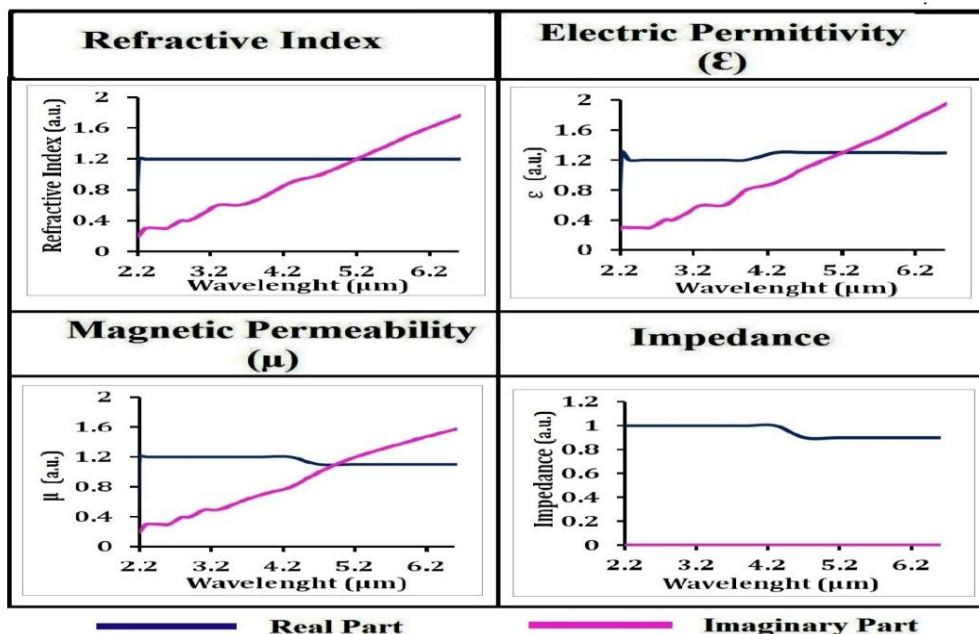
Figure 4.4: Electromagnetic parameter with respect to wavelength for sample SRR structures

54

From the above plotted curves the variation in negative refractive index is found for the respective angular gap and is plotted in figure 4.5 (below).
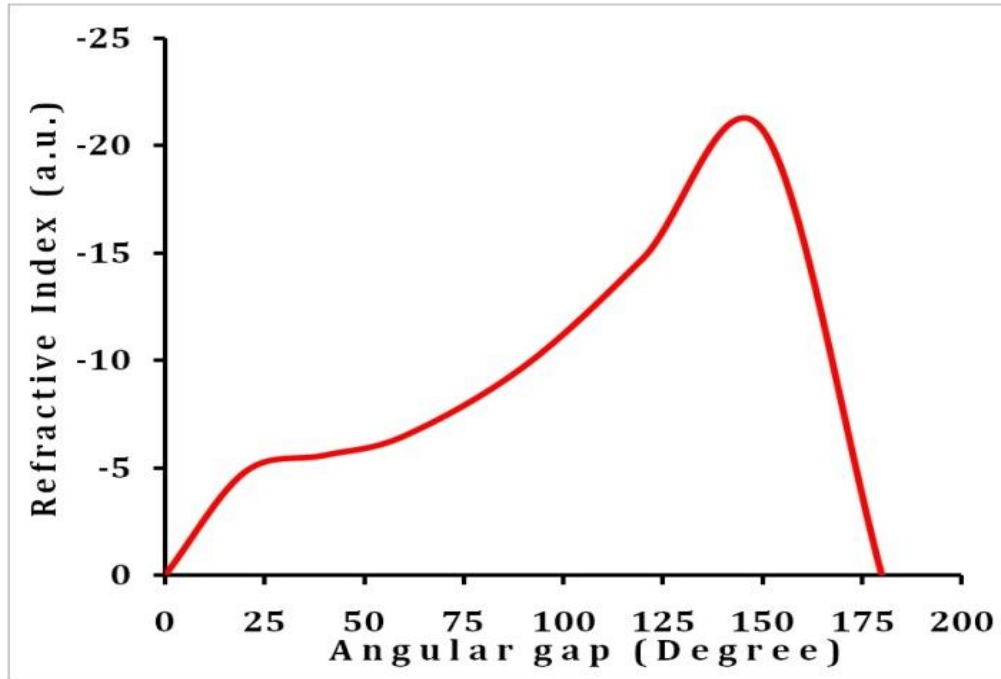
Figure 4.5: Plot of refractive index against different value of angular gap

From the above observations, it is clear that refractive index is negative for the reported structure at the LC resonance frequency. This observation confirms that our structure is behaving as negative refractive index metamaterial at corresponding resonant frequency.

Also from figure 4.4 and 4.5 it can be clearly seen that by changing the angular gap of the V shaped SRRs, their LC resonance position changes and negative refractive index of the structure increases constantly at the corresponding resonance position. This is significant for practical applications of negative index metamaterials in waveguides and cloaking because signals obtained near resonance response of materials tend to be very lossy and difficult for real life applications. In case of V shaped SRRs, we have the advantage of increasing the NRI just by increasing the angular gap. To the best of our knowledge, this facility cannot be harnessed in other structures e.g. the C shaped SRRs. This also proves that the electromagnetic parameters (such as permittivity and permeability) of metamaterial can also be tuned as per our requirement by varying the angular gap.

4.5   Conclusion

In this chapter, a new design of metamaterial structure similar as English letter "V" is fabricated and performed experimental and computational investigations of the structure. In this work, the behavior of a "V" shaped split ring resonator is described. By changing the angular gap of V shaped SRRs it is possible to vary the NRI of the structure. The experimental results are well corroborated by simulations to show that electromagnetic parameters (such as ε, μ, n etc.) can be tuned with the variation of the angular gap between the arms of V shaped SRRs. Thus, the reported structure for the metamaterial will put a significant mark in the design and development of metamaterials based optical switch, tunable devices and sensors etc.

Chapter 7

CHAPTER 5

Design and characterization of a Metamaterial Structure for Negative refraction in optical communication window around 1.55 µm[4]

5.1 INTRODUCTION

In the last chapter, Design, fabrication and characterization of V-shaped tunable Metamaterial is expounded. Now, in this chapter, the main focus is to design a Metamaterial Structure for Negative refraction in optical communication window. Also, after designing to characterize the structure to know the electromagnetic parameters like electric permittivity (ε), magnetic permeability (μ), impedance as well as the refractive index (n).

In almost all cases, SRRs are fabricated as periodic arrays of metallic structures with a dimension smaller than the wavelength of radiation so the collective oscillations of conducting electrons in these metallic structures (known as localized surface Plasmon) [86-90, 92-93] determine the overall electromagnetic response of the entire material. Metamaterials have characteristic dimensions of the order of the operating wavelength, with fabrication accuracies better than 10 nm. Now, due to this fabrication limit, metamaterial advantage is not being exploited in optical regime, as much it is well explored and exploited in microwave regime. A new planar metamaterials structure are being tailored to obtain the negative refractive index property in high frequency regime to overcome this difficulty in the fabrication of the metamaterials with the structures consisting a combination of split-ring resonator and metal wire [103-104]. These new planar metamaterials structures are well suited for most applications in terms of feasibilities of design and fabrication in the optical frequency regime [104-105]. They have also advantage in easy excitation and easy matching with conventional planar circuits.

---

[4] Part of the results reported in this chapter has been published in the paper "Design and Simulation of "I" shaped Split Ring Resonator metamaterial at optical communication window around 1.55 µm", Optik (Elsevier, Science Direct), IJLEO-D-14-01345 (Accepted) (2015)

5.2   Geometry and Design of the structure

In this chapter, design and simulation of "I" shaped metamaterial is described, which is showing negative refraction in the optical communication window around wavelength of 1.4 μm to 1.6 μm. The proposed metamaterial structure consisting of periodic arrays of gold split ring resonators (SRR) deposited on silicon substrate, with a minimum feature size of 100 nm.

Two dimensional array of 12 x 8 was formed on a 1.5 micron thick silicon substrate; gold strip of 0.6 micron thickness is used to form the proposed structure having the width 0.1 micron of gold strip. Figure 5.1 shows the geometry with its dimensions and the elementary cell of the proposed planar metamaterial. To get the optical frequency range, the 0.1 micron longitudinal and 0.4 micron horizontal gap between two successive proposed structure units is set as when two rings get closer then the resonance frequency is shifted to lower (44).
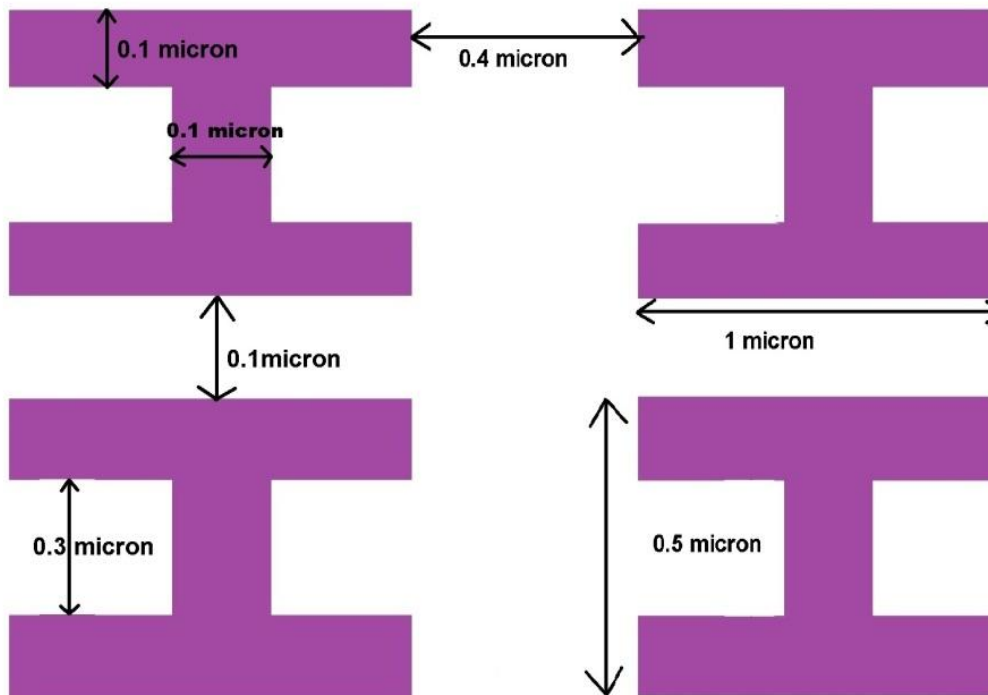
Figure 5.1: The geometry and dimensions of the reported structure

60

5.3 Modeling and characterization of the structure

The modeling and simulation of the reported "I" shape planar metamterial structure is done by using finite-differential-time-domain method (FDTD) of omnisim simulation package from Photon Design, UK. To describe the complex dielectric constant of the gold layer the Drude model is used. The propagation characteristics in terms of reflection and transmission spectrum as a function of wavelength of the reported structure are obtained using finite differential time domain (FDTD) method. Figure 5.2 showing the transmittance and reflectance resonance response for the proposed "I" structure with respect to the wavelength.

(a)

(b)
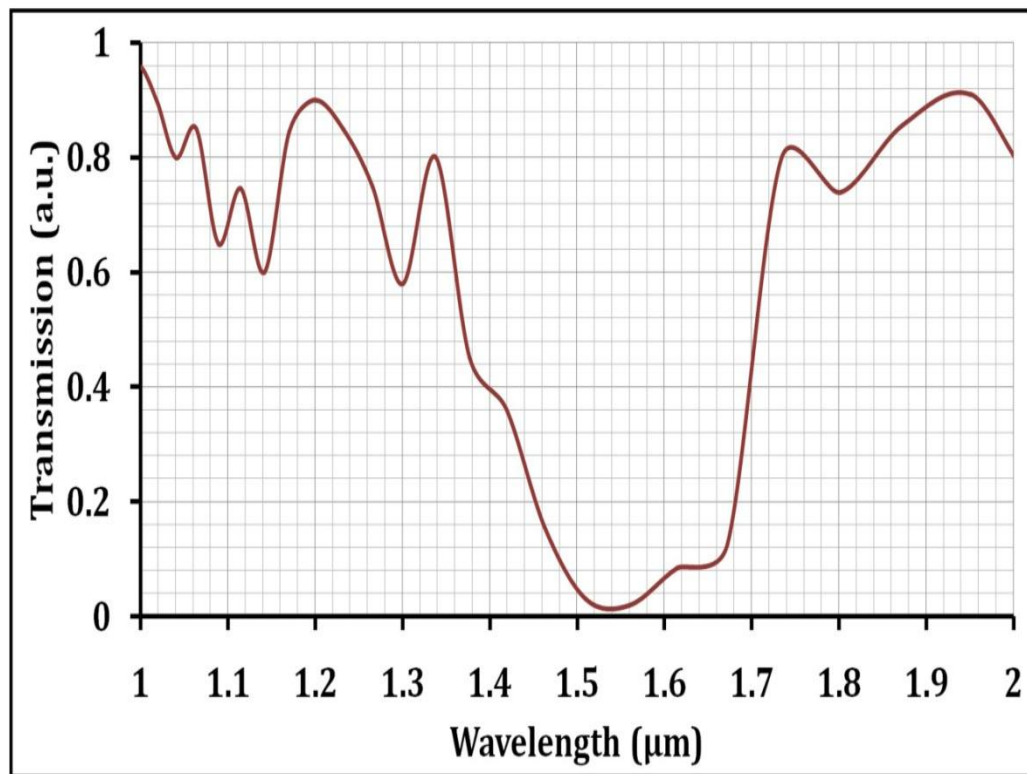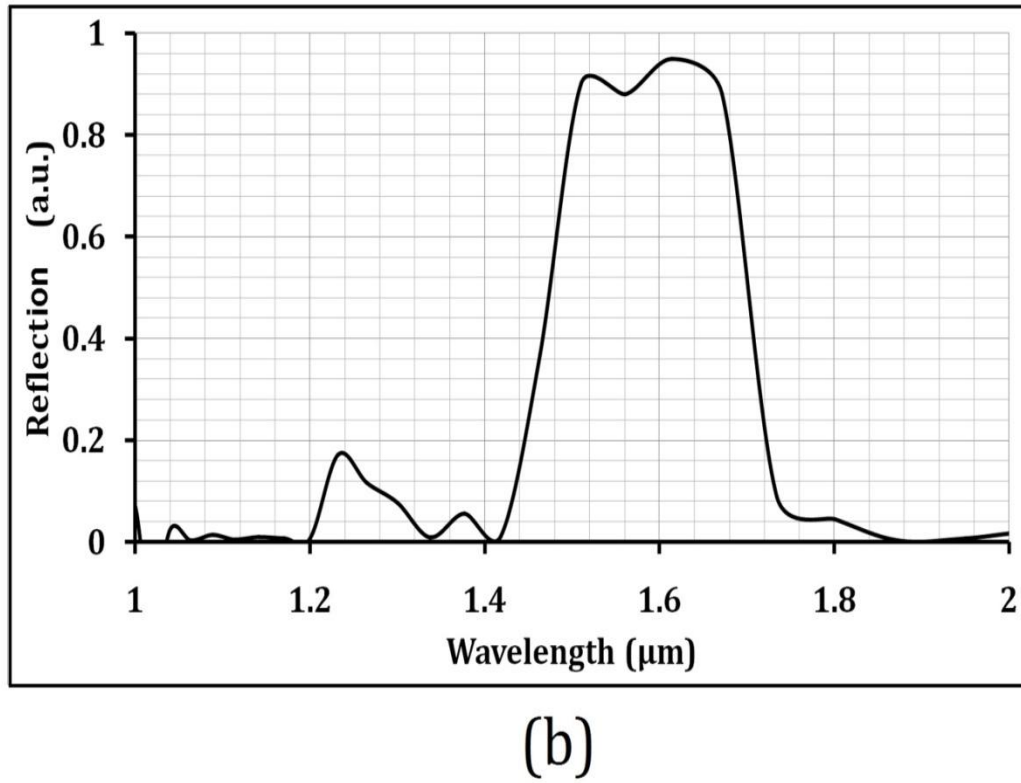
Figure 5.2: Propagation characteristics of the structure (a) Transmission (b) Reflection

It is observed that proposed structure with above mentioned dimension produced very much significant resonance response at wavelength range around 1.4 µm to 1.6 µm which is belongs to optical communication frequency range.

5.4 Determination and analysis of the Electromagnetic Parameters

To exploit the amazing electromagnetic properties of the proposed structure, all the key electromagnetic parameters i.e. such as permittivity (ε), permeability (μ), refractive index (n) etc have been obtained from the propagation characteristic curve obtained for the structure [94-102].

In the presence several method, the Yosuke et al. [102] calculation method is used to obtain the electromagnetic parameters by using the obtained data of transmittance and refractive coefficient of the proposed structure. The Yosuke et al. calculation method has the following formulas which are used for the purpose.

$$z^2 = \frac{T^2 - (1+R)^2}{T^2 - (1-R)^2} \qquad \text{.....……………} (1)$$

$$n = \frac{c}{i\omega d} \ln\left[\frac{(1+z)R}{(1-z)R} + \frac{1}{T}\right] \qquad \text{………………} (2)$$

$$T = Te^{(i\omega d/c)} \qquad \text{………………} (3)$$

$$R = -R \qquad \text{………………} (4)$$

$$\varepsilon = \frac{n}{z} \qquad \text{………………...} (5)$$

$$\mu = nz \qquad \text{………………...} (6)$$

Where T = Transmission coefficient; R = Reflection coefficient; d = effective thickness of the gold layer, c = velocity of light in vacuum, $\omega = 2\pi/\lambda$, z = impedance, n = refractive index, ε = electric permittivity, μ = magnetic permeability.

It is observed and reported that the electromagnetic parameters (such as permittivity (ε) and permeability (μ)) as well as the refractive index for the reported structure is negative in broad optical communication window of 1.4μm to 1.6μm. Figure 5.3 shows all the electromagnetic parameters for the structure.
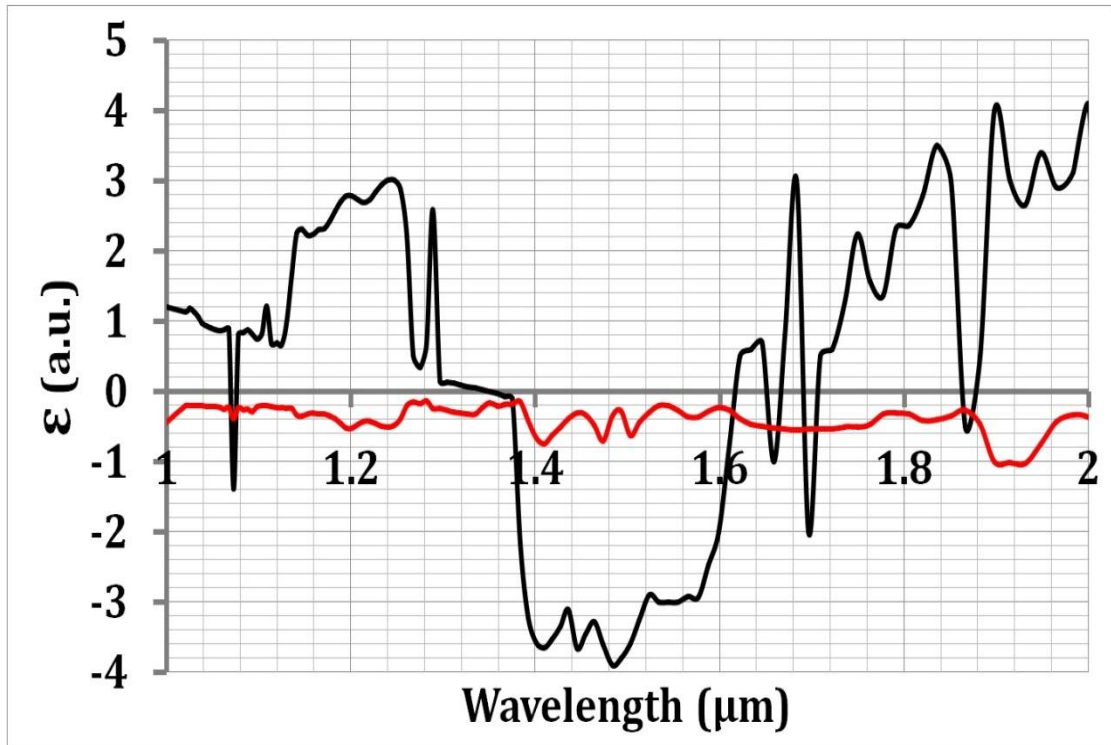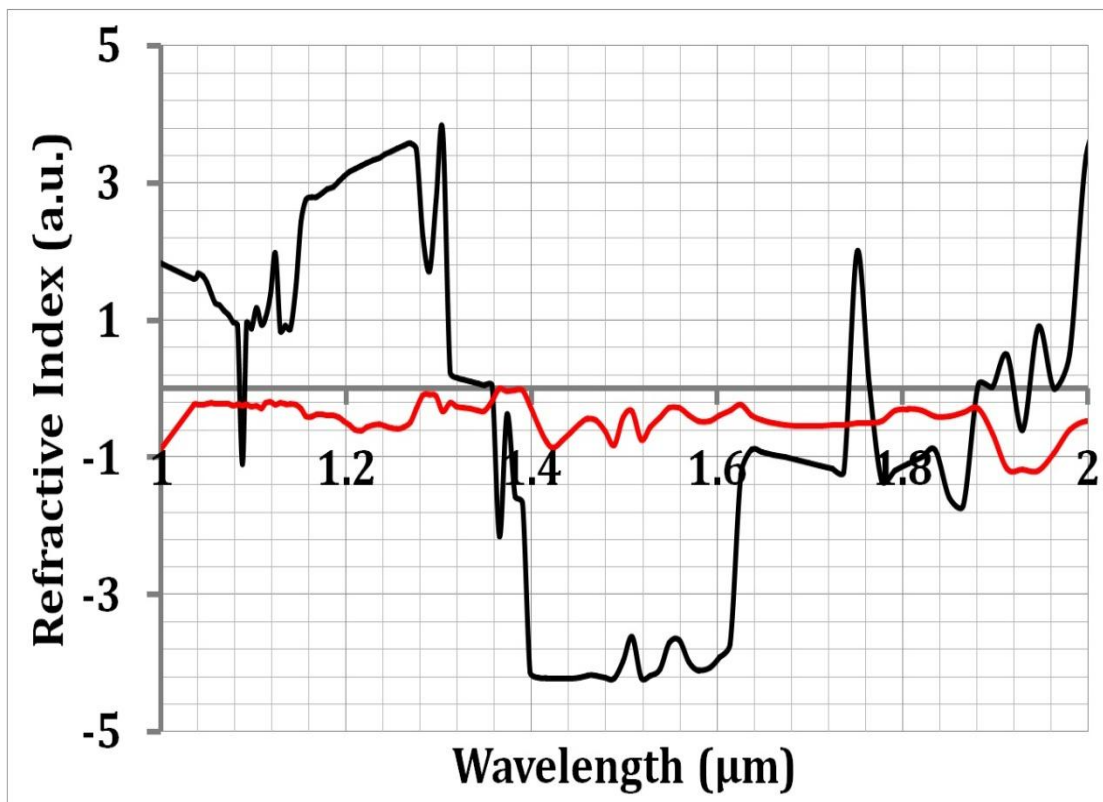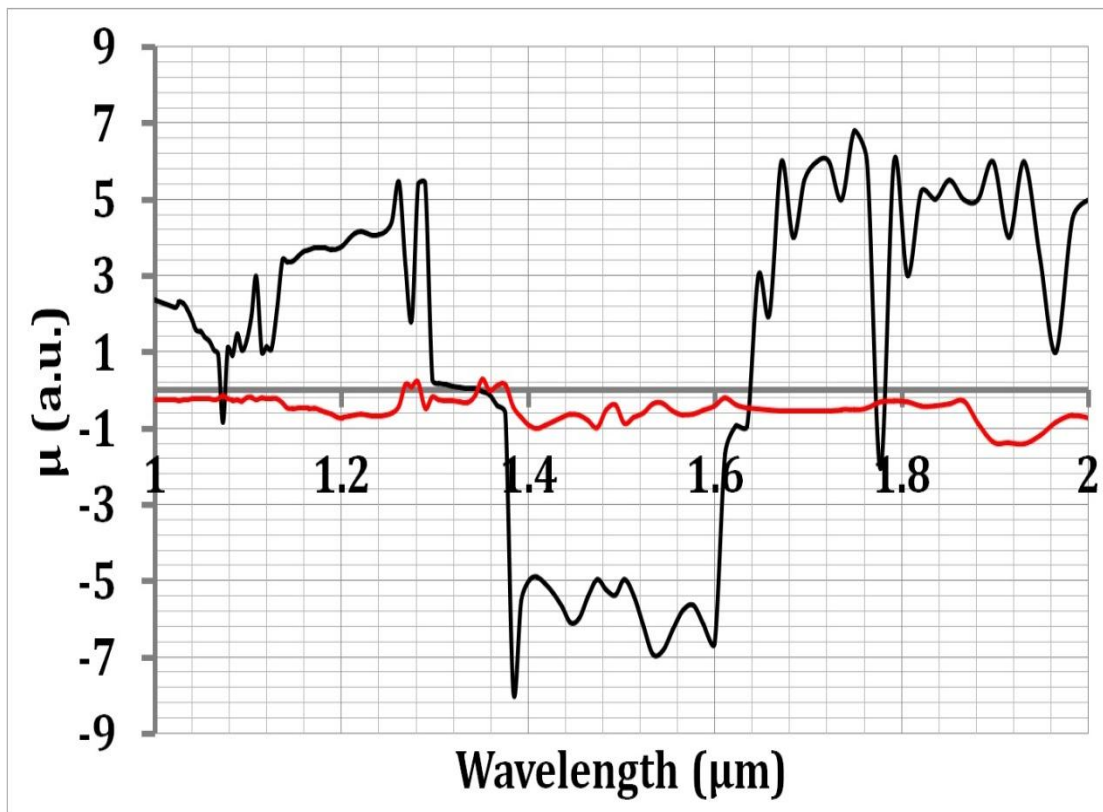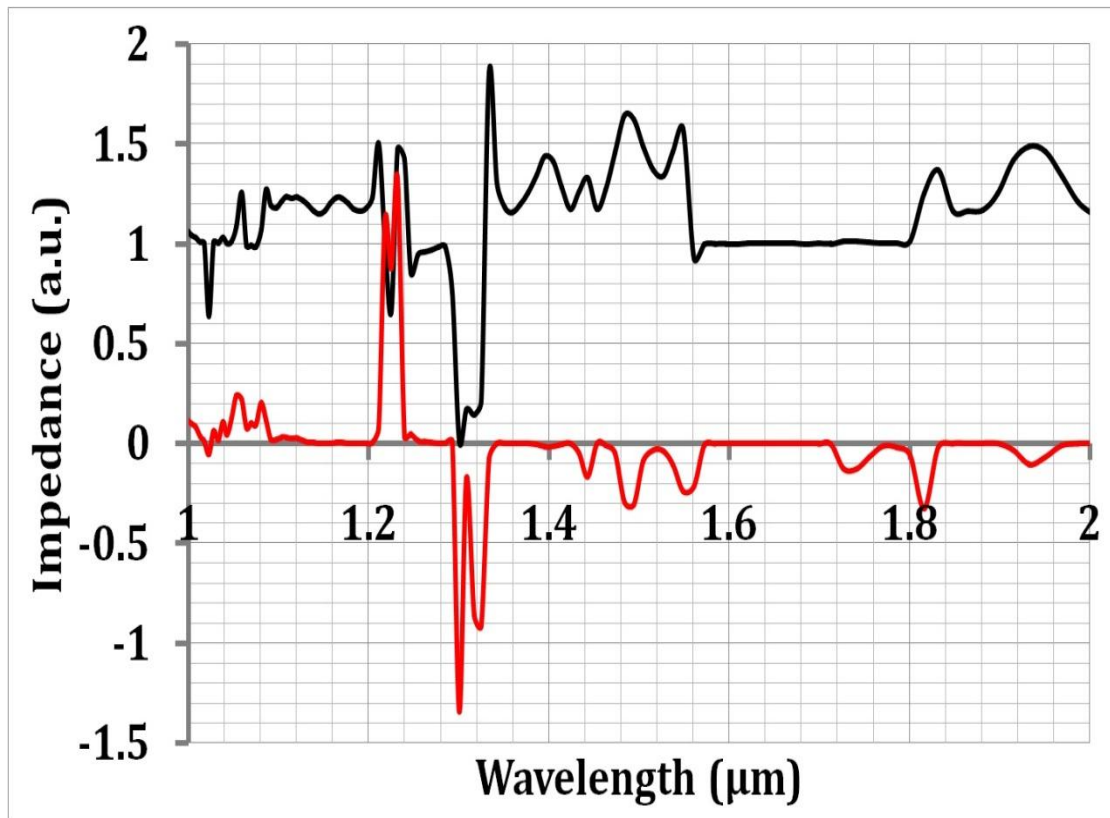
Figure5.3: Electromagnetic parameter with respect to wavelength for structure

The reported structure provides a way to build the device such as sensors, cloaking device etc. in the range of optical frequency using the property of negative refractive within very small characteristics size, this achievement open the way to advance metamaterial technology in optical frequency range.

5.5 Conclusion

The reported "I" shaped planar metamaterial structure and geometry is investigated for its electromagnetic parameters. It is observed that the transmission and reflection spectrum showing the resonance response in the wavelength range of 1.4 μm to 1.6μm. Furthermore, the calculated spectrum of the electromagnetic properties such as negative refractive index, electric permittivity and magnetic permeability is obtained negative in the wavelength range of 1.4 μm to 1.6 μm. These obtained results open

the window for the integrated application of the metamaterial in optical communication window. Thus, the reported structure put a significant mark in the design and development of metamaterials based devices in optical communication window.

References

References

[1] D. B. Keck, R. D. Maurer and P. C. Schultz, "On the ultimate lower limit of attenuation in glass optical waveguides", Applied Physics Letters, Vol. 22, pp. 307-309, (1973).

[2] F. P. Kapron, D. B. Keck and R. D. Maurer, "Radiation Losses in Glass Optical Waveguides", Applied Physics Letters, Vol. 17, pp. 423-425, (1970).

[3] M. R. Layton and J. A. Bucaro, "Optical fiber acoustic sensor utilizing mode-mode interferometer", Applied Optics, Vol. 18, pp. 666-670 (1979).

[4] K. A. Murfphy, M. S. Miller, A. M. Vengsarkar and R. O. Claus, "Elliptical-core two mode optical fiber sensor implementation methods", Journal of Lightwave Technology, Vol. 8, pp. 1688-1696 (1990).

[5] A. Ghatak and K. Thyagarajan, "Introduction to Fiber Optics", Cambridge University Press, (1998).

[6] P. Yeh, A. Yariv, and E. Marom, "Theory of Bragg fiber", J. Opt. Soc. Am., Vol. 68, pp. 1196-1201, (1978)

[7] E. Pone, C. Dubois, N. Guo, Y. Gao, A. Dupuis, F. Boismenu, S. Lacroix, and M. Skorobogatiy, "Drawing of the hollow all-polymer Bragg fibers", Opt. Exp., Vol. 14, pp. 5838-5852, (2006).

[8] K. Pande, and B. P. Pal, "Design optimization of a dual-core dispersion compensating fiber with high figure of merit and a large mode effective area for dense wavelength division multiplexed transmission through standard G.655 fibers", App. Opt., Vol. 42, pp. 3785-3791, (2003).

[9] R. J. Mears, L. Reekie, I. M. Jauncy, and D. N. Payne, "Low-noise fiber amplifier operating at 1.54 μm", Electron. Lett., Vol. 23, pp. 1026-1028, (1987).

[10] J. Broeng, G. Mogilevtsev, S. Barkou, and A. Bjarklev, "Photonic crystal fibers: a new class of optical waveguides", Optical Fiber technology, Vol. 5, pp. 305-330, July (1999)

[11] J. C. Knight, J. Broeng, T. A. Birks, and P. St. J. Russell, "Photonic bandgap guidance in optical fibers", Science, Vol. 282, pp. 1476-1478, (1998).

References

[12] A. Mekis, I.Chen, I.Kurland, S. Fan, P. R. Villeneuve, and J. D. Joannopoulos, "High transmission through sharp bends in photonic crystal waveguides", Physical Review Letters, Vol. 77, pp. 3787-3790, (1996).

[13] J. C. Knight, T. A. Birks, D. M. Atkin, and P. St. J. Russell, "Pure silica single mode fiber with hexagonal photonic crystal cladding", Optical Fiber Communication Conference, Vol. 2, p.CH 35901, (1996).

[14] T. A. Birks, P. J. Roberts, P. St. J. Russell, D. M. Atkin and T. J. Shepherd, "Full 2-D photonic band gaps in silica/air structures", Electron. Lett. Vol. 31, pp. 1941-1943, (1995).

[15] J. C. Knight, T. A. Birks, P. St. J. Russell and D. M. Atkin, "All-silica single mode optical fiber with photonic crystal cladding", Opt. Lett., Vol. 21, pp. 1547-1549, 1996, Errata, Opt. Lett., Vol. 22, pp. 484-485,(1997).

[16]   T. A. Birks, J. C. Knight and P. St. J. Russell, "Endlessly single-mode photonic crystal fiber", Opt. Lett. Vol. 22, pp. 961-963, (1997).

[17] J. C. Knight, T. A. Birks, P. St. J. Russell and J. P. de Sandro, "Properties of photonic crystal fiber and the effective index model", J. Opt. Soc. Am. A, Vol. 15, pp. 748-752, (1998).

[18]   D. Mogilevtsev, T. A. Birks, and P. St. J. Russell "Group-velocity dispersion in photonic crystal fibers", Opt. Lett., Vol. 23, pp. 1662-1664, (1998).

[19]   T. M. Monro, D. J. Richardson, N. G. R. Broderick, and P. J. Bennett "Holey optical fibers: an efficient modal model", IEEE J. of Lightwave Technolgy Vol. 17, pp. 1093-1102, (1999).

[20] A. Ferrando, E. Silvestre, J. J. Miret, J. A. Monsoriu, M. V. Andres and P. St. J. Russell, "Designing a photonic crystal fiber with flattened chromatic dispersion", Electron. Lett., Vol. 35, pp. 325-326, (1999).

[21]   R. Ghosh, A. Kumar, and J. P. Meunier "Waveguiding properties of holey fibres and effective-V model," Electron. Lett., Vol. 35, pp. 1873-1875,(1999).

[22] A. Ferrando, E. Sylvestre, J. J. Miret, and P. Andres "Nearly zero ultraflattened dispersion in photonic crystal fibers", Opt. Lett., Vol. 25, pp. 790-792, (2000).

[23] D. Ouzounov, D. Homoelle, W. Zipfel, W. W. Webb, A. L. Gaeta, J. A. West, J. C. Fajardo, and K. W. Koch "Dispersion measurements of microstructured

fibers using femtosecond laser pulses", Opt. Commun., Vol. 192, pp. 219-223, (2001).

[24]   A. Ferrando, E. Sylvestre, P. Andres, J. Miret, and M. V. Andres "Designing the properties of dispersion-flattened photonic crystal fibers," Opt. Exp., Vol. 9, pp. 687-697, (2001).

[25]   W. H. Reeves, J. C. Knight, P. St. J. Russell and P.J. Roberts, "Demonstration of ultra-flattened dispersion in photonic crystal fibers," Opt. Exp., Vol. 10, pp. 609- 613, (2002).

[26] T. A. Birks, D. Mogilevstev, J. C. Knight and P. St. J. Russell, "Dispersion compensation using single material fibers," IEEE Photon. Technol. Lett., Vol. 11, pp. 674-676, (1999).

[27] F. M. Cox, A. Argyros, and M .C. J. Large, "Liquid-filled hollow core microstructured polymer optical fiber", Opt. Exp., Vol. 14, pp. 4135-4140, (2006).

[28] J. C. Knight, T. A. Birks, R. F. Cregan, P. St. J. Russell and J. P. de Sandro, "Large mode area photonic crystal fiber," Elect. Lett. Vol. 34, pp. 1347-1348, (1998).

[29] N. A. Mortensen, "Effective area of photonic crystal fibers", Opt. Exp.,Vol. 10, pp. 341-348, (2002).

[30] N. G. R. Broderick, T. M. Monro, P. J. Bennett, and D. J. Richardson, "Nonlinearity in holey optical fibers: measurement and future opportunities", Opt. Lett., Vol. 24, pp. 1395-1397, (1999).

[31] T. A. Birks, J. C. Knight, B. J. Mangan, and P. St. J. Russell, "Photonic crystal fibers: An endless variety", IEICE Transactions On Electronics. Vol. E84-C, pp. 585-592, (2001).

[32] R. D. Birch, D. N. Payne, and M. P. Varnham, "Fabrication of polarization-maintaining fibers using gas-phase etching", Electron. Lett., Vol. 18, pp. 1036-1038, (1982).

[33]   T. Hosaka, K. Okamoto, T. Miya, Y. Sasaki, and T. Edahiro, "Low-loss single polarization fibers with asymmetrical strain birefringence", Electron. Lett., Vol. 17, pp. 530-531, (1981).

References

[34] J. Noda, K. Okamoto, and Y. Sasaki, "Polarization-Maintaining Fibers and Their Applications", J. Lightwave Technol., Vol. LT-4, pp. 1071-1088, (1986).

[35] V. G. Veselago, "The electrodynamics of substances with simultaneously negative values of permittivity and permeability," Sov.Phys. Usp. Vol. 10, pp. 509–514, (1968).

[36] J. B. Pendry, "Negative refraction makes a perfect lens," Phys. Rev. Lett. Vol. 85, pp. 3966–3969, (2000).

[37] R. A. Shelby, D. R. Smith, S. C. Nemat-Nasser, and S. Schultz, "Microwave transmission through a two dimensional, isotropic, left-handed metamaterial," Appl. Phys. Lett. Vol. 78, pp. 489–491 (2001).

[38] R. A. Shelby, D. R. Smith, and S. Schultz, "Experimental verification of a negative index of refraction," Science Vol. 292, pp. 77–79, (2001).

[39] J. B. Pendry, A. J. Holden, D. J. Robbins, and W. J. Steward, "Low frequency plasmons in thin-wire structures," J. Phys. Condens. Matter Vol. 10, pp. 4785–4809, (1998).

[40] J. B. Pendry, A. J. Holden, D. J. Robbins, and W. J. Steward, "Magnetism from conductors and enhanced nonlinear phenomena," IEEE Trans. Microwave Theory Tech. Vol. 47, pp. 2075–2084 (1999).

[41] D. R. Smith, W. J. Padilla, D. C. Vier, S. C. Nemat-Nasser, and S. Schultz, "Composite medium with simultaneously negative permeability and permittivity," Phys. Rev. Lett. Vol. 84, pp. 4184–4187, (2000).

[42] S. A. Ramakrishna, "Physics of negative refractive index materials," Rep. Prog. Phys. Vol. 68, pp. 449–521, (2005).

[43] J. Valentine, J. Li, T. Zentgraf, G. Bartal, and X. Zhang, "An optical cloak made of dielectrics," Nat. Mater. Vol. 8, pp. 568–571, (2009).

[44] J. B. Pendry, D. Schurig, and D. R. Smith, "Controlling electromagnetic fields," Science Vol. 312, pp. 1780–1782, (2006).

[45] D. Schurig, J. J. Mock, B. J. Justice, S. A. Cummer, J. B. Pendry, A. F. Starr, and D. R. Smith, "Metamaterial electromagnetic cloak at microwave frequencies," Science Vol. 314, pp. 977–980, (2006).

[46] N. Engheta and W. Z. Richard, "Metamaterials: Physics and Engineering Explorations", Wiley, (2006).

[47] S. Zouhdi, S. Ari, and P. V. Alexey, "Metamaterials and Plasmonics: Fundamentals, Modeling, Applications", Springer-Verlag, (2008).

[48] H.-T. Chen, W. J. Padilla, J. M. O. Zide, A. C. Gossard, A. J. Taylor, and R. D. Averitt, "Active terahertz metamaterial devices," Nature Vol. 444, pp. 597–600, (2006).

[49] V. G. Veselago, "Formulating Fermat's principle for light travelling in negative refraction material," Phys. Uspekhi Vol. 45, pp. 1097– 1099, (2002).

[50] I. V. Lindell, S. A. Tretyakov, K. I. Nikoskinen, and S. Ilvonen, "BW-media with negative parameter, capable of supporting backward waves," Microwave Opt. Technol. Lett. Vol. 31, pp. 129–133, (2001).

[51] R. W. Ziolkowski and E. Heynman, "Wave propagation in media having negative permeability and permittivity," Phys. Rev. E Vol. 64, pp. 056625-01-056625-15, (2001).

[52] B. Lahiri, A. Z. Khokhar, R. M. De La Rue, S. G. McMeekin, and N. P. Johnson, "Asymmetric split ring resonators for optical sensing of organic materials," Opt. Express Vol. 17, pp. 1107–1115, (2009).

[53] V. A. Fedetov, M. Rose, S. L. Prosvirnin, N. Papasimakis, and N. I. Zheludev, "Sharp trapped-mode resonances in planar metamaterials with a broken structural symmetry," Phys. Rev. Lett. Vol. 99, pp. 147401-01-147401-04, (2007).

[54] M. S. Rill, C. Plet, M. Thiel, I. Staude, G. V. Freymann, S. Linden, and M. Wegener, "Photonic metamaterials by direct laser writing and silver chemical vapour deposition," Nat. Mater. Vol. 7, pp. 543–546, (2008).

[55] K. Kishor and R. K. Sinha, "Design of planar metamaterial optical resonator," in International Conference on Fiber Optics and Photonics (Optical Society of America, 2012), paper M3B.5.

[56] R. Singh, C. Rockstuhl, C. Menzel, T. P. Meyrath, M. He, H. Giessen, F. Lederer, and W. Zhang, "Spiral-type terahertz antennas and the manifestation of the Mushiake principle," Opt. Express Vol. 17, pp. 9971–9980, (2009).

[57] K. Kishor and R. K. Sinha, "Design of planar metamaterial optical antenna," Proc. SPIE 8457, 84572N (2012).

[58] G. Dolling, M. Wegener, C. M. Soukoulis, and S. Linden, "Negative-index metamaterial at 780 nm wavelength," Opt. Lett. Vol. 32, pp. 53–55, (2007).

[59] A. K. Ghatak, R. Srivastava, I. F. Faria, K. Thyagarajan, and R. Tiwari, "Accurate method for characterizing single-mode fibers: theory and experiment", Electron Lett., Vol. 19, pp. 97–99, (1983).

[60] S. K. Varshney, and R. K. Sinha "Characterization of photonic crystal fibers from far field measurements", J Microwave Optoelectron, Vol. 2, pp. 32–42, (2002).

[61] K. N. Park, and K. S. Lee, "Improved effective-index method for analysis of photonic crystal fibers", Opt Lett Vol. 30, pp. 58–60, (2005).

[62] A. D. Varshney, and R. K. Sinha, "Propagation characteristics of photonic crystal fiber: scalar effective index method and fully vectorial effective index method", Adv Studies Theor Phys, Vol. 1, pp. 75–85, (2007).

[63] B. T. Kuhlmey, H. C. Nguyen, M. J. Steel, and B. J. Eggleton, "Confinement loss in adiabatic photonic crystal fiber tapers", J. Opt. Soc. Am. B, Vol. 23, pp. 1965–1974, (2006).

[64] Y. Li, Y. Yao, M. Hu, L. Chai, and C. Wang, "Improved fully vectorial effective index method for photonic crystal fibers: evaluation and enhancement". Appl Opt, Vol. 47, pp. 399–406, (2008).

[65] T. Itoh, G. Pelosi, and P. Silvester, "Finite Element Software for Microwave Engineering", Wiley-Interscience, New York , (1996).

[66] F. Brechet, J. Marcou, D. Pagnoux, and P. Roy, "Complete Analysis of the Characteristics of Propagation into Photonic Crystal Fibers, by the Finite Element Method", Optical Fiber Technology, Vol. 6, pp. 181-191, (2000).

[67] K. Saitoh and M. Koshiba, "Full-vectorial imaginary-distance beam propagation method based on a finite element scheme: application to photonic crystal fibers," IEEE J. Quantum Electron, Vol. 38, pp. 927–933 (2002).

[68] M. Koshiba and K. Saitoh, "Structural dependence of effective area and mode field diameter for holey fibers," Opt. Express, Vol. 11, pp. 1746–1756, (2003).

[69] M. Qiu, "Analysis of guided modes in photonic crystal fibers using the finite difference time-domain method" Microwave and Optical Technology Letters, Vol. 30, pp. 327-330, (2001).

[70] G. E. Town, and J. T. Lizier, "Tapered holey fibers for spot size and numerical aperture conversion", Proc. CLEO'2001, Paper CtuAA3, P. 261.

[71] C. T. Chan, Q. L. Yu, and K. M. Ho, "Order-N spectral method for electromagnetic waves", Physical Review B, Vol. 51, pp. 16635-16642, (1995).

[72] M. Qiu and S. He, "A nonorthogonal finite-difference time-domain method for computing the band structure of a two-dimensional photonic crystal with dielectric and metallic inclusions", J. Appl. Phys. Vol. 87 , pp. 8268-8275, (2000)

[73] M. Qiu and S. He, "FDTD algorithm for computing the off-plane band structure in a two-dimensional photonic crystal with dielectric or metallic inclusions", Physics Letters A, Vol. 278, pp. 348-354, (2001).

[74] M. Qiu, and S. He, "Numerical method for computing defect modes in two dimensional photonic crystals with dielectric or metallic inclusions", Phys. Rev. B Vol. 61, pp. 12871-12876, (2000).

[75] M. Qiu, and S. He, "Guided modes in a two-dimensional metallic photonic crystal waveguide",Phys. Lett. A, Vol. 266, pp. 425-429 (2000).

[76] M. Szustakowski, N. Palka, and W. Grabiec, "Simple method for characterization of photonic crystal fiber", J Telecom & Info Technol, Vol. 2 pp. 109–113, (2007).

[77] G. P. Agarwal, "Nonlinear Fiber Optics", third ed., (1995).

[78] T. Masatoshi and F. Moriyuki, "Optical properties of a low-loss polarization-maintaining photonic crystal fiber", Optics Express, Vol. 9, pp. 676- 680, (2001).

[79] P. R. Chaudhuri, V. Paulose, C. Zhao, and C. Lu, "Near-Elliptic Core Polarization Maintaining Photonic Crystal Fiber: Modeling Birefringence Characteristics and Realization," IEEE Photonics Tech. Lett., Vol. 16, pp. 1301-1303, (2004).

References

[80] A. D. Varshney and R.K. Sinha, "Study of Birefringence of Elliptical Core Photonic Crystal Fiber using Mathieu function", Applied Optics, Vol. 46, pp. 5912-5916 (2007).

[81] A. D. Varshney and R.K. Sinha, "Ultrahigh Birefringent Photonic Crystal Fiber: An Improved Design," Int. J. Microwave and Optical Tech., Vol. 4, pp. 324-327, (2009).

[82] R. K. Sinha, "Accurate Estimation of Aspect ratio of Elliptical Core Optical Fibers from Far Field Measurements: Theory and Experiment", LEOS 1997, 10th Annual Meeting Conference Proceedings, IEEE, Vol. 2, pp. 50-51, (1997).

[83] A. Kumar and R. K. Varshney, "Propagation characteristics of highly elliptical core optical waveguide: A perturbation approach", Optical and Quantum Electron., Vol. 16, pp. 349–354, (1984).

[84] A. C. Boucouvalas, "Use of Far-Field Radiation Pattern to Characterize Single-mode Symmetric Slab Waveguide", IEEE, Elec. Lett., Vol. 19, pp. 120-121, (1983).

[85] Y. Matt, "Mode-Field Diameter of Single-Mode Optical Fiber by Far-Field Scanning," Applied Optics. Vol. 37, pp. 5605-5619, (1998).

[86] J. Zhou, T. Koschny, M. Kafesaki, E. N. Economu, J. B. Pendry, and C. M. Soukoulis, "Saturation of the magnetic response of split-ring resonators at optical frequencies," Phys. Rev. Lett. Vol. 95, pp. 223902-1-223902-4, (2005).

[87] M. W. Klein, C. Enkrich, M. Wegener, C. M. Soukoulis, and S. Linden, "Single-slit split-ring resonators at optical frequencies:limits of size scaling," Opt. Lett. Vol. 31, pp. 1259–1261, (2006).

[88] S. Tretyakov, "On geometrical scaling of split ring and doublebar resonators at optical frequencies," Metamaterials, Vol. 1, pp. 40–43, (2007).

[89] B. Lahiri, S. G. McMeekin, A. Z. Khokhar, R. M. De La Rue, and N. P. Johnson, "Impact of titanium adhesion layers on the response of arrays of metallic split-ring resonators (SRRs)," Opt. Express Vol. 18, pp. 3210–3218, (2010).

[90] W. C. Chen, J. J. Mock, D. R. Smith, T. Akalin, and W. J. Padilla, "Controlling gigahertz and terahertz surface electromagnetic waves with

metamaterial resonators," Phys. Rev. X Vol.1, pp. 021016-1-021016-4, (2011).

[91] S. Linden, C. Enkrich, M. Wegener, J. Zhou, T. Koschny, and C. M. Soukoulis, "Magnetic response of metamaterials at 100 terahertz," Science Vol. 306, pp. 1351–1353, (2004).

[92] C. Rockstuhl, F. Lederer, C. Etrich, T. Zentgraf, J. Kuhl, and H. Giessen, "On the reinterpretation of resonances in split ring resonators at normal incidence," Opt. Express Vol. 14, pp. 8827–8836, (2006).

[93] B. Lahiri, G. Holland, V. Aksyuk, and A. Centrone, "Nanoscale imaging of plasmonic hot spots and dark modes with the photothermal-induced resonance technique," Nanoletters Vol. 13, pp. 3218–3224, (2013).

[94] A. M. Nicolson and G. F. Ross, "Measurement of the intrinsic properties of material by time-domain techniques," IEEE Trans. Instrum. Meas. Vol. 19, pp. 377–382, (1970).

[95] D. R. Smith, S. Schultz, P. Markos, and C. M. Soukoulis, "Determination of effective permittivity and permeability of metamaterials from reflection and transmission coefficients," Phys. Rev.B Vol. 65, pp. 195104-1-195104-5, (2002).

[96] M. Iwanaga, "Effective optical constants in stratified metaldielectric metamaterial," Opt. Lett. Vol. 32, pp. 1314–1316, (2007).

[97] P. Markos and C. M. Soukoulis, "Transmission properties and effective electromagnetic parameters of double negative metamaterials," Opt. Express Vol. 11, pp. 649–661, (2003).

[98] E. Saenzz, P. M. T. Ikonen, R. Gonzalo, and S. A. Tretyakov, "On the definition of effective permittivity and permeability for thin composite layers," J. Appl. Phys. Vol. 101, pp. 114910-1-114910-7, (2007).

[99] T. Koschny, P. Markos, D. R. Smith, and C. M. Soukoulis, "Resonant and antiresonant frequency dependence of the effective parameters of metamaterials," Phys. Rev. E Vol. 68, pp. 065602-1-065602-4, (2003).

[100] R. A. Depine and A. Lakhtakia, "Comment I on resonant and antiresonant frequency dependence of the effective parameters of metamaterials," Phys. Rev. E Vol. 70, pp. 048601-1, (2004).

[101] A. L. Efros, "Comment II on resonant and antiresonant frequency dependence of the effective parameters of metamaterials," Phys. Rev. E Vol. 70, pp. 048602-1-048602-2, (2004).

[102] Y. Minowa, T. Fujii, M. Nagai, T. O. K. Sakoda, K. Hirao, and K. Tanaka, "Evaluation of effective electric permittivity and magnetic permeability in metamaterial slabs by terahertz time-domain spectroscopy," Opt. Express Vol. 16, pp. 4785–4796, (2008).

[103] Marques R., Martel J., Mesa F., and Medina F., Left-handed-media simulation and transmission of EM waves in subwavelength split-ring-resonator loaded metallic waveguides, Phys.Rev. Lett. Vol. 89, pp. 183901-1-183901-4, (2002).

[104] R. W. Ziolkowski, "Design, fabrication, and testing of double negative metamaterials," IEEE Transactions on Antennas and Propagation, Vol. 51, 1516-1529, (2003).

[105] E. Ekmekci, and G. Turhan-Sayan, "Comparative investigation of resonance characteristics and electrical size of the double-sided SRR, BC-SRR and conventional SRR type metamaterial for varying substrate parameters", Progress In Electromagnetics Research B, Vol. 12, pp. 35-62, (2009).

STUDENT APPROVAL FORM

Name of the Author	Kamal Kishor
Department	Department of Applied Sciences and Humanities
Degree	Doctor of Philosophy
University	University of Delhi
Guide	Prof. R.K. Sinha
Thesis Title	Characterization of Photonic Crystal Fibers and Metamaterials: Theory and Experiments
Year of Award	

Agreement

1. I herby certify that, if appropriate, I have obtained and attached hereto a written permission/statement from the owner(s) of each third party copyrighted matter to be included in my thesis/dissertation, allowing distribution as specified below.

2. I hereby grant to the university and its agents the non-exclusive license to archive and make accessible, under the condition specified below, my thesis/dissertation, in the whole or in part in all forms of media, now or hereafter know. I retain all other ownership rights to the copyright of the thesis/dissertation. I also retain to use in future works (such as article or books) all or part of this thesis, dissertation, or project report.

Conditions:

1. Release the entire work for access worldwide	

2. Release the entire work for 'My University only for
 	
      1 Year
      2 Year
      3 Year
And after this time release the work for access worldwide	

3. Release the entire work for 'My University only while at the same time releasing the following parts of the work (e.g. because other parts relate to publications) for the worldwide access.
 	
   a) Bibliographic details and synopsis only.
   b) Bibliography details, synopsis and the following chapters only.
   c) Preview/Table of Contents/24 page only.	

4. View only (NO Downloads) (worldwide)	

Signature of the Scholar   Signature and Seal of the Guide

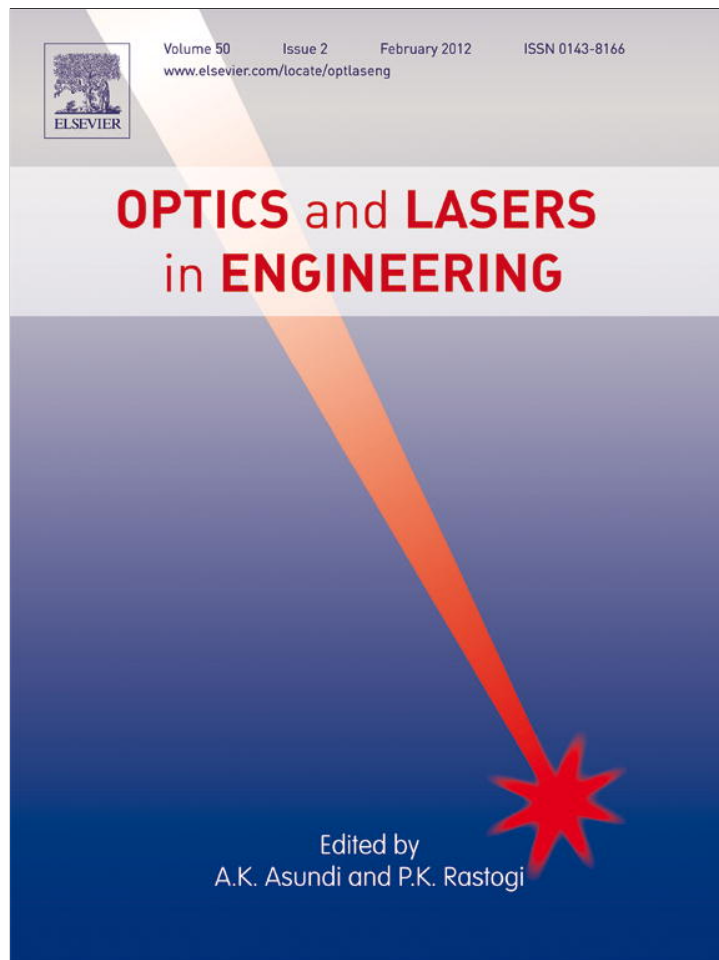**Kamal Kishor**   **Prof. R.K. Sinha**

Place: Delhi
Date:

Reprints of Research Papers

Experimental verification of improved effective index method for endlessly single mode photonic crystal fiber

Kamal Kishor, R.K. Sinha*, Anshu D. Varshney

TIFAC-Centre of Relevance & Excellence in Fiber Optics and Optical Communications, Applied Physics Department, Delhi Technological University, (Formerly Delhi College of Engineering), Bawana Road, Delhi–110 042, India

ABSTRACT

We report the experimental verification of Improved Effective Index Method (IEIM) for Endlessly Single Mode Photonic Crystal Fibers (ESM PCFs) from far field intensity measurements. In this paper all the key parameters i.e. *V*-Number, effective refractive index of the cladding, radius of the core and numerical aperture have been obtained from the experimentally measured far-field intensity pattern of ESM-PCFs. It is shown that the transmission characteristics of ESM-PCFs match with the simulation result obtained using IEIM and also with the core diameter of PCF obtained from scanning electron microscope (SEM) within the experimental limit.

© 2011 Elsevier Ltd. All rights reserved.

1. Introduction

Photonic crystal materials are the prime focus area in the past few years with the number of publications and patents increasing exponentially. It is now the critical phase of their development as they move fast from the realm of fundamental studies to the manufacturing of photonic devices and commercial deployment of photonic crystal fibers in optical communication network.

Photonic crystals are patterned materials with a well defined periodicity in dielectric constant. Photonic Crystal Fibers (PCFs) are one of the most important applications of photonic crystal materials. PCFs have given a new dimension in the field of optical communication. PCF has the ability to confine light with the confinement characteristics, not possible in conventional optical fiber due to its high degree of design flexibility [1–5]. PCF is an optical fibers made up of single material with an arrangement of periodic air holes across the cross-section running down its entire length. A localized region of higher refractive index is formed by leaving a single lattice site without an air hole. Light can be trapped along the axis of the fiber in this localized region, which acts as a waveguide core. PCFs are now finding applications in fiber-optic communications, fiber lasers, nonlinear devices, high-power transmission, highly sensitive gas sensors, super-continuum generation and other areas. With its high degree of design flexibility and wavelength dependent refractive index of cladding, PCFs can be optimized for single mode operation over a very long range of wavelengths. Due to this property it is also named as Endlessly Single Mode PCF (ESM PCF), first coined by Birks et al. [1]. Extensive numerical calculation for the transmission characteristics of ESM PCF have been reported in the recent past [6–11]. Many numerical modeling techniques have been applied to study its propagation and transmission characteristics, which include the effective index method (EIM) [9,11–13], scalar effective index method (SEIM) [13], full vectorial effective index method (FVEIM) [13], plane wave expansion method [14–16], localized basis function method [12,17,18], finite element method [19,20], finite difference time domain method [21,22] and multipole method [23–25], etc.

The basic of all these methods is to calculate the effective cladding index and then compute the propagation characteristics of the PCFs. Among the above mentioned methods, the FVEIM requires less computation time and less computer memory. However FVEIM does not provide very accurate results at higher wavelength values. This has led to development of Improved Effective Index method (IEIM) by Park and Lee (2005) [8] in which they empirically expressed the optimized value of core radius of PCF in terms of air hole spacing (Λ) and air hole diameter (d). The implementation of the core radius in terms of air hole diameter and air hole spacing substantially improved the accuracy of the results of effective index method. Although IEIM has been extensively used to estimate propagation characteristics of PCFs, yet no effort has been done to experimentally test this method.

---

* Corresponding author. Tel.: +91 11 27871017; fax: +91 11 27871023.
E-mail address: dr_rk_sinha@yahoo.com (R.K. Sinha).

Mortensen and Folkenberg have investigated the transition of the fundamental mode radiating out of a PCF, from near field to the far field [28] for endlessly single mode PCF. Further, implication of six fold rotational symmetry in the far field intensity pattern measurement of PCF is also analyzed by Dabirian et al. [29]. However, the geometrical and waveguiding parameters of PCFs had not been explicitly obtained using far field measurements for experimental characterization of ESM PCFs.

In this paper, we report the experimental verification of IEIM for ESM PCF from far field intensity measurements. From the experimental measurements of the far field intensity pattern, we obtained the transmission characteristics of ESM PCF in terms of V-number, effective refractive index of the cladding, radius of the core, numerical aperture, etc. The experimental values of the waveguiding and geometrical parameters are found to be in agreement with the simulation results obtained using IEIM and Scanning Electron Microscope (SEM) data. This paper is supported with experimental as well as simulation results and confirms the validity of IEIM for estimation of transmission characteristics of ESM PCFs.

2. Theory

In this paper, the geometrical and wave guiding parameters of ESM PCF are obtained from the far field intensity measurements. It is also referred as the Fraunhofer region intensity measurement; the region where the angular field distribution is essentially independent of distance from the source.

Far field intensity expression of the cylindrical waveguide is obtained. The far-field radiation pattern $\Psi(r, \theta, \Phi)$ is the inverse Fourier transform of the aperture or near fields.

The normalized (wrt $\theta=0$) far-field intensity distribution $I(\theta)$ for the fundamental mode of PCF [6,27] with normalized radiation angle (α) is given as

$$I(\theta) = |\Psi|^2 \tag{1a}$$

$$|\Psi|^2 = \left[\frac{U^2 W^2}{(U^2-\alpha^2)(W^2+\alpha^2)}\left\{J_0(\alpha)-\alpha J_1(\alpha)\frac{J_0(U)}{UJ_1(U)}\right\}\right]^2 \quad \text{for } U \neq \alpha \tag{1b}$$

$$|\Psi|^2 = \left[\frac{U^2 W^2}{(2V^2)(UJ_1(U))}\left\{J_0^2(\alpha)+J_1^2(\alpha)\right\}\right]^2 \quad \text{for } U \neq \alpha \tag{1c}$$

where $V^2 = U^2 + W^2$; $\alpha = ka \sin\theta$; $k = 2\pi/\lambda_0$; λ_0 is the free-space wavelength and 'a' is the optimized radius of the core. With the help of above equations the universal curve (Fig. 1) for the step index photonic crystal fiber is plotted, which is used for the characterization of ESM PCF from the far-field measurement.

It is noted that α_{10} and α_{50} are the values of $\alpha(=ka \sin\theta)$, which correspond to angles in the far field intensity pattern at which the intensity has dropped to 10% and 50% of its maximum value (at $\theta=0$). The intensities are measured at θ_{10} because it is practically very difficult to measure the first minimum intensity position accurately in far field intensity pattern [26,27].

2.1. Improved effective index method

The development of IEIM was led by Park and Lee [8] and later used by subsequent authors [30–32]. In IEIM the core radius (r_c) is optimized in terms of pitch (Λ) and air hole diameter (d), which substantially improved the accuracy of the results of the effective index method [9–11]. As the core radius of a PCF with a fixed pitch should decrease when air hole diameter becomes large, whereas the core radius of a PCF with a fixed air hole size increases when the pitch increases. Therefore the core radius has been optimized using empirical formula given as

$$\frac{r_c}{\Lambda} = c_1 / \left\{1 + \exp\left[\left(\frac{d}{\Lambda} - c_3\right)/c_2\right]\right\} \tag{2}$$

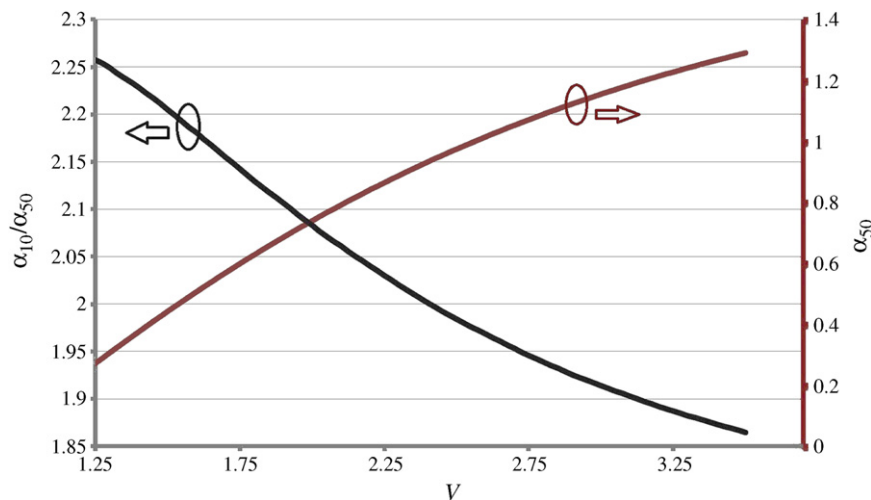where $c_1 = 0.686064$, $c_2 = 0.265366$ and $c_3 = 1.291080$

The tolerance of this formula is $1e-6$.

The analysis of fully vectorial effective index method begins with Maxwell's equations. The homogeneous vector wave equations for the electrical field 'E' and magnetic field 'H' in cylindrical coordinates, since the refractive index profile of the PCFs are cylindrically symmetric can be rewritten as,

$$\frac{\partial^2 \psi}{\partial r^2} + \frac{1}{r}\frac{\partial \psi}{\partial r} + \frac{1}{r^2}\frac{\partial \psi}{\partial \phi} + (k^2 n^2 - \beta^2)\psi = 0 \tag{3}$$

where n is the refractive index of the material, β is the propagation constant, k is the wave vector and ψ can represent either the E_z or H_z. By applying boundary conditions, dispersion equation has been obtained

$$\left(\frac{P_l'(\gamma a)}{\gamma a P_l(\gamma a)} + \frac{I_l'(\kappa a)}{\kappa a P_l(\kappa a)}\right)\left(\frac{n_{silica}^2 P_l'(\gamma a)}{\gamma a P_l(\gamma a)} + \frac{n_{air}^2 I_l'(\kappa a)}{\kappa a P_l(\kappa a)}\right)$$
$$= l^2\left[\left(\frac{1}{\gamma a}\right)^2 + \left(\frac{1}{\kappa a}\right)^2\right]^2\left(\frac{\beta}{k}\right)^2 \tag{4}$$

Fig. 1. Variation of the ratio α_{10}/α_{50} (black) and α_{50} (red) with V parameter. (For interpretation of the references to color in this figure legend, the reader is referred to the web version of this article.)

where $P_l(\gamma(\omega)\rho) = J_l(\gamma(\omega)\rho)Y_l(\gamma(\omega)R) - Y_l(\gamma(\omega)\rho)J_l(\gamma(\omega)R)$ and parameters $\kappa(\omega)$ and $\gamma(\omega)$ are defined as $\kappa^2(\omega) = \beta^2(\omega) - n_{air}^2\omega^2/c^2$ and $\gamma^2(\omega) = n_{silica}^2(\omega)\omega^2/c^2 - \beta^2(\omega)$ with c being the velocity of light in vacuum.

Setting $l = 1$ in the above equation, one can solve for $n_{eff}(\omega)$ of the fundamental space filling mode. The index of pure silica ($n_{Si} = 1.457$ at 633 nm) [34] and the index of fundamental space filling mode are used as the indices of the core and cladding, respectively, in effective index method.
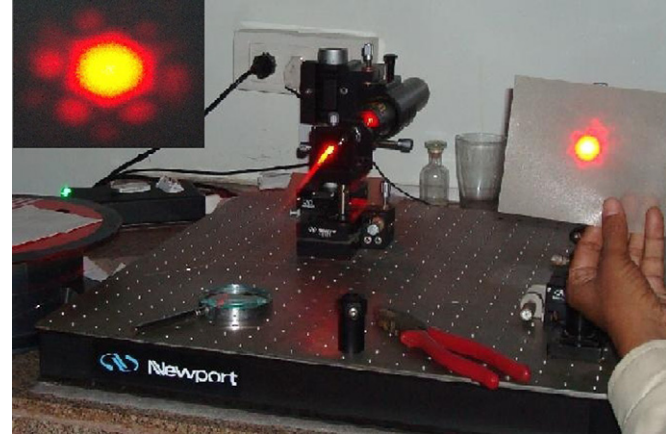

Fig. 2. Real time experimental arrangement; Far-Field pattern (inset).
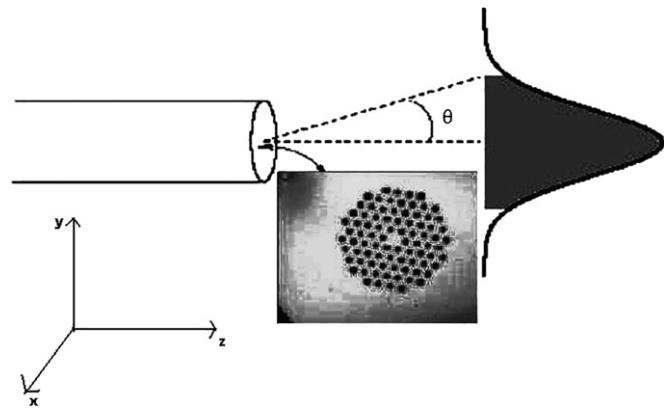

Fig. 3. Experimental arrangement for far field measurement.

The characteristic equation obtained from the FVEIM [30] is written as

$$\left(\frac{J'_1(U_{eff})}{U_{eff}J_1(U_{eff})} + \frac{K'_1(W_{eff})}{W_{eff}K_1(W_{eff})}\right)\left(n_{cl}^2\frac{J'_1(U_{eff})}{U_{eff}J_1(U_{eff})} + n_{eff}^2\frac{K'_1(W_{eff})}{W_{eff}K_1(W_{eff})}\right)$$
$$= \left(\frac{1}{U_{eff}^2} + \frac{1}{W_{eff}^2}\right)^2\left(\frac{\beta}{k}\right)^2 \tag{5}$$

where $U_{eff} = k_0\rho\sqrt{n_s^2 - n_{eff}^2}$ $W_{eff} = k_0\rho\sqrt{n_{eff}^2 - n_{FSM}^2}$ n_{eff} is the effective index of the fundamental mode and hence n_{cl} is the effective cladding index obtained from equation (4).

3. Experimental setup and characterization method

3.1. Experimental setup

This experimental setup (Fig. 2) consists of a laser with wavelength 633 nm, microscopic lens, fiber chuck and holders, Polarizer sheet (to find the polarization axes of laser), Silicon-photodetector (818-SL/Newport) with digital display and 10 m long three samples of ESM-PCFs (ESM-12-01, LMA-10 and LMA-15) obtained from Crystal Fiber, Denmark. Fiber output end is mounted on a calibrated circular mount fitted with a photodetector such that the fiber end is at the center of the circle and when we rotate the circular mount photodetector records the far field at the circumference of the circle. The sketch of experimental setup to record the far field intensity pattern of ESM PCF [33] is shown in Fig. 3.

3.2. Characterization methods

The ends of ESM PCFs are stripped and cleaved properly to minimize the reflection losses. The far-field radiation patterns of fundamental mode (Fig. 4) for the ESM PCFs are recorded at output end of the fibers. From Fig. 4, we obtain the corresponding angles θ_{10} and θ_{50} at which the intensity drops to 10% and 50% of its maximum value (at $\theta = 0$) for three fibers. Thereby ratio $\sin\theta_{10}/\sin\theta_{50}$ is obtained using Fig. 4. From the universal graph (Fig. 1), the V value is obtained corresponding to experimental values of $\sin\theta_{10}/\sin\theta_{50}$ for each fiber. For the respective V parameter the corresponding $\alpha_{50}(= k_0a\sin\theta_{50})$ is calculated from the right hand ordinate of the universal graph (Fig. 1). Since θ_{50} was already known, the core radius is calculated with the value of α_{50}, at the known operating wavelength (633 nm). Since V parameter and core dimension is obtained, the corresponding numerical aperture ($\sqrt{n_1^2 - n_2^2}$) is calculated for each ESM PCF.
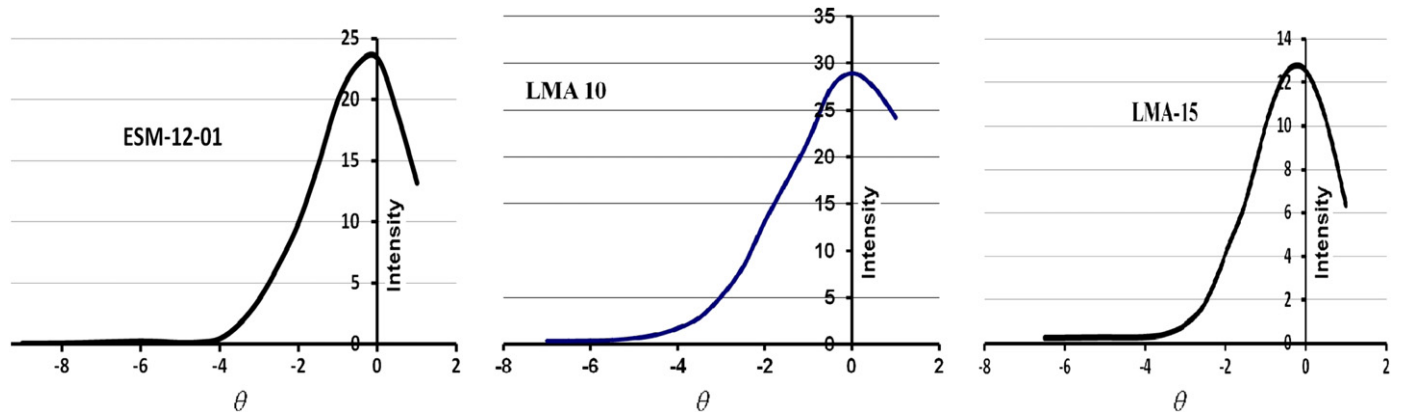

Fig. 4. Measured far field intensity distribution of ESM PCFs.

Table 1
Geometrical and waveguiding parameters of PCFs obtained from IEIM, SEM and experimental results obtained from far field measurements.

		IEIM(a)/Measured from SEM (b)	Experimental results
V-parameter	ESM-12-01	2.8268 (a)	2.725 ± 0.06
	LMA-10	2.9540 (a)	2.701 ± 0.05
	LMA-15	2.9703 (a)	2.775 ± 0.05
Core diameter (micrometer)	ESM-12-01	7.18 (b)	7.01 ± 0.05
	LMA-10	8.95 (b)	8.62 ± 0.04
	LMA-15	13.84 (b)	13.59 ± 0.04
Numerical aperture	ESM-12-01	0.055972 (a)	0.038829 ± 0.0011
	LMA-10	0.074013 (a)	0.063246 ± 0.0014
	LMA-15	0.048275 (a)	0.041360 ± 0.0008
Effective refractive index of cladding($n_{clad.}$)	ESM-12-01	1.4560 (a)	1.45648 ± 0.041
	LMA-10	1.4552 (a)	1.45562 ± 0.032
	LMA-15	1.4562 (a)	1.45641 ± 0.028

Further, using refractive-index of core (n_1)=1.457 at 633 nm obtained with Sellemier formula [34], the effective refractive index of cladding $n_2(=n_{clad})$ is calculated using the value of numerical aperture.

4. Results and discussion

The core radius is obtained by universal graph (Fig. 1) and these values are verified with the SEM measurement and are found to be in agreement with each other for the three different sample of ESM PCF.

The V-parameters for each fiber is obtained from the universal graph (Fig. 1), using the experimental value of corresponding $\sin \theta_{10}/\sin \theta_{50}$ and is verified with the values calculated from IEIM.

The numerical aperture $\sqrt{n_1^2 - n_2^2}$ is calculated using the above obtained values of V-parameters for respective fibers and corresponding core radius and are verified with the calculations by IEIM.

The effective refractive index of cladding for each ESM PCF is calculated using respective value of core refractive index (n_1)=1.457 and the numerical aperture and are verified with the results obtained from IEIM.

The experimental results obtained for the transmission characteristics of ESM PCFs are found to match with the results obtained using improved effective index method (IEIM) and scanning electron microscope (SEM) data. It was found that the experimental values validate the numerical method as the results are in good match and have been compared and tabulated in Table 1 along with corresponding maximum possible error. It is mentioned that an error in measurement of angles θ_{10} and θ_{50} leads to error in calculation of V-parameters, core diameter, numerical aperture and effective refractive index of cladding.

5. Conclusion

Far field method is applied to obtain the transmission characteristics of ESM PCFs and to validate the results calculated using IEIM. It is shown that the transmission characteristics i.e. core diameter, V-parameter, effective refractive index of cladding and numerical aperture are obtained from far field measurement match with the SEM data and simulation results using IEIM within the experimental limits. Thus the far field measurement method and IEIM validate and authenticate the results obtained from each other.
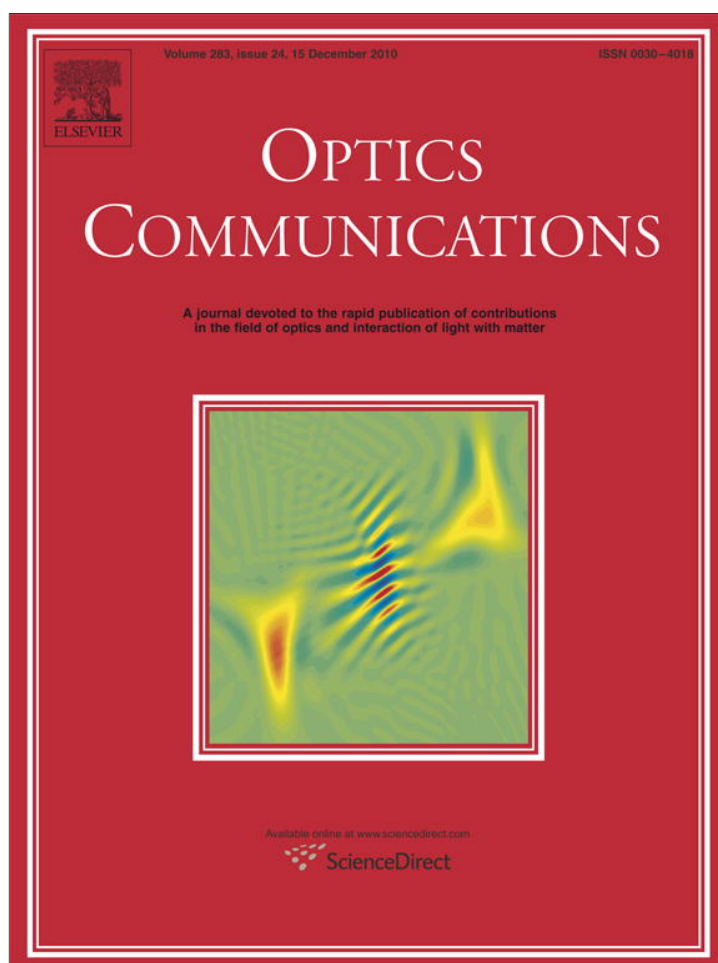
References

[1] Knight JC, Birks TA, Russell PStJ, Atkin DM. All-silica single-mode optical fiber with photonic crystal cladding. Opt Lett 1996;21:1547–9.
[2] Birks TA, Knight JC, Russel PStJ. Endlessly single-mode photonic crystal fiber. Opt Lett 1997;22:961–3.
[3] Broeng J, Mogilevstev D, Barkou SE, Bjarklev A. Photonic crystal fibers: a new class of optical waveguides. Opt Fiber Technol 1999;5:305–30.
[4] Birks TA, Knight JC, Mangan BJ, Russell PStJ. Photonic crystal fibers: an endless variety. IEICE Trans Electron 2001;E84-C:585–92.
[5] Kishor K, Sinha RK, Varshney AD, Singh J. Characterization of specially designed polarization maintain photonic crystal fiber from far field radiation patterns. Opt Commun 2010;283:5007–11.
[6] Varshney SK, Sinha RK. Characterization of photonic crystal fibers from far field measurements. J Microwave Optoelectron 2002;2:32–42.
[7] Szustakowski M, Palka N, Grabiec W. Simple method for characterization of photonic crystal fiber. J Telecom & Info Technol 2007;2:109–13.
[8] Park KN, Lee KS. Improved effective-index method for analysis of photonic crystal fibers. Opt Lett 2005;30:958–60.
[9] Knight JC, Birks TA, Russell PStJ, de Sandro JP. Properties of photonic crystal fiber and the effective index model. J Opt Soc Am A 1998;15:748–52.
[10] Sinha RK, Varshney SK. Dispersion Properties of Photonic crystal Fibers. Microwave Opt Technol. Lett 2003;37:129–32.
[11] Varshney SK, Singh MP, Sinha RK. Propagation characteristics of photonic crystal fibers. J Opt Commun 2003;24:192–8.
[12] Peyrilloux A, Février S, Marcou J, Berthelot L, Pagnoux D, Sansonetti P. Comparison between the finite element method, the localized function method and a novel equivalent averaged index method for modeling photonic crystal fibres. J Opt A: Pure Appl Opt 2002;4:257–62.
[13] Sinha RK, Varshney AD. Dispersion properties of photonic crystal fiber: comparison by scalar and fully vectorial effective index methods. Opt Quantum Electron 2005;37:711–22.
[14] Barkou SE, Broeng J, Bjarklev A. Silica–air photonic crystal fiber design that permits waveguiding by a true photonic bandgap effect. Opt Lett 1999;24:46–8.
[15] Steel MJ, Osgood RM. Polarization and dispersive properties of elliptical-hole photonic crystal fibers. IEEE J Lightwave Technol 2001;19:495–503.
[16] Ferrando A, Silvester E, Miret JJ, Andres P, Andres MV. Full vector analysis of realistic photonic crystal fiber. Opt. Lett. 1999;24:276–8.
[17] Monro TM, Richardson DJ, Broderick NGR, Bennett PJ. Holey optical fibers: an efficient modal model. IEEE J. Lightwave Technol 1999;17:1093–101.

[18] Mogilevtsev D, Birks TA, Russell P StJ. Localized function method for modeling defect modes in 2-D photonic crystals. J Lightwave Technol 1999;17:2078–81.

[19] Saitoh K, Koshiba M. Full-vectorial imaginary-distance beam propagation method based on a finite element scheme: application to photonic crystal fibers. IEEE J Quantum Electron 2002;38:927–33.

[20] Koshiba M, Saitoh K. Structural dependence of effective area and mode field diameter for holey fibers. Opt Express 2003;11:1746–56.

[21] Koshiba M, Saitoh K. Finite-element analysis of birefringence and dispersion properties in actual and idealized holeyfiber structures. Appl Opt 2003;42:6267–75.

[22] Town GE, Lizer JT. Tapered holey fibers for spot-size and numerical aperture conversion. Opt Lett 2001;26:1042–4.

[23] TM Monro, KM Kiang, JH Lee, K Frampton, Z Yusoff, R Moore, et al., Highly nonlinear extruded single mode holey optical fibers, Proc. OFC'2002, OSA Technical Digest pp. 315–317, Anaheim, California, (2002).

[24] White T, McPhedran R, Botten L, Smith G, de Sterke CM. Calculations of air-guided modes in photonic crystal fibers using the multipole method. Opt. Express 2001;9:721–32.

[25] White TP, McPhedran RC, de Sterke CM, Botten LC, Steel MJ. Confinement losses in micro structured optical fibers. Opt. Lett. 2001;26:1660–2.

[26] Ghatak AK, Srivastava R, Faria IF, Thyagarajan K, Tiwari R. Accurate method for characterizing single-mode fibers: theory and experiment. Electron Lett 1983;19:97–9.

[27] Ghatak A, Thayagrajan K. Introduction to Fiber Optics. Cambridge Press; 1999.

[28] Mortensen NA, Folkenberg JR. Near-field to far-field transition of photonic crystal fibers: symmetries and interference phenomena. Opt. Express 2002;10:475–81.

[29] Dabirian A, Akbari M, Mortensen NA. The radiated fields of the fundamental mode of photonic crystal fibers. Opt Express 2005;13:3999–4004.

[30] Varshney AD, Sinha RK. Propagation characteristics of photonic crystal fiber: scalar effective index method and fully vectorial effective index method. Adv Studies Theor Phys 2007;1:75–85.

[31] Kuhlmey BT, Nguyen HC, Steel MJ, Eggleton BJ. Confinement loss in adiabatic photonic crystal fiber tapers. J Opt Soc Am B 2006;23:1965–74.

[32] Li Y, Yao Y, Hu M, Chai L, Wang C. Improved fully vectorial effective index method for photonic crystal fibers: evaluation and enhancement. Appl Opt 2008;47:399–406.

[33] Mortensen NA, Folken JR, Skovgaard PMW, Broeng J. Numerical aperture of single-mode photonic crystal fibers. IEEE PhotonTechnol Lett 2002;14:1094–6.

[34] Agarwal GP. Nonlinear Fiber Optics. third ed.1995.

Characterization of specially designed polarization maintaining photonic crystal fiber from far field radiation patterns

Kamal Kishor [a,*], R.K. Sinha [a], Anshu D. Varshney [a], Jaspreet Singh [b]

[a] TIFAC-Centre of Relevance & Excellence in Fiber Optics & Optical Communications, Applied Physics Department, Delhi Technological University, (Formerly Delhi College of Engineering), Bawana Road, Delhi 110 042, India
[b] Fiberonics India Ltd, Delhi, India

ARTICLE INFO

ABSTRACT

We report the development of theory and experiment for the characterization of polarization maintaining photonic crystal fiber (PM PCF) from far field intensity measurements. In this specially designed photonic crystal fiber, the air hole diameters along orthogonal axes adjacent to the core region are different, and hence create an effective index difference between the two orthogonal polarization modes. From the experimental measurements of the far field radiation pattern, we obtain transmission characteristics of PM PCF in terms of mode field diameters (MFD), V-values along major and minor axes, mode field area, birefringence, core radius, effective refractive index of cladding and numerical apertures along major and minor axes of PM PCFs. It is shown that the experimentally obtained geometrical and wave guiding parameters of the PM PCF match with the manufacturer/simulation/scanning electron microscope (SEM) data within the experimental limits.

© 2010 Elsevier B.V. All rights reserved.

1. Introduction

Polarization Maintaining Fibers (PMFs) are required for high bit rate optical fiber communication systems as polarization mode dispersion (PMD) can be eliminated in PMFs. To transmit the stable state of polarization it is important to use the specialty optical fibers i.e. PMFs. These fibers work by inducing a birefringence within the fiber core, which refers to a difference in the propagation constant of light wave traveling through the fiber for two orthogonal directions of polarizations. Birefringence is created within a PMF either by forming a non-circular fiber core (shape induced birefringence), or by inducing constant stresses within the fiber with stress applying parts (SAP) and is called stress induced birefringence. Birefringence breaks the circular symmetry in an optical fiber, creating two principal transmission axes within the fiber, known as the fast and slow axes of the fiber according to the effective refractive index experienced by the propagating modes.

PMFs find extensive applications in coherent optical communication systems and in polarization sensitive experiments including design and development of optical fiber based sensors. Elliptical Core, Bow Tie and PANDA fibers etc. are conventionally referred as PMFs and their modal birefringence are reported in the order of 5×10^{-4} [1–3]. New designs of optical fibers, exhibiting higher birefringence and thereby enhancing their polarization maintaining capability, are needed to meet the requirement of low PMD in optical communication systems and networks.

In the recent past, design, simulation and fabrication of Photonic Crystal Fibers (PCFs) are being reported. PCFs are the recent advancement in optical fiber technology and have generated great amount of interest, as they exhibit many superior transmission characteristics with high degree of design flexibilities [4–6]. The transition from near field to the far field of the fundamental mode radiating out of a PCF is also investigated experimentally and theoretically, where it is observed that six satellites form around a nearly Gaussian far field pattern from conventional (i.e. index guided solid core) PCF, which qualitatively explains all the observed phenomena and quantitatively predicts the relative intensity of the six satellites in the far field region [7]. Six fold rotational symmetry and its implication in the measurement of the far field intensity pattern of conventional PCF is described by Mortensen et al. [8]. However these methods do not attempt to characterize PCF in terms of its geometrical and waveguiding parameters. Further, it has been reported that the far field measurement is an excellent method to characterize conventional PCF [9,10], which forms a basis for using far field intensity patterns to characterize such specialty optical fibers.

With photonic crystal structure, it is possible to design highly birefringent fiber which serves as polarization maintaining (PM) PCF. In case of PCFs, birefringence can be easily tailored and enhanced [11–14]. Recently PM PCFs have been fabricated using two different air hole diameters along two orthogonal axes near the core region (Fig. 1), which provides an effective index difference between two orthogonal polarization modes and their transmission characteristics exhibiting high birefringence in the order of 10^{-3}, is reported

* Corresponding author.
 E-mail address: kishorkamal1@rediffmail.com (K. Kishor).

(a)

(b)
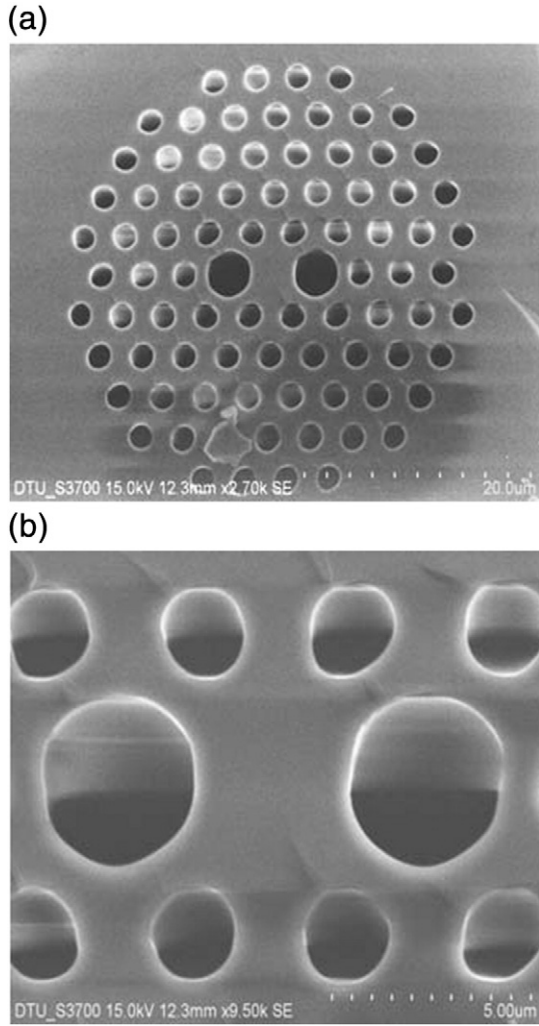
Fig. 1. SEM images of PM PCF, Pitch, Λ — 4.4 μm, large hole diameter — 4.5 μm, small hole diameter — 2.2 μm.

[15–18]. This value of birefringence is one order higher in magnitude than that of conventional PMFs. Transmission characteristics of such PM PCF depend on the waveguiding (e.g., MFD, V-values along major and minor axes and birefringence etc.) and geometrical (core radius of major and minor axes of PM PCFs, air hole diameters, etc.) parameters of PM PCF. Therefore the knowledge of these waveguiding and geometrical parameters are required to assess the performance and transmission characteristics of PM PCFs.

In this paper, we report the development of a theory and experiment for the characterization of PM PCF from far filed intensity measurements. From the experimental measurements of the far field intensity pattern, we obtain transmission characteristics of PM PCF in terms of MFD, V-values along major and minor axes, mode field area, birefringence, core radius and numerical apertures of major and minor axes of PM PCFs. The experimental values of the geometrical and waveguiding parameters are found to be in agreement with the manufacturer, simulation and Scanning Electron Microscopy (SEM) data for this PM PCF. It is expected that the theory and experiment reported in this paper will find extensive application in design, development and online characterization of PM PCFs.

2. Theory

In this paper, we have used far field intensity measurements for estimation of geometrical and waveguiding parameters of PM PCF. The far field region is also referred as the Fraunhofer region; it is the region

where the angular field distribution is essentially independent of distance from the source. The cross sectional views of the spot size of PM PCF used in our experiment is found to be elliptical in its near and far field regime (Fig. 2) and hence it is considered as an elliptical core fiber. The propagation characteristics of elliptical core optical fiber had been obtained accurately by its equivalent Rectangular Core Waveguide (RCW), having the same aspect ratio, core areas and core-cladding refractive index difference [19].

The elliptical cross section of PM PCF is approximated to be rectangular shape for obtaining the far field intensity expression in our analysis. Propagation characteristics of the elliptical core waveguide have been successfully obtained from the equivalent rectangular core waveguide (Fig. 3) having the same aspect ratio, core areas and core-cladding refractive indices[19,20] and is briefly described as follows:

Refractive Index Profile of elliptical core can be given by Eqs. (1a) and (1b).

$$n^2(x,y) = n_1^2, \text{ for} \left(\frac{x^2}{a'^2} + \frac{y^2}{b'^2} \right) < 1.0 \tag{1a}$$

$$n^2(x,y) = n_2^2, \text{ for} \left(\frac{x^2}{a'^2} + \frac{y^2}{b'^2} \right) > 1.0 \tag{1b}$$

Further, elliptical core is approximated by the pseudo rectangular core waveguide having following refractive index distribution:

$$n^2(x,y) = n'^2(x) + n''^2(y) - n_1^2 \tag{2}$$

where

$$
\begin{aligned}
n'(x) &= n_1 \quad |x| < a \\
&= n_2 \quad |x| > a
\end{aligned}
$$

and

$$
\begin{aligned}
n''(y) &= n_1 \quad |y| < b \\
&= n_2 \quad |y| > b
\end{aligned}
$$

where $a/a' = b/b' = \sqrt{\pi}/2$, as area of rectangle (4ab) = area of ellipse ($\pi a' b'$).

Thus, the elliptical cross section of PM PCF can be considered as two crossed slab waveguides.

The far field radiation pattern $\psi(r, \theta, \phi)$ is the inverse Fourier transform of the aperture or near fields. The normalized (with respect to $\theta = 0$) far field intensity distribution for the fundamental
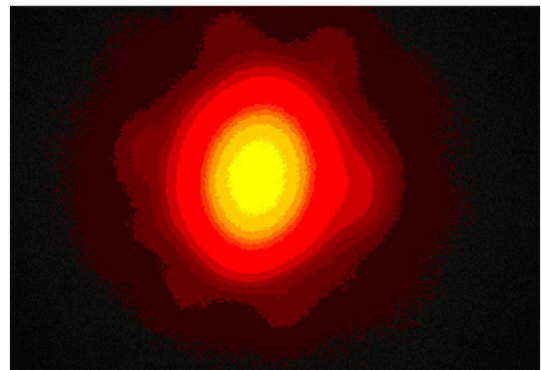
Fig. 2. Far field pattern of PM PCF.
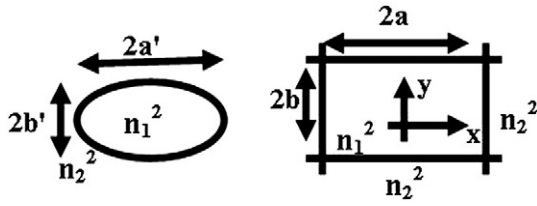
Fig. 3. Transverse cross section of elliptical core described by the refractive index profile with its equivalent pseudo same rectangular core waveguide described by the refractive index profile.

Fig. 5. Variation of the ratio α_{10}/α_{50} (red) and α_{50} (black) with V-parameter.

TE mode [19] of symmetric slab waveguide is given in Eqs. (3a) and (3b).

for $U \neq \alpha$

$$|\Psi|^2 = \left[\frac{U^2 W^2}{(U^2 - \alpha^2)(W^2 + \alpha^2)} \left\{ \cos\alpha - \alpha\sin\alpha \frac{\cos U}{U\sin} U \right\} \right]^2 \qquad (3a)$$

for $U = \alpha$

$$|\Psi|^2 = \left[\frac{U^2 W^2}{(2V^2)(U\sin U)} \left\{ \frac{\cos^2\alpha - \sin^2\alpha + \sin 2\alpha}{2\alpha} \right\} \right]^2 \qquad (3b)$$

where $V^2 = U^2 + W^2$; $\alpha = ka\sin\theta$; $k = \frac{2\pi}{\lambda_0}$; λ_0 is the free-space wavelength and 'a' is the half-thickness of the core along the respective axes. It is mentioned here that far field intensity corresponding to TE mode is used as the transcendental equation for TE mode propagation does not depend on refractive indices directly unlike TM modes [21,22] and hence the above mentioned expression for far field intensity and its pattern (Fig. 4) is widely used for the characterization of optical waveguides [19–21].
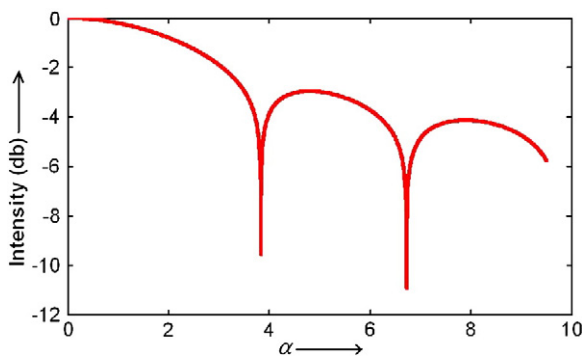
The universal curves (Fig. 5) for far field intensity pattern of the slab waveguides is obtained from the above equations and is used for estimating the core dimensions and hence aspect ratio of the core of PM PCF.

It is noted that α_{10} and α_{50} are the values of $\alpha(= ka\sin\theta)$, which correspond to angles in the far field intensity pattern at which the intensity drops to 10% and 50% of its maximum value (at $\theta = 0°$.). The intensities are measured at θ_{10} because it is practically very difficult to measure the first minimum intensity position accurately in far field intensity pattern [23].
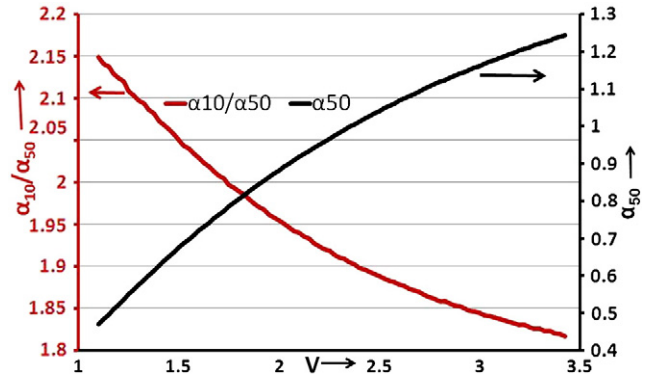
3. Experimental setup and characterization method

3.1. Experimental setup

This setup consists of a Helium–Neon laser with wavelength 633 nm, microscopic lens, fiber chuck and holders, polarizer sheet (to

find the polarization axes of laser and polarization of the output light from PM PCF), detector with digital display and 20 m long PM PCF. The far field output of the detector is measured in the digital display. A schematic diagram [24] to record far field intensity pattern of PM PCF is depicted in Fig. 6 whereas the real experiment setup is exhibited in Fig. 7.

3.2. Characterization methods

The PM PCF ends are stripped and cleaved properly to minimize the reflection losses. The TE mode is excited in the fiber after identifying the polarization axes of both the laser and the fiber. The output far field intensity pattern is recorded and the light intensity pattern is recorded and the light intensity was fed into the digital display. The far field intensity variation of the fundamental TE mode along the major and minor axes of the PM PCF is displayed in Figs. 8 and 9 respectively.

From Figs. 8 and 9, we obtain the angles corresponding to the fall of intensity to 10% and 50% of its maximum value. The corresponding values for these two angles θ_{10} and θ_{50} are tabulated Table 1. After noting down the angles θ_{10} and θ_{50}, we calculate the sine ratio of these two angles i.e. $\sin\theta_{10}/\sin\theta_{50}$.

From the universal graph (Fig. 5) for the slab waveguide, the V-values are obtained corresponding to experimental values of $\sin\theta_{10}/\sin\theta_{50}$ along both axes. For the respective V numbers the corresponding $\alpha_{50}(= k_0 a\sin\theta_{50})$ is calculated from the right hand ordinate of the universal graph (Fig. 5). Since θ_{50} is known, the core radius along the respective axes is calculated with the value

Fig. 4. Far field intensity pattern for the slab-wave guide.
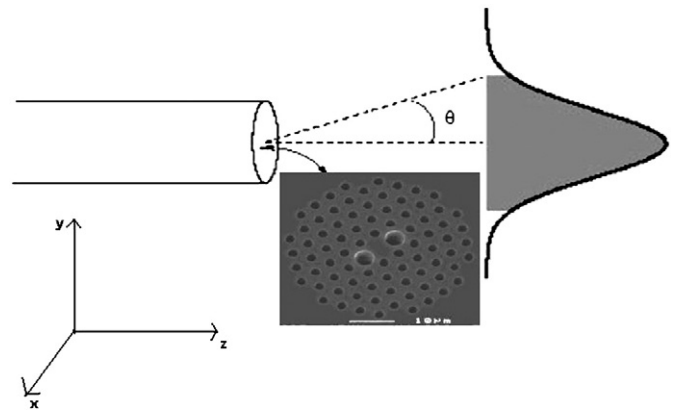
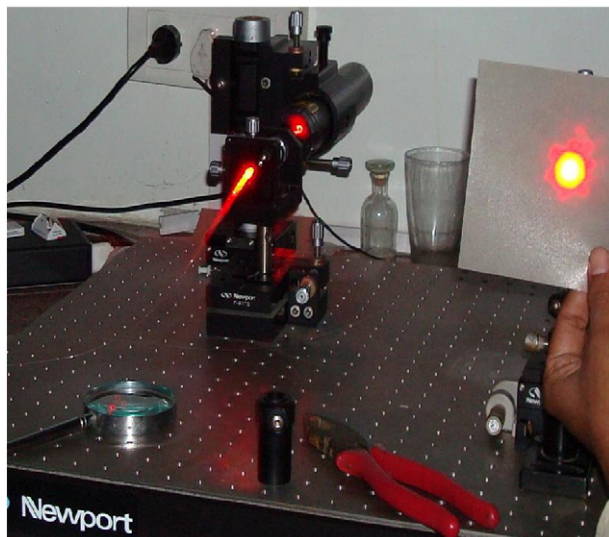**Fig. 6.** Line sketch of the far field intensity pattern.

Fig. 7. Experimental arrangement for the far field measurement.

of α_{50}; at the known operating wavelength (633 nm). Thus, by measuring far field intensity angles at which the intensity has dropped to 10% and 50% of its maximum value, the core radius for the pseudo rectangular waveguide are calculated. From this data, the core dimension of the elliptical core of this PM PCF has been calculated using aspect ratio for pseudo rectangular waveguide and elliptical PM PCF i.e. $a/a' = b/b' = \sqrt{\pi}/2$.

Since V-parameter and core dimension are obtained, the numerical apertures $\left(\sqrt{n_1^2 - n_2^2}\right)$ along the both axes are calculated. Further, refractive index of core is n_1 (=1.45), effective refractive index of cladding $n_2 (= n_{clad})$ is calculated using the value of numerical aperture. Once we have the effective refractive index of cladding (n_{clad}), we calculated the effective refractive index of the guided mode (n_g) along the two orthogonal axes of PM PCF with the R-Soft. From the knowledge of the effective refractive index of the guided mode along two mutually orthogonal axes, the birefringence $(n_{gx} - n_{gy})$ induced in the given PM PCF is obtained.

Further, we find the experimental value of θ_e, the angle where the far field intensity falls to the $1/e^2$ of the maximum intensity from the measured far field intensity curve. The MFD of propagating light wave is obtained with the help of the formula of MFD ($= 2\lambda_0/\pi \sin\theta_e$) for both the axes [22,25]. From MFD of PM PCF along two orthogonal axes we calculate the mode field area ($= \pi xy/4$): where x, y are the MFD of the PM PCF along the two orthogonal axes.
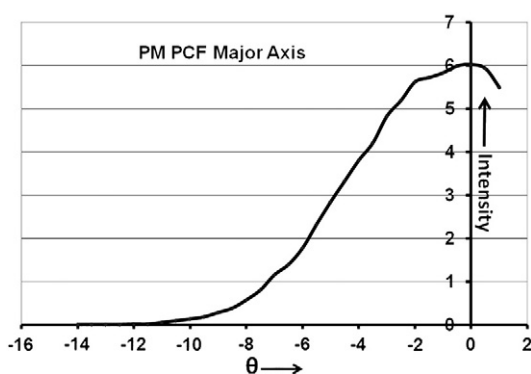

Fig. 8. Measured far field intensity distribution along the major axis.
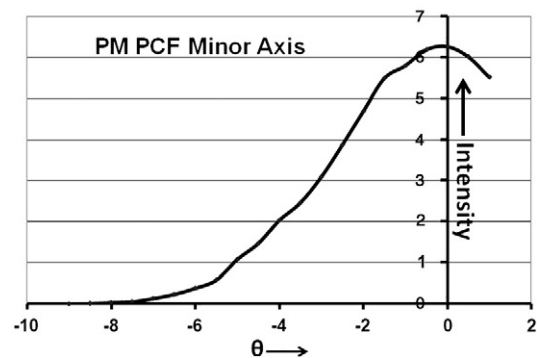

Fig. 9. Measured far field intensity distribution along the minor axis.

3.3. Verification of experimental results for characterization for given PCF from R-SOFT simulation

We have used manufacturer (Blaze Photonics) data for the given PM PCF as mentioned below:

1. Pitch, Λ (Spacing between adjacent holes) — 4.4 µm.
2. Large hole diameter — 4.5 µm.
3. Small hole diameter — 2.2 µm.

Using R-SOFT simulator (band solve), we have modeled the PM PCF by taking into account the manufacturer data. We have calculated V-parameter, effective refractive index of cladding and guided mode along the two orthogonal axes. With calculated effective index for cladding $(n_2 (= n_{clad}))$ and knowledge of refractive index of the core $(n_1) = 1.45$, numerical aperture $\left(\sqrt{n_1^2 - n_2^2}\right)$ along the two axes and birefringence $(n_{gx} - n_{gy})$ for PM PCF are obtained and these values are mentioned in Table 2.

4. Results and discussion

It is mentioned that the major axis in the near field becomes minor axis in far field and the minor axis in near field becomes the major axis in far field, which is expected also from diffraction phenomena. MFD of the PM PCF is provided by the manufacturer, and we experimentally also measured it, using the formula "MFD $= 2\lambda_0/\pi \sin \theta_e$" for both axes. Our experimental result of MFD is found to be in close agreement with the manufacturer data within the experimental limits.

From the experimentally obtained value of MFD for both axes, mode field area is obtained and also found to be in close agreement with the manufacturer's data.

Core radius along two axis i.e. semi major and semi minor axes is calculated by using universal graph (Fig. 5) and these values are verified with SEM measurement and are found to be in agreement with each other.

The V-parameter of the PM PCF along both axes is obtained from the universal graph (Fig. 5), using the experimental value of $\sin \theta_{10}/\sin \theta_{50}$ and are verified with the simulation result of R-Soft Band solver.

The numerical aperture $\left(\sqrt{n_1^2 - n_2^2}\right)$ along the two axes is calculated by using the above obtained values of V-parameters and

Table 1
Scanning data along the major and minor axes of the far field.

Figure (far field)	θ_{10}	θ_{50}	$\alpha_{10}/\alpha_{50} = \sin \theta_{10}/\sin \theta_{50}$	$\alpha_{50} = k_0 a \sin \theta_{50}$
Scanning ↕ ⬭ ↔ Polarization	5.5°	3°	1.8313	1.198
Polarization ↕ ⬭ ↔ Scanning	8°	4.25°	1.87796	1.068

Table 2
Comparison between manufacturer/simulation/SEM data and experimental results.

	Manufacturer's-(a)/ simulation data (b)/ measured from SEM (c)		Experimental results
MFD (μ)	Axis-1 (x)	3.1 (a)	3.08
	Axis-2 (y)	3.6 (a)	3.79
Mode field area (μ^2)	$\pi xy/4$	8.7606 (a)	9.163462
Core radius (μ)	Axis-1	$b' = 1.445$ (c)	$b = 1.28754, b' = 1.45284$
	Axis-2	$a' = 2.285$ (c)	$a = 2.0454, a' = 2.308$
Effective refractive index of cladding (n_{clad})	Axis-1	1.43298 (b)	1.43860
	Axis-2	1.44086 (b)	1.44335
Effective refractive index of guided mode (n_g)	Axis-1	1.445459 (b)	1.445212
	Axis-2	1.447837 (b)	1.447869
Birefringence	0.002378 (b)		0.002657
V-parameter	Axis-1	2.8295 (b)	2.65
	Axis-2	3.2985 (b)	3.175
Numerical aperture	Axis-1	0.22151 (b)	0.18146
	Axis-2	0.16254 (b)	0.13871

the core radius and are verified with the simulation result of R-Soft Band solver. The effective refractive index of cladding for given PM PCF along the two axes is calculated by using core refractive index $(n_1) = 1.45$ and the numerical aperture and are verified with the simulation result obtained from R-Soft Band solver. The experimental effective refractive index of the guided modes (n_g) along the two orthogonal axes is obtained with the R-Soft by using the experimentally obtained effective refractive index of cladding.

It is mentioned here that the experimental value of numerical aperture is obtained directly from the universal graph after obtaining V value and core radius along the respective axis. In simulation data, the numerical aperture is obtained indirectly, i.e. first we obtain the effective refractive index of the guided mode, followed by the assumption of the core refractive index as 1.45 at $\lambda = 0.633$ μm, and there after we obtain the effective cladding index, which is used for the calculation of numerical aperture of the PM PCF along their respective axis. From these data, it is found that the difference between the simulation and experimentally obtained value of the numerical aperture is very small and falls within experimental limit.

The birefringence $(n_{gx} - n_{gy})$ induced in the given PM PCF is obtained from the effective refractive index of the guided mode along two mutually orthogonal axes and is verified with the simulation result of R-Soft Band solver, where it is shown that the birefringence is in the order of 10^{-3}.

Experimental results for the determination of wave guiding and geometrical parameters for the given PM PCF are found to match with the manufacturer/simulation results by plane wave expansion method using the R-Soft Band solver as well as from the SEM measurements, which have been compared and tabulated in Table 2. "Axis-1" is the axis along big air holes act as minor axis in the near field and major axis in the far field and hence yields lower effective refractive index in the cladding along the big air holes, similarly "Axis-2" is the axis along the regular air holes act as major axis in the near field and minor axis in the far field and yields larger value of effective refractive index in the cladding. As a result modal birefringence is introduced.

5. Conclusion

Far field method is applied to characterize PM PCF in terms of its waveguiding and geometrical parameters. It is shown that the waveguiding and geometrical parameters obtained from the far field measurement of PM PCF match with the manufacturer/simulation/ SEM data within the experimental limits. Thus, this method provides a useful tool for online characterization of PM PCF. It is expected that this method will serve as standard technique to characterize PM PCF and will also be useful to design and develop application specific to PM PCF for both optical communication and in sensor systems.

Acknowledgement

References

[1] R.D. Birch, D.N. Payne, M.P. Varnham, Electron. Lett 18 (1982) 1036.
[2] T. Hosaka, K. Okamoto, T. Miya, Y. Sasaki, T. Edahiro, Electron. Lett 17 (1981) 530.
[3] J. Noda, K. Okamoto, Y. Sasaki, J. Lightwave Technol. LT-4 (1986) 1071.
[4] J.C. Knight, T.A. Birks, P.St.J. Russell, D.M. Atkin, Opt. Lett. 21 (1996) 1547.
[5] J. Broeng, D. Mogilevstev, S.E. Barkou, A. Bjarklev, Opt. Fiber Technol. 5 (1999) 305.
[6] T.A. Birks, J.C. Knight, B.J. Mangan, P.St.J. Russell, IEICE Trans. Electron. E84-C (2001) 585.
[7] N.A. Mortensen, J.R. Folkenberg, Opt. Express 10 (2002) 475.
[8] A. Dabirian, M. Akbari, N.A. Mortensen, Opt. Express 13 (2005) 3999.
[9] S.K. Varshney, R.K. Sinha, J. Microw. Optoelectron. 2 (2002) 32.
[10] M. Szustakowski, N. Pałka, W. Grabiec, J. Telecom. Info. Tech. 2 (2007) 109.
[11] Blanch A. Ortigosa, J.C. Knight, W.J. Wadsworth, J. Arriaga, B.J. Mangan, T.A. Birks, P.St.J. Russell, Opt. Lett. 25 (2000) 1325.
[12] S. Kawanishi, K. Okamoto, IEICE Soc. Conf. 2000 (2000) B (in Japanese).
[13] S.B. Libori, J. Broeng, E. Knudsen, A. Bjarklev, H.R. Simomsen, Proc. Optical Fiber Conference (OFC), OSA Proceedings Series, Vol. 54, Optical Society of America, Washington, D.C, 2001, TuM2.
[14] T.P. Hansen, J. Broeng, E.B. Libori, E. Knudsen, A. Bjarklev, J.R. Jensen, H. Simonsen, IEEE Photon. Tech. Lett. 13 (2001) 588.
[15] Tanaka Masatoshi, Fujita Moriyuki, Opt. Express 9 (2001) 676.
[16] Partha Roy Chaudhuri, Varghese Paulose, Chunliu Zhao, Chao Lu, IEEE Photonics Tech. Lett. 16 (2004) 1301.
[17] A.D. Varshney, R.K. Sinha, Appl. Opt. 46 (2007) 5912.
[18] A.D. Varshney, R.K. Sinha, Int. J. Microw. Opt. Tech. 4 (2009) 324.
[19] R.K. Sinha, LEOS 1997, 10th Annual Meeting Conference Proceedings, IEEE, 2, 1997, p. 50.
[20] A. Kumar, R.K. Varshney, Opt. Quant. Electron. 16 (1984) 349.
[21] A.C. Boucouvalas, IEEE Elec. Lett. 19 (1983) 120.
[22] A. Ghatak, K. Thayagrajan, Introduction to Fiber Optics, Cambridge Press, 1999.
[23] A.K. Ghatak, R. Srivastava, I.F. Faria, K. Thyagarajan, R. Tiwari, Electron. Lett 19 (1983) 97.
[24] N.A. Mortensen, J.R. Folken, P.M.W. Skovgaard, J. Broeng, IEEE Photon. Technol. Lett. 14 (2002) 1094.
[25] Young Matt, Appl. Opt. 37 (1998) 5605.

Tunable negative refractive index metamaterial from V-shaped SRR structure: fabrication and characterization

Kamal Kishor,[1] Monu Nath Baitha,[1] R. K. Sinha,[1,*] and Basudev Lahiri[2]

[1]*TIFAC-Centre of Relevance & Excellence in Fiber Optics & Optical Communications, Applied Physics Department, Delhi Technological University (Formerly Delhi College of Engineering), Bawana Road, Delhi 110 042, India*
[2]*School of Engineering, University of Glasgow, Glasgow G12 8LT, UK*
*Corresponding author: dr_rk_sinha@yahoo.com

In this paper, we report the fabrication and characterization of a V-shaped split ring resonator (SRR) metamaterial and have shown that it is possible to tune a negative refractive index by changing the angular gap of V-shaped SRR. Our experimental characterization results are well supported by simulation results using the FDTD method. The reported design of a V-shaped SRR structure has the distinctive advantage of having its capacitance varied by changing the angular gap between its arms. It is also observed that the electromagnetic parameters (such as permittivity and permeability) of metamaterials can be tuned as per our requirement by varying the angular gap.   © 2014 Optical Society of America

OCIS codes: (160.3918) Metamaterials; (350.3618) Left-handed materials; (220.4241) Nanostructure fabrication.

http://dx.doi.org/10.1364/JOSAB.31.001410

1. INTRODUCTION

Metamaterials have been in prime focus for the past few years with the number of publications and patents increasing exponentially due to their highly uncommon electromagnetic properties and applications such as negative refraction, reverse Doppler effect, flat lens, cloaking, etc. [1–17]. It is possible to design metamaterials due to the dispersive nature of materials, i.e., electric permittivity and magnetic permeability are functions of the radiation frequency [1–3,10]. Metamaterials provide precise control over the flow of electromagnetic waves [9]. The main challenge in the design of metamaterials is to design a structure that shows electric permittivity and magnetic permeability simultaneously negative for the desired frequency range within its characteristic size [1–3,8].

Due to this challenge and uncommon electromagnetic properties, it took a long 30 years after Veselago in 1968 [1] for the practical realization of metamaterials by Smith *et al.* 2000 [7], who used metallic split ring resonators (SRRs) of dimension smaller than the wavelength of light as basic building block (basic units) of a metamaterial. After Smith *et al.*, scientists proposed various different metamaterial unit structures such as Ω-shaped, circular, U-shaped, S-shaped, I-shaped, H-shaped, asymmetric-type split ring structures, to name a few, for various applications such as antenna and optical sensing [18–24].

In almost all cases, SRRs are fabricated as periodic arrays of metallic structures whose dimensions are smaller than the wavelength of radiation. The collective oscillations of conducting electrons in these metallic structures (known as localized surface plasmon) determine the overall electromagnetic response of the entire material [25–31]. By adjusting the dimensions and geometries of these SRRs, a customized electromagnetic response can be obtained. The C-shaped SRR is arguably the most common element used in forming the basic microstructure of metamaterials resonating in the infrared regime [26–30]. SRRs, in their fundamental resonance, behave as LC oscillatory circuits containing a single-turn magnetic coil of inductance in series with a capacitance produced by the gap between the arms. For normal incidence with TE polarization mode, with an incident electric field across its gap, the electric field couples with the capacitance of the SRR and generates a circulating current across it. This circulating current induces a magnetic field at the bottom of the SRR that interacts with the external field to generate the magnetic resonance identified as an LC resonance by Linden *et al.* [32]. The LC resonance of the SRR is given as $\omega_{LC} = 1/\sqrt{LC}$ and is inversely proportional to the size (dimension) of SRRs. For the TM polarization mode, where the electric field is perpendicular across the SRR gap, no circulating current could be produced and therefore results in no LC resonance only with the plasmon resonance being present.

In this paper, we report on the fabrication and characterizations of a V-shaped SRR metamaterial and have shown its angular-gap-dependent tunable negative refractive index (NRI) characteristics. The reported V-shaped SRR structure and angular-gap-dependent NRI, to the best of our knowledge is so far not studied. The unique property of this structure is that by varying the angular gap between its arms, we can change the capacitance (C) for the structure, and hence we can tune and control the NRI. We experimentally and computationally investigated the interdependence of the capacitance (C) and inductance (L) of the structure, and we observed that

by changing the angular gap of V-shaped SRRs, it is possible to control/tune their NRI at the corresponding resonance wavelength. Exploiting this important result for the extraordinary electromagnetic properties of the reported structure, we can use this structure for tunable metamaterial devices, e.g., the design of receiver and transmitter antenna for the desired frequency/application range.

2. FABRICATION AND MEASUREMENT

A 2D array of ~50 nm thick gold based V-shaped SRRs were fabricated on n-doped silicon substrate over an area of ~300 × 300 μm using a combination of electron beam lithography (EBL) technique and metal lift-off. The width of the arms for the V-shaped structure was kept at ~0.1 μm and the

arm length at ~1 μm. We fabricated and studied eight different samples of reported structure with angular gap of 0°, 20°, 40°, 60°, 90°, 120°, 150°, and 180°. The reflectance measurements were done using a Nicolet continuum Fourier transform infrared (FTIR) spectroscope fitted with a case grain objective of 10× magnifications and an NA of 0.25. A zinc selenide polarizer was used to polarize the incident light. The measurements were taken for both orthogonal linear polarizations of the incident light (TE and TM polarization) and were then normalized with respect to the reflectivity of a bare silicon substrate. All measurements were taken at normal incidence.

Figure 1 shows the geometry and dimensions of the reported structure. Figure 1(a) shows the geometry of the structure for angular gap of $\alpha°$ (α may be 20°, 40°, 60°, 90°, 120°, 150°); Fig. 1(b) is for an angular gap of 0°, which looks like single arm or longitudinally parallel rods; similarly Fig. 1(c) shows the structure for an angular gap of 180° where both arms open in the opposite direction and look like horizontally parallel rods. Figure 1(d) charts the dimension of all the samples for a different angular gap.

3. MODELING AND SIMULATION

Modeling and simulation for reported V-shaped metamaterial is performed using the Omnisim FDTD simulation package of Photon Design, UK. We used the Drude model to describe the complex dielectric constant of the gold layer. The reflection and transmission spectra for the modeled structures are simulated as a function of wavelength.

4. RESULTS AND DISCUSSION

The reflectance resonance response (both experimental and simulation) of samples with an angular gap of 20°, 60°, and 120° are shown in Fig. 2. The 0° and 180° angular gap samples (having minimum and maximum gaps) represented

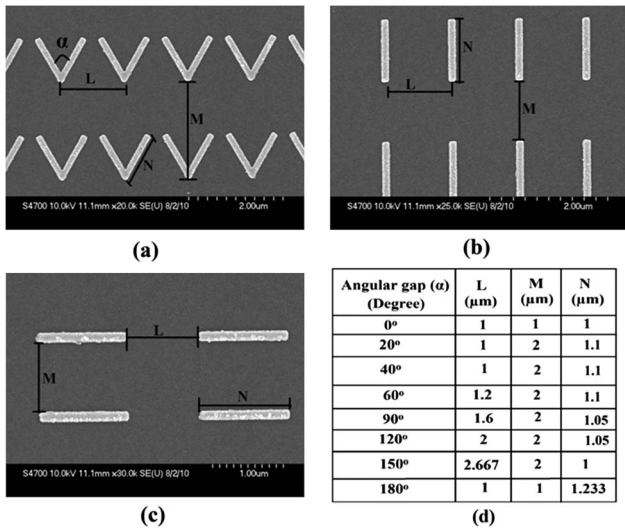| Angular gap (α) (Degree)	L (μm)	M (μm)	N (μm)
0°	1	1	1
20°	1	2	1.1
40°	1	2	1.1
60°	1.2	2	1.1
90°	1.6	2	1.05
120°	2	2	1.05
150°	2.667	2	1
180°	1	1	1.233

Fig. 1.   Geometry and dimensions of the reported structure.
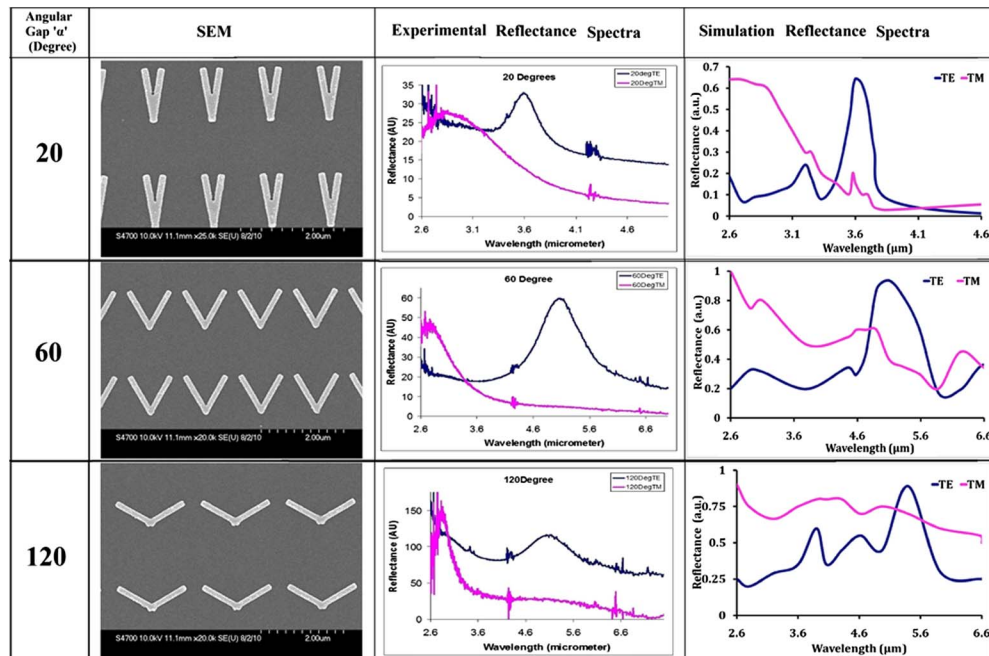

Fig. 2.   Reflection spectra for SRR structure samples of 20°, 60°, and 120° angular gap; first column shows scanning electron microscope (SEM) images of the samples; second column shows experimentally obtained reflection spectra for both TE and TM polarization; third column shows reflection spectra obtain by FDTD simulation.

horizontal metallic rods instead of SRRs and produced no significant resonance response, as expected. But the LC and plasmon resonance response is significant and observable for the structures with the angular gap (α) of 20°, 40°, 60°, 90°, 120°, and 150° for the TE polarization mode with the electric field parallel across the SRR gap. The most significant observation is that position of LC resonance peak in the samples varying from 3.6 to 5.6 μm wavelength ranges by varying the angular gap from 20° to 150°, respectively. These experimental observations were confirmed with the simulation results obtained from the Omnisim FDTD simulation package within experimental limits.

Figure 3 shows the significant shift in resonance (LC) peak with respect to the angular gap for TE polarization (experimental as well as simulated).

The characterization of metamaterial structure in terms of its electromagnetic parameters, such as the real and imaginary value of electrical permittivity, magnetic permeability, refractive index, and impedance etc. are required to exploit its

amazing electromagnetic properties. In the recent past, several methods have been reported for the characterization of metamaterials and to evaluate their electromagnetic parameters [33–41]. We used the Minowa *et al.* method [41] to compute the electromagnetic parameters by using the reflection and transmission coefficients obtained by simulation results. The following formulas are used:

$$z^2 = \frac{T'^2 - (1 + R')^2}{T'^2 - (1 - R')^2}, \tag{1}$$

$$n = \frac{c}{i\omega d} \ln\left[\frac{(1 + z)R'}{(1 - z)T'} + \frac{1}{T'}\right], \tag{2}$$

$$T' = Te^{\left(\frac{i\omega d}{c}\right)}, \tag{3}$$

$$R' = -R, \tag{4}$$

$$\varepsilon = \frac{n}{z}, \tag{5}$$

$$\mu = nz, \tag{6}$$

where T is the transmission coefficient, R is the reflection coefficient, d is effective thickness of the gold layer, c is the velocity of light in vacuum, $\omega = 2\pi/\lambda$, z is the impedance, n is the refractive index, ε is the electric permittivity, and μ is the magnetic permeability.

From Fig. 5, it is clear that the refractive index is negative for the reported structure at the LC resonance frequency. This observation confirms that our structure is behaving as NRI metamaterial at corresponding resonant frequency.
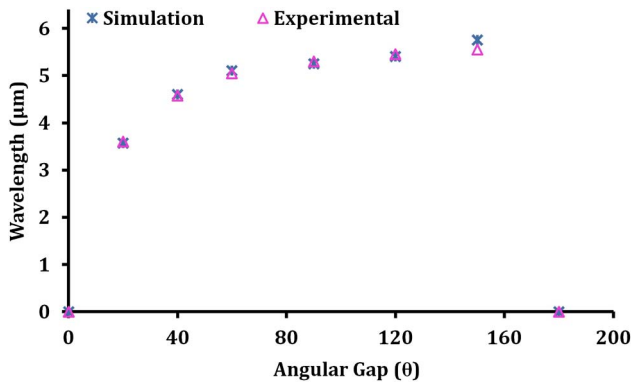
Fig. 3.   Position of LC peak with respect to angular gap.
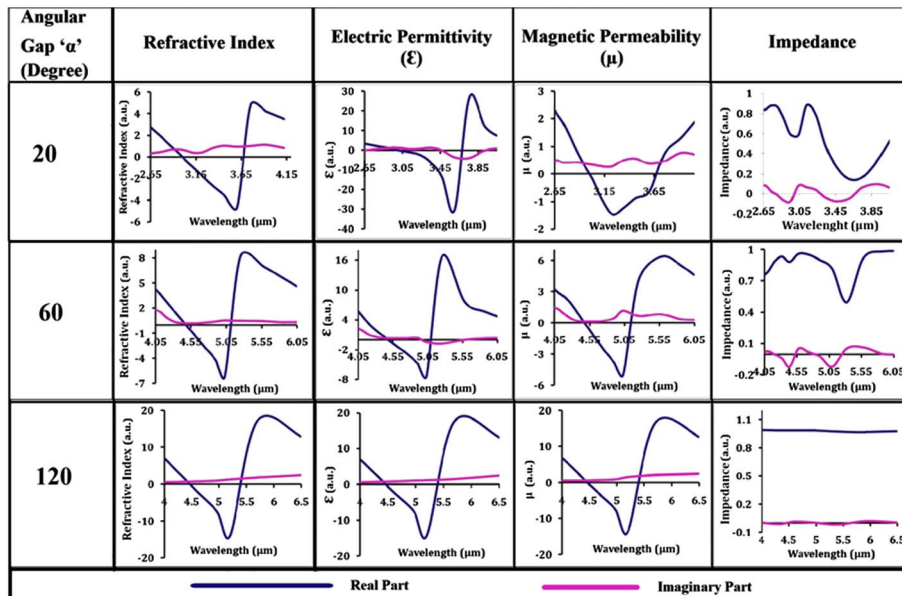
Fig. 4.   Electromagnetic parameters with respect to wavelength for SRR structure samples of 20°, 60°, and 120° angular gaps; first column shows results for variation in refractive index w.r.t. wavelength for samples; second column shows results for variation in electrical permittivity w.r.t. wavelength; third column shows results for variation in magnetic permeability w.r.t. wavelength; fourth column shows results for variation in impedance w.r.t. wavelength (blue curve is for real part; pink curve is for imaginary part).

Fig. 5.   Plot of refractive index against different value of angular gap.

From Figs. 4 and 5, it can be clearly seen that, by changing the angular gap of the V-shaped SRRs, their LC resonance position changes, and the NRI of the structure increases constantly at the corresponding resonance position. This is significant for practical applications of negative index metamaterials in waveguides and cloaking because signals obtained near resonance response of materials tend to be lossy and difficult for real-life applications [24,39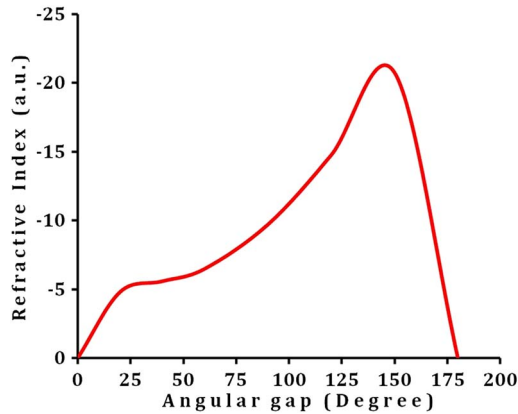]. In case of V-shaped SRRs, we have the advantage of increasing the NRI just by increasing the angular gap. To the best of our knowledge, this facility cannot be harnessed in other structures, e.g., the C-shaped SRRs. This also proves that the electromagnetic parameters (such as permittivity and permeability) of metamaterials also can be tuned as per our requirement by varying the angular gap.

5. CONCLUSION

In this paper, we report a new design of a metamaterial structure, similar to the English letter V, and performed experimental and computational investigations of the structure. In this work, we describe the behavior of a V-shaped SRR. By changing the angular gap of V-shaped SRRs, it is possible to vary the NRI of the structure. Our experimental results are well corroborated by simulations to show that electromagnetic parameters (such as ε, μ, n, etc.) can be tuned with the variation of the angular gap between the arms of V-shaped SRRs. Thus the reported structure for the metamaterial will put a significant mark in the design and development of metamaterials based optical switch, tunable devices, and sensors etc.

ACKNOWLEDGMENTS

REFERENCES

1. V. G. Veselago, "The electrodynamics of substances with simultaneously negative values of permittivity and permeability," Sov. Phys. Usp. **10**, 509–514 (1968).
2. J. B. Pendry, "Negative refraction makes a perfect lens," Phys. Rev. Lett. **85**, 3966–3969 (2000).
3. R. A. Shelby, D. R. Smith, S. C. Nemat-Nasser, and S. Schultz, "Microwave transmission through a two dimensional, isotropic, left-handed metamaterial," Appl. Phys. Lett. **78**, 489–491 (2001).
4. R. A. Shelby, D. R. Smith, and S. Schultz, "Experimental verification of a negative index of refraction," Science **292**, 77–79 (2001).
5. J. B. Pendry, A. J. Holden, D. J. Robbins, and W. J. Steward, "Low frequency plasmons in thin-wire structures," J. Phys. Condens. Matter **10**, 4785–4809 (1998).
6. J. B. Pendry, A. J. Holden, D. J. Robbins, and W. J. Steward, "Magnetism from conductors and enhanced nonlinear phenomena," IEEE Trans. Microwave Theory Tech. **47**, 2075–2084 (1999).
7. D. R. Smith, W. J. Padilla, D. C. Vier, S. C. Nemat-Nasser, and S. Schultz, "Composite medium with simultaneously negative permeability and permittivity," Phys. Rev. Lett. **84**, 4184–4187 (2000).
8. S. Anantha Ramakrishna, "Physics of negative refractive index materials," Rep. Prog. Phys. **68**, 449–521 (2005).
9. J. Valentine, J. Li, T. Zentgraf, G. Bartal, and X. Zhang, "An optical cloak made of dielectrics," Nat. Mater. **8**, 568–571 (2009).
10. J. B. Pendry, D. Schurig, and D. R. Smith, "Controlling electromagnetic fields," Science **312**, 1780–1782 (2006).
11. D. Schurig, J. J. Mock, B. J. Justice, S. A. Cummer, J. B. Pendry, A. F. Starr, and D. R. Smith, "Metamaterial electromagnetic cloak at microwave frequencies," Science **314**, 977–980 (2006).
12. N. Engheta and W. Z. Richard, *Metamaterials: Physics and Engineering Explorations* (Wiley, 2006).
13. S. Zouhdi, S. Ari, and P. V. Alexey, *Metamaterials and Plasmonics: Fundamentals, Modeling, Applications* (Springer-Verlag, 2008).
14. H.-T. Chen, W. J. Padilla, J. M. O. Zide, A. C. Gossard, A. J. Taylor, and R. D. Averitt, "Active terahertz metamaterial devices," Nature **444**, 597–600 (2006).
15. V. G. Veselago, "Formulating Fermat's principle for light travelling in negative refraction material," Phys. Uspekhi **45**, 1097–1099 (2002).
16. I. V. Lindell, S. A. Tretyakov, K. I. Nikoskinen, and S. Ilvonen, "BW-media with negative parameter, capable of supporting backward waves," Microwave Opt. Technol. Lett. **31**, 129–133 (2001).
17. R. W. Ziolkowski and E. Heynman, "Wave propagation in media having negative permeability and permittivity," Phys. Rev. E **64**, 056625 (2001).
18. B. Lahiri, A. Z. Khokhar, R. M. De La Rue, S. G. McMeekin, and N. P. Johnson, "Asymmetric split ring resonators for optical sensing of organic materials," Opt. Express **17**, 1107–1115 (2009).
19. V. A. Fedetov, M. Rose, S. L. Prosvirnin, N. Papasimakis, and N. I. Zheludev, "Sharp trapped-mode resonances in planar metamaterials with a broken structural symmetry," Phys. Rev. Lett. **99**, 147401 (2007).
20. M. S. Rill, C. Plet, M. Thiel, I. Staude, G. V. Freymann, S. Linden, and M. Wegener, "Photonic metamaterials by direct laser writing and silver chemical vapour deposition," Nat. Mater. **7**, 543–546 (2008).
21. K. Kishor and R. K. Sinha, "Design of planar metamaterial optical resonator," in *International Conference on Fiber Optics and Photonics* (Optical Society of America, 2012), paper M3B.5.
22. R. Singh, C. Rockstuhl, C. Menzel, T. P. Meyrath, M. He, H. Giessen, F. Lederer, and W. Zhang, "Spiral-type terahertz antennas and the manifestation of the Mushiake principle," Opt. Express **17**, 9971–9980 (2009).
23. K. Kishor and R. K. Sinha, "Design of planar metamaterial optical antenna," Proc. SPIE **8457**, 84572N (2012).
24. G. Dolling, M. Wegener, C. M. Soukoulis, and S. Linden, "Negative-index metamaterial at 780 nm wavelength," Opt. Lett. **32**, 53–55 (2007).

25. C. Rockstuhl, F. Lederer, C. Etrich, T. Zentgraf, J. Kuhl, and H. Giessen, "On the reinterpretation of resonances in split ring resonators at normal incidence," Opt. Express **14**, 8827–8836 (2006).

26. J. Zhou, T. Koschny, M. Kafesaki, E. N. Economu, J. B. Pendry, and C. M. Soukoulis, "Saturation of the magnetic response of split-ring resonators at optical frequencies," Phys. Rev. Lett. **95**, 23902 (2005).

27. M. W. Klein, C. Enkrich, M. Wegener, C. M. Soukoulis, and S. Linden, "Single-slit split-ring resonators at optical frequencies: limits of size scaling," Opt. Lett. **31**, 1259–1261 (2006).

28. S. Tretyakov, "On geometrical scaling of split ring and double-bar resonators at optical frequencies," Metamaterials **1**, 40–43 (2007).

29. B. Lahiri, S. G. McMeekin, A. Z. Khokhar, R. M. De La Rue, and N. P. Johnson, "Impact of titanium adhesion layers on the response of arrays of metallic split-ring resonators (SRRs)," Opt. Express **18**, 3210–3218 (2010).

30. W. C. Chen, J. J. Mock, D. R. Smith, T. Akalin, and W. J. Padilla, "Controlling gigahertz and terahertz surface electromagnetic waves with metamaterial resonators," Phys. Rev. X **1**, 021016 (2011).

31. B. Lahiri, G. Holland, V. Aksyuk, and A. Centrone, "Nanoscale imaging of plasmonic hot spots and dark modes with the photothermal-induced resonance technique," Nanoletters **13**, 3218–3224 (2013).

32. S. Linden, C. Enkrich, M. Wegener, J. Zhou, T. Koschny, and C. M. Soukoulis, "Magnetic response of metamaterials at 100 terahertz," Science **306**, 1351–1353 (2004).

33. A. M. Nicolson and G. F. Ross, "Measurement of the intrinsic properties of material by time-domain techniques," IEEE Trans. Instrum. Meas. **19**, 377–382 (1970).

34. D. R. Smith, S. Schultz, P. Markos, and C. M. Soukoulis, "Determination of effective permittivity and permeability of metamaterials from reflection and transmission coefficients," Phys. Rev. B **65**, 195104 (2002).

35. M. Iwanaga, "Effective optical constants in stratified metal-dielectric metamaterial," Opt. Lett. **32**, 1314–1316 (2007).

36. P. Markos and C. M. Soukoulis, "Transmission properties and effective electromagnetic parameters of double negative metamaterials," Opt. Express **11**, 649–661 (2003).

37. E. Saenzz, P. M. T. Ikonen, R. Gonzalo, and S. A. Tretyakov, "On the definition of effective permittivity and permeability for thin composite layers," J. Appl. Phys. **101**, 114910 (2007).

38. T. Koschny, P. Markos, D. R. Smith, and C. M. Soukoulis, "Resonant and antiresonant frequency dependence of the effective parameters of metamaterials," Phys. Rev. E **68**, 065602 (2003).

39. R. A. Depine and A. Lakhtakia, "Comment I on resonant and antiresonant frequency dependence of the effective parameters of metamaterials," Phys. Rev. E **70**, 048601 (2004).

40. A. L. Efros, "Comment II on resonant and antiresonant frequency dependence of the effective parameters of metamaterials," Phys. Rev. E **70**, 048602 (2004).

41. Y. Minowa, T. Fujii, M. Nagai, T. O. K. Sakoda, K. Hirao, and K. Tanaka, "Evaluation of effective electric permittivity and magnetic permeability in metamaterial slabs by terahertz time-domain spectroscopy," Opt. Express **16**, 4785–4796 (2008).

List of Publications

Research Publications in refereed international journals:

1. Kamal Kishor, R.K.Sinha, A.D.Varshney, Jaspreet Singh, "Characterization of specially designed Polarization Maintaining Photonic Crystal Fiber from far field radiation patterns", Optics Communications (Elsevier, Science Direct) 283, 5007-5011 (2010).   Cited by - 5

2. Kamal Kishor, R.K.Sinha, A.D.Varshney, "Experimental Verification of Improved Effective Index Method for Endlessly Single Mode Photonic Crystal Fiber", Optics and Laser in Engineering (Elsevier, Science Direct) 50, 182-186 (2012)   Cited by - 7

3. Kamal Kishor, Monu Nath Baitha, R.K.Sinha, Basudev Lahiri, "Tunable negative refractive index metamaterial from "V" shaped SRR structure: Fabrication and Characterization", Journal of the Optical Society of America B (OSA) Vol. 31 No. 7, 1410-1414 (2014).

4. Kamal Kishor, Monu Nath Baitha, R.K.Sinha, "Design and Simulation of "I" shaped Split Ring Resonator metamaterial at optical communication window around 1.55 μm", Optik (Elsevier, Science Direct), IJLEO-D-14-01345 (Accepted) (2015).

Research Publications in refereed conference proceedings:

5. Kamal Kishor, R.K.Sinha, A.D.Varshney, Jaspreet Singh, "Characterization of Polarization Maintaining Photonic Crystal Fiber from Far Field Measurements" International Conference Optics + Photonics 2009, San Diego, CA, USA, Proc. SPIE 7420, Photonic Fiber and Crystal Devices: Advances in Materials and Innovations in Device Applications III, 742015 (2009); doi:10.1117/12.826167
         Cited by – 11

6. Kamal Kishor, R.K.Sinha, "Design of Planar Metamaterial Optical Antenna" International Conference Optics + Photonics 2012, San Diego, CA, USA, (12-16th August 2012), Proc. SPIE 8457, Plasmonics: Metallic Nanostructures and Their

Optical Properties X, 84572N (October 9, 2012); doi:10.1117/12.929581.

<div align="right">Cited by – 1</div>

7. Kamal Kishor and R. K. Sinha, "Design of Planar Metamaterial Optical Resonator," International Conference on Fibre Optics and Photonics, OSA Technical Digest (online) (Optical Society of America, 2012), paper M3B.5.

<div align="right">Cited by – 1</div>

8. Kamal Kishor, R.K.Sinha, A.D.Varshney, Vinit Kumar , "Optical Sensor for the determination of adulteration in petrol: design and development" International Conference Optics + Photonics 2011, San Diego, CA, USA, 21-25th August 2011, Proc. SPIE 8129, Novel Optical Systems Design and Optimization XIV, 81290N (September 21, 2011); doi:10.1117/12.893504.

9. Kamal Kishor, R.K.Sinha, A.D.Varshney, Jaspreet Singh, "Determination of waveguiding and geometrical parameters of Endlessly Single Mode Photonic Crystal Fiber: Theory and Experiment" International Conference Optics + Photonics 2010, San Diego, CA, USA, Proc. SPIE, Vol. 7781, 778103 (2010); doi:10.1117/12.860535.

10. Kamal Kishor, R.K.Sinha, "Geometrical & Wave guiding Parameters of Polarization Maintaining Photonic Crystal Fiber from Far-Field Measurements" International Conference Lasers and Their Applications, Changchun, CIOMP-OSA, China (2011) OSA Technical Digest (online) (Optical Society of America, 2011), paper Tu30.

11. Kamal Kishor, R.K.Sinha, A.D.Varshney, Vinit Kumar "Determination of adulteration in Petrol with Optical Fiber" International Conference IONS-11-OSA(Optical Society of America), Univ. of Southampton, United Kingdom (2011).

12. Kamal Kishor, R.K.Sinha, A.D.Varshney, Jaspreet Singh, "Theory and Experiment on Characterization of Polarization Maintaining Photonic Crystal Fiber from Far-Field Measurements" International Conference ICOP-2009, Chandigarh, India.

Characterization of Photonic Crystal Fibers and Metamaterials: Theory and Experiments

A thesis submitted to the
Faculty of Technology, University of Delhi
for the award of the degree of

DOCTOR OF PHILOSOPHY

IN

APPLIED PHYSICS

By

Kamal Kishor

Under the Supervision of :

PROF. R. K. SINHA

Department of Applied Physics,
Delhi College of Engineering,
(Now, Delhi Technological University)
Faculty of Technology
University of Delhi
Delhi-110 042, India

Chapter 8

CHAPTER 6

Summary and future scope

This chapter includes a brief summary of the main results obtained in previous chapters and the major results of this thesis.

Distinct approaches are studied to develop a deeper understanding of the new photonic waveguides e.g. photonic crystal fiber and metamaterials and the techniques for their characterization, in terms of geometrical and waveguiding parameters.

The work in this dissertation has dealt with the theory and experiments for the characterization of newly designed photonic crystal fiber and metamaterials.

➢ The characterization technique for different types of Endlessly Single Mode Photonic Crystal Fibers (ESM PCFs) in terms of all the key parameters i.e. V-Number, effective refractive index of the cladding, radius of the core and numerical aperture using experimentally measured far-field intensity pattern is developed. It is observed that the transmission characteristics i.e. core diameter, *V*-parameter, Effective refractive index of cladding and numerical aperture obtained from far field measurement match with the SEM data and simulation results using IEIM within the experimental limits. Thus, characterization of ESM-PCFs from its far field radiation pattern measurement provides a useful tool for online characterization of ESM PCFs. It is expected that this method will serve as standard technique to characterize ESM PCFs and will also be useful to design and develop application specific ESM PCFs in optical communication systems.

➢ The characterization technique for specially designed polarization maintaining photonic crystal fiber (PM PCF) in terms of all the key parameters i.e. mode field diameters (MFD), V-values along major and minor axes, mode field area, birefringence, core radius, effective refractive index of cladding and numerical apertures along major and minor axes of PM PCFs using experimentally measured far-field intensity pattern is developed. It is shown that the

experimentally obtained geometrical and wave guiding parameters of the PM PCF match with the manufacturer/simulation/scanning electron microscope (SEM) data within the experimental limits. This new technique of characterization will serve as standard technique to characterize PM PCF and will also be useful to design and develop application specific PM PCF both in optical communication and in sensor systems.

➢ A new design of a V-shaped split ring resonator (SRR) metamaterial is fabricated and characterized and also it has been shown that it is possible to tune a negative refractive index by changing the angular gap of V-shaped SRR. The unique property of this new structure is that by varying the angular gap between its arms, one can change the capacitance (C) for the structure, and hence can tune and control the Negative Refractive Index (NRI). The experimental and computational investigation of the interdependence of the capacitance (C) and inductance (L) of the structure has been done, and it is observed that by changing the angular gap of V-shaped SRRs, it is possible to control/tune their NRI at the corresponding resonance wavelength. Exploiting this important result for the extraordinary electromagnetic properties of the reported structure, the reported structure will put a significant mark in the design and development of Metamaterials based optical switch, tuneable devices, and sensors etc.

➢ A new design of a split ring resonance (SRR) based planar metamaterial is proposed to achieve the negative refraction in optical communication window. All the key electromagnetic parameters i.e. such as permittivity (ε), permeability (μ), refractive index (n) etc have been obtained from the simulation using propagation characteristics for the reported structure. It is observed and reported that the electromagnetic parameters (such as permittivity (ε) and permeability (μ)) as well as the refractive index for the reported structure is negative in broad optical communication windows of 1.4μm to 1.6μm. The reported structure provides a way to build the device such as sensors, cloaking device etc. in the range of optical frequency using the property of negative refraction within very small characteristic size. This achievement opens the way to advance metamaterial technology in optical frequency range for the design of nano-scale optical devices.

There are numerous possibilities to extend the work using the technique developed and also by using the results discussed in this thesis. Some of them are briefly outlined below;

New designs of PCFs are being reported due to inherit advantages of this characterization of fiber. Technique used for characterization of PCFs in this thesis has a distinct possibility to design and develop online characterization technique for futuristic photonic crystal and other micro-structured fiber.

Further, a knowledge of geometrical and waveguiding parameters are enhanced to design fiber optic based devices, therefore the research work carried out in this thesis will be helpful for design and development of emerging devices based on photonic crystal in general and on photonic crystal fiber in particular.

The method will also be useful to design and develop application specific PM PCF for both optical communication and in sensor systems.

Next, Characterization technique for different new PCFs e.g. hollow PCFs, double clad PCFs can be developed using far-field radiation pattern.

This metamaterial structures and characterization techniques reported in this thesis will provides a way to build the device such as sensors, cloaking device etc in the range of optical frequency using the property of negative refraction within very small characteristics size. Exploiting the important result reported in the thesis for the extraordinary electromagnetic properties of the structure, the devices based on tunable metamaterial will be designed and developed e.g. the design of receiver and transmitter antenna for the desired frequency/application range. This achievement opens the way to advance metamaterial technology in optical frequency range for the design of nano-scale optical devices. New design of tunable metamaterial can be designed for the visible frequency spectrum. This leads to a new revolution to the photonic device world.